DOCTORAL THESIS

Higher-Order Shear Deformation Theory for the Elastic Response of Ship Structures

Mikk-Markus Imala

Higher-Order Shear Deformation Theory for the Elastic Response of Ship Structures

MIKK-MARKUS IMALA

TAL
TECH
PRESS

TALLINN UNIVERSITY OF TECHNOLOGY
School of Engineering
Department of Civil Engineering and Architecture
This dissertation was accepted for the defence of the degree 16/07/2025

Supervisor: Prof Kristjan Tabri
                         Department of Civil Engineering and Architecture
                         Tallinn University of Technology
                         Tallinn, Estonia

Co-supervisor: Prof Hendrik Naar
                         Department of Civil Engineering and Architecture
                         Tallinn University of Technology
                         Tallinn, Estonia

Opponents: Prof Zhaolong Yu
                         Department of Marine Technology
                         Norwegian University of Science and Technology
                         Trondheim, Norway

                         Prof Jerolim Andric
                         Department of Naval Architecture and Offshore Engineering
                         Faculty of Mechanical Engineering and Naval Architecture
                         UNIVERSITY OF ZAGREB
                         Zagreb, Croatia

Defence of the thesis: 25/08/2025, Tallinn

Declaration:
Hereby I declare that this doctoral thesis, my original investigation and achievement, submitted for the doctoral degree at Tallinn University of Technology has not been submitted for doctoral or equivalent academic degree.

Mikk-Markus Imala

_____
                                              signature

Kõrgemat järku nihkedeformatsiooni teooria laeva struktuuride elastse vaste analüüsiks

MIKK-MARKUS IMALA

Contents

Abstract

Higher-Order Shear Deformation Theory for the Elastic Response of Ship Structures

The concept design phase of ships has a critical role in establishing foundational design decisions and far-reaching structural consequences. During this stage, the general arrangement of decks is defined, and major structural elements are defined and evaluated with preliminary structural analysis, consequently constraining following developments. As ship design progresses into later design stages and more detailed finite element analysis (FEA) is performed, these early design validations serve as the framework upon which more intricate structural evaluations are built.

During the concept design phase, heavily simplified models are used for structural analyses as detailed scantling design is not yet developed. Elements with large dimensions and adjusted material properties are employed to maintain low computational costs. As the marine industry mainly relies on elements with linear displacement field, stress behaviour within elements and on element boundaries is not accurately predicted leading to significant misrepresentation of maximal stresses and overall stress distribution.

This thesis aims to create a finite element formulation, that can be implemented to increase the FEA accuracy of the static response of a multideck ship in the concept design phase. The higher-order shear deformation (HSD) theory utilizes a global 6-degree of freedom (DOF) nodal definition that enables higher-order displacement field definitions to accurately capture stress behaviour within elements. The theory focuses on creating finite element formulations implementing a novel equilibrium shear flow rate DOF that can describe noncontinuous stress between adjacent elements that significantly improves the stress response in ship structure analysis.

Comparative calculations are presented on models varying in the level of detail to provide a comprehensive understanding of the application potential. Additionally, in every comparison, a selection of planes and cross-sections are analysed to verify the applicability of the proposed theory in areas with high variation in stress distribution due to geometric discontinuities or material changes as well as in areas with less variation.

The results across all analysed models showed sufficient accuracy for describing normal and shear stress distributions in critical planes and cross-sections outperforming traditional linear shell elements. The HSD element captured stress behaviour at discontinuities by incorporating elemental parameters when calculating stress values with the coupled DOFs. By doing so, significant stress maximums and inter-elemental stress behaviour are discovered that otherwise can be significantly underestimated. This method can serve as an efficient tool by increasing the accuracy of coarse mesh 3D structural analysis.

Lühikokkuvõte

Kõrgemat järku nihkedeformatsiooni teooria laeva struktuuride elastse vaste analüüsiks

Laevade kontseptuaalse projekteerimise faasil on kriitiline roll aluslike disaini ja konstruktsiooniliste otsuste määramisel. Selles etapis määratletakse üldine tekiplaan ning peamised konstruktsioonielemendid, mida hinnatakse esialgsetes konstruktsiooni analüüsides, piirates seeläbi järgnevaid arendusi. Liikudes laevadisaini hilisematesse etappidesse, eelnevalt tehtud otsused on raamistikuks, et teostada detailsem lõplike elementide analüüs.

Algses projekteerimise faasis kasutatakse tugevusanalüüsideks lihtsustatud mudeleid, kuna detailne plaanilahendus ei ole veel välja töötatud. Madalate arvutuskulude säilitamiseks kasutatakse suurte mõõtmetega ja kohandatud materjaliomadustega elemente. Meretööstus kasutab peamiselt lineaarset siirdevälja omavaid tasandi elemente, mille puhul puudub täpne ülevaade pinge käitumisest elemendi sees ja servadel tuues kaasa maksimaalsete pingete ja üldise pingejaotuse ulatustliku väära esituse.

Käesoleva töö eesmärk on luua lõplike elementide formuleering, mida saab rakendada mitme-tekilise laeva staatilise reaktsiooni täpsuse suurendamiseks kontseptuaalse projekteerimise faasis. Kõrgemat järku nihkedeformatsiooni teooria kasutab 6-vabadusastmega sõlmede definitsiooni, mis võimaldab kõrgemat järku siirdevälja definitsioone, et hinnata pinge käitumist elementide sees. Teooria keskendub lõplike elementide formuleeringute loomisele, rakendades uudset nihkevoo tasakaalu vabadusastet.

Rakenduspotentsiaali mõistmiseks esitatakse võrdlevad arvutused erineva detailsusastmega mudelite kohta. Lisaks analüüsitakse igas võrdluses erinevaid tasandeid ja ristlõikeid, et kontrollida pakutud teooria rakendatavust nii piirkondades, kus pingejaotuses on suur varieeruvus tingitud geomeetrilistest katkestustest või materjali muutustest, kui ka piirkondades, kus varieeruvus on väiksem.

Kõigi analüüsitud mudelite tulemused näitasid piisavat täpsust normaal- ja nihkepinge jaotuse kirjeldamisel kriitilistes tasandites ja ristlõigetes, parandades tulemusi võrreldes traditsiooniliste lineaarsete tasandelementidega. Kõrgemat järku nihkedeformatsiooni element kirjeldas pinge käitumist katkestuspiirkondades, kasutades elemendi parameetreid pinge väärtuste arvutamisel. Sel viisil avastati olulisi pinge maksimumkohti ja elementide vahelist pinge käitumist, mis traditsioonilistes arvutustes võivad oluliselt alahinnatud olla. Pakutud meetod võib olla tõhusaks vahendiks, suurendades jämeda võrgu 3D konstruktsioonianalüüsi täpsust.

Acknowledgments

I would like to give thanks to my supervisor Prof. Kristjan Tabri for the continued support and unwavering guidance since my Bachelor's degree, through my studies abroad for my Master's degree, and now throughout my research for this thesis. You have played a pivotal role in my academic journey, and I would not have made it here without you in my corner. Secondly, I want to give my thanks to my advisor PhD Hendrik Naar for the knowledge you have shared with me over the years, which has been pivotal in defining my academic and professional passion. Additionally, I would like to extend my deepest gratitude to Prof. Jani Romanoff, for the support offered in this research. Many thanks to the colleagues at Tallinn University of Technology for their support.

I want to thank my lifelong friends and teacher role models who played a big role in shaping me while attending Tallinn Secondary School of Science and who have stood beside me ever since. To my family, my mother Margit and father Meelis, and all my siblings, thank you for believing in me and keeping my morale high. To my late grandmother Leen, I wish I could share this accomplishment with you as you were my biggest supporter in pursuing my dreams. You were, and will always be a source of true inspiration, I miss you.

Lastly and most importantly, my sincerest thanks go to my wife Kaila. Without your support, this journey would have been immensely harder. Thank you for believing in me even at times my motivation was faltering. Your love and words of encouragement have taken me this far and keep pushing me towards my dreams.

Tallinn, 2025
Mikk-Markus Imala

List of publications

The list of author's publications, based on which the thesis has been prepared:

[P1]   Imala, M. M., Naar, H., Tabri, K., & Romanoff, J. 2022. Toward the application of the layer-wise displacement theory in passenger ships—a quasi-static response. Mechanics of Advanced Materials and Structures, 30(22), 4698–4710. DOI: 10.1080/15376494.2022.2103859

[P2]   Imala, M. M., Naar, H., & Tabri, K. 2025. Higher-order shear deformation formulation for the structural response of a multideck ship. Ships and Offshore Structures, 1–26. DOI: 10.1080/17445302.2025.2507714

[P3]   Imala, M.M.; Naar, H.; Tabri, K. 2025. Passenger ship global static response analysis implementing a modified higher-order shear element description. Innovations in the Analysis and Design of Marine Structures. (49–57). CRC Press. DOI: 10.1201/9781003642411-6.

Author's contribution to the publications

Contributions to the papers in this thesis are:

In [P1], the author created the theoretical formulation and compiled the finite element formulation with three calculation scripts: element and node script, stiffness script, and post-processing script. The first compiled a node and element cloud file, the second script was used to create element stiffness matrices and subsequently, global stiffness matrices by adding stiffness components into correct nodal locations, and the third performed matrix multiplications, filtered the resulting nodal degree of freedom vector and exported necessary data. The author also performed 2D FEM calculations. H. Naar and K. Tabri greatly contributed to defining the theoretical formulation as well as provided valuable feedback comments and improvements together with J. Romanoff for the analysis and the manuscript. J. Romanoff was instrumental in providing guidance in positioning the article to be published in the desired and achieved journal.

In [P2], the author reworked the theoretical formulation to be more transparent and applicable in commercial settings. The author defined the nodal degree of freedom mapping for the theory, defined the novel shear flow rate degree of freedom and worked out the equilibrium conditions that facilitate the coupling of all nodal degrees of freedoms. The author generated a workflow where 3D models where all modelled and meshed as well as calculations were run in commercial software. Models applying the higher-order mesh type presented in the research utilized user input stiffness matrices. H. Naar and K. Tabri contributed to defining the desired direction of the theoretical framework and provided valuable feedback and comments for the manuscript.

In [P3], the author improved on the 3D application of the theoretical framework by extending the equations for equilibrium shear flow rate definition and introduced displacement fields for vertical transversal elements. The author defined a simplified multi-deck cruise ship and ran 3D finite element analysis. H. Naar and K. Tabri provided valuable feedback and comments for the manuscript.

Original features

The author believes that the following features in the thesis are original.

1. A novel higher-order shear flow rate degree of freedom is developed that describes the shear flow equilibrium value in all surrounding elements. This degree of freedom and the additional deformation degrees of freedom are incorporated into the displacement field descriptions for a higher-order stress behavior analysis within elements.
2. The nodal equilibrium shear flow rate is parametrically defined with element thickness and material information, which is used to derive independent deformation for surrounding elements with varying definitions. This enables discontinuous stress evaluation in adjacent elements where ship structures change in topology.
3. The novel degree of freedom vector is developed for integration with commercial software. The theory defines a universal nodal degree of freedom mapping that can be implemented in commercial software through user-defined matrix inputs, thus allowing calculations without modifying core solver algorithms and visualization of global displacements.

Abbreviations

2D	Two dimensional
3D	Three dimensional
CUF	Carrera Unified Formulation
DMIG	Direct Matrix Input G-set
DNV	Det Norske Veritas
DOF	Degree of Freedom
FEA	Finite Element Analysis
FEM	Finite Element Method
GL	Germanischer Lloyd
HSD	Higher-order Shear Deformation
LDT	Layerwise Displacement Theory

Symbols

A_1	First-order polynomial equation linear component multiplier
A_3	Third-order polynomial equation cubic component multiplier
B_1	First-order polynomial equation constant component
B_3	Third-order polynomial equation quadratic component multiplier
B_{tot}	Total breadth of the model
C_3	Third-order polynomial equation linear component multiplier
D_3	Third-order polynomial equation constant component
du_i	Displacement increment in node i
dy	Increment in the y-axis direction
E_i	Orthotropic element Young's modulus
G_0	Reference shear modulus value
G^*	Neighbouring horizontal element shear modulus
G^{**}	Neighbouring vertical transversal element shear modulus
G_{ij}	Element shear modulus
h	Element height
H_{tot}	Total height of the model
l	Element length
L_{tot}	Total length of the model
P_1	First-order polynomial equation
P_3	Third-order polynomial equation
$p(x)$	Equation for sin-wave distributed loading
p_0	Amplitude distributed loading
$q_{i,j}$	Shear flow rate degree of freedom value in element i, node j
$q_{el\,i,j}$	Elemental shear flow rate in element i, node j
s_i	The polarity of an element's first edge
s_i'	The polarity of an element's second edge
t	Element thickness
t^*	Neighbouring horizontal element thickness
t^{**}	Neighbouring vertical transversal element thickness
u_i	Nodal displacement in the global x-axis direction
u^*	Nodal displacement of a neighbouring horizontal element
$u(i,j)$	Displacement field function in the x-axis direction
v_i	Nodal displacement in the global y-axis direction
$v(i,j)$	Displacement field function in the y-axis direction
w_i	Nodal displacement in the global z-axis direction
w^{**}	Nodal displacement of a neighbouring vertical transversal element
$w(i,j)$	Displacement field function in z-axis direction
α	Polynomial equation variable

β	Shape function edge length parameter
$\gamma_{xy,i}$	Nodal shear deformation degree of freedom in node i
ϕ_i	First-order shape function for node i
ψ_i	Third-order shape function for node i

1 Introduction

1.1 Background

In modern passenger ship design, the overall dimensions of vessels and the structural complexity have been gradually increasing as companies strive to provide outstanding onboard experience. Ship owners are incentivized to opt for novel and unique architectural solutions while focusing on lightweight design which ultimately leads to an increased need for accurate structural analysis in the earlier concept and basic design phases.

Cruise ship design is divided into three major stages: concept design phase, basic design phase, and detail design phase. These stages require an exponentially increasing number of labor hours, which generates a process where decisions made in every design iteration need to be rigorously analyzed and validated. The concept design phase establishes the critical foundation by setting dimensional constraints and defining the initial deck arrangement, main structural scantlings, and load-carrying pathways. The progression from broad conceptual decisions to creating precise manufacturing paperwork in the later stages of the ship design represents a cohesive systematic refinement process that brings a cruise ship from initial vision to buildable reality, where setbacks due to insufficient structural analysis trigger significant rework during later design stages.

Backed by international committees and classification societies, present-day structural analysis of multideck passenger ships is done using 3D finite element analysis (FEA) to evaluate the structural response (ISSC (1997), DNV-GL (2016)). The level of detail used in the FEA is closely related to the structural design stage as analyses in the concept design phase utilize main structural units and typically only consist of plating structures to evaluate global ship response. Later, when scantling dimensions are defined and outfitting mass can be determined more precisely, the FEA becomes computationally more expensive requiring exponentially more information, modelling and solving time. Early-stage structural analyses are increasingly important when implementing novel design concepts as best-practice-based guidelines do not exist in classification rules and the burden of proof for the reliable execution and implementation is on the ship company.

The research in this thesis is positioned in the conceptual design structural analysis space. An overview of the state of the art is provided for different methods used in early-stage structural analysis of ship design as well as provide insight into the solid mechanics community and how the research on layered composites and thick beams could be implemented in the marine environment.

1.2 State of the art

Historically, the first information about the hull girder response has been gathered using classical beam theories such as the Euler-Bernoulli beam or Timoshenko beam theory (Timoshenko, 1921). Beyond very basic response data, the former neglects shear behaviour altogether or oversimplifies it in the latter, when applied to a multi-deck passenger ship. The first introductions to specialized beam theory applications built on classical beam theories in the marine industry were done by Crawford et al. (1950) and Bleich et al. (1953) describing the hull and superstructure interaction in two-beam systems introducing vertical and shear coupling between the beams.

A review paper presented by Romanoff et al. (2020) challenges traditional approaches in marine engineering by demonstrating that shear-weak superstructures exhibit internal behaviour that deviates from the typical shear force distribution experienced by the hull-girder. The research identifies two potential pathways for addressing the complicated stress behaviour of multideck ships that vary in their perspective. The first of such approaches would be to exploit classical continuum mechanics by building on the multi-beam approaches by Crawford et al. (1950) and Bleich et al. (1953). The research specifically points out the Coupled Beam theory presented by Naar et al. (2004) which divides a ship's cross-section into layered Timoshenko beams and places vertical and shear springs between the layers to model the asymmetric shear behaviour. The theory is further developed to include non-linear material descriptions for the ultimate strength assessment of passenger ships by Naar (2006). Coupled beams were also used by Romanoff et al. (2013) and Toming et al. (2016) to evaluate superstructure and hull interaction. Morshensholuk (2016) applied coupled beams to assess hull girder limit states while also emphasizing local buckling and yielding.

The second pathway described by Romanoff et al. (2020) is to leverage non-classical continuum mechanics by incorporating a micropolar correctional factor into Timoshenko beam theory, thus capturing variation of shear stress along the hull girder's height and length. Research supporting this formulation is mainly found in the solid mechanics community, where higher-order formulations are presented for thick beams, and assumptions to layer-wise coupled finite elements can be drawn upon. Higher-order beam theories utilizing parabolic functions in shear deformation definitions are presented by Levinson (1981), Bickford (1982), Rehfield (1982) and Krishna Murty (1984) to describe higher-order variation in axial displacements in the beam height direction. Ghugal (2009, 2011) describes flexure in thick beams with variationally consistent hyperbolic shear deformation. In-plane displacements are described using third-order polynomials in a higher-order shear deformation theory by Reddy (1984). Higher-order shear deformation theories are often extended into layerwise theories by defining coupling assumptions for displacement DOFs and are applied to composite laminate or layered beam analyses as done by Toledano (1987), Reddy (1987), and Robbins (1991). Carrera (1995) proposed a self-named Carrera Unified Formulation (CUF) where generalized polynomial expansion methods are defined for beams, plates, and shells that were analysed in the marine industry application by Rehan (2017). The research showed a simple hull girder response using 1D beam elements to model coupling between cross-sections made up of L9 CUF elements.

In addition to using multi-beam approaches for early-stage structural response analyses, current best practices are to perform 3D finite element method (FEM) calculations. Typically, passenger ship models utilize convenient yet optimized mesh dimensions that follow deck spacing vertically, main frame spacing longitudinally, and bulkhead or pillar spacing transversally. This approach is implemented to reduce computational cost without underrepresenting major structural units. Optimization methods to model passenger ships in the conceptual design phase were presented by Ringsberg et al. (2012) and Raikunen et al. (2019). In addition to optimizing mesh sizing, orthogonal approaches to defining element stiffness properties are applied to take into consideration the asymmetry of the stiffening structures of the structural unit cell represented with a singular finite element. A two-layer element approach is presented by Hughes (1988) where the first layer defines the plating stiffness, while the second layer takes into consideration the orthogonal stiffeners that are summed into a singular

element stiffness matrix. Andric (2010) and Zanic et al. (2013) used equivalent orthotropic quadrilateral 8 elements to model passenger ships. Romanoff (2007) used the equivalent single-layer theory by Reddy (2004) to define an equivalent element to represent a web-core sandwich panel. An equivalent single-layer technique was used by Avi et al. (2015) to implement stiffener and their spacing into an orthogonal material description. Teguh et al. (2021) analysed passenger ship's ultimate strength using an equivalent single-layer approach. Although there are numerous methods to defining equivalent element stiffness properties, linear displacement fields are most used in these applications. In conceptual design phase, where large elements are used, linear approximation between nodal degrees of freedom may result in significant misrepresentation of stresses within element boundaries and at element edges in areas with high influence from structural stress concentrations or changing topology and resulting element stiffness properties.

This thesis aims to present a finite element definition that would be applicable in marine industry applications to supplement already existing best practices. The methodology focuses on introducing a finite element description that can be implemented with commercial software to seamlessly provide accuracy improvements over using meshing with linear displacement fields. Stress response in ship structures is often highly varying and discontinuous. While the high variance is mainly caused by structural stress concentrations, discontinuities occur in areas with varying element plate thickness. Additionally, the cross-section of stiffening structures often varies, making the equivalent orthogonal stiffness between elements inconsistent. In these areas, standard linear meshing falls short due to linear displacement fields resulting in a singular elemental stress value. Higher accuracy is achieved with increased mesh resolution which increases the computational cost in two aspects. First and most notably, this increases the modelling time by introducing additional unique equivalent element descriptions and secondly by increasing the solving time.

This thesis presents a higher-order shear deformation (HSD) theory that defines a consistent nodal mapping with six DOFs per node, matching the nodal structure in commonly used commercial softwares. The theory presents different definitions for elements on all principal planes as the in-plane response involves different set of non-zero DOFs in the full nodal DOF vector. The vertical longitudinal elements utilize the novel shear flow rate DOF that ensures shear flow equilibrium between all adjacent elements on different principal planes and provides a higher-order stress description. The theory is validated on several simplified ship models varying in the level of detail.

1.3 Objectives of the thesis

The main objective of the thesis is to present a finite element formulation, that could be implemented in the concept design phase and improve the accuracy of the elastic response results. The formulation is defined to fit the confines of commercial software for improved applicability. To achieve this, the thesis has the following objectives:

1. Develop a finite element definition that uses higher-order approximations to accurately assess stress within element boundaries.
2. Provide a methodology to accurately assess stress in structural transition layers, where plating thickness, material grade or scantling geometry changes.
3. Develop the new element formulations in a way that they could be implemented into commercial engineering tools used by maritime industry.

1.4 Scope of work

In multi-deck ship design, 3D finite element analysis is performed to assess the reliability of the ship structures in multiple iterations. An initial assessment is carried out in the concept design phase by following methods to decrease computational cost and modeling time. This typically involves using large element dimensions and linear finite element formulations. To improve the accuracy of the finite element method, we propose the HSD theory that is presented within the span of the three publications summarized in Figure 1.

In [P1], the initial finite element formulation is presented for a 6-node shell element, where nodal displacements are described in corner nodes and shear deformation DOF are described in mid-side nodes. The research presents definitions for the elemental stiffness matrix and external force vector calculated. The comparative analysis is performed on two planar models with distinct geometric characteristics to visualize the accuracy of the proposed layerwise displacement formulation compared to linear mesh types in a variety of planes and cross-sections. The linear mesh models are created and evaluated in FEMAP software.

In [P2], a reworked higher-order shear deformation formulation is presented. The previously used midside nodes have been omitted for improved applicability and a consistent six DOF nodal mapping has been created. A novel shear flow rate DOF is introduced that implements elemental thickness and material properties to independently describe stress in the transition layer between adjacent elements. Unique element definitions for horizontal and vertical elements are provided, as the consistent nodal DOF vector does not allow elements to simply be rotated, and their stiffness matrices be transformed. The analysis shows a simple hollow beam model to initially provide validation on a simpler model and further provide insight into the performance of the HSD formulation over traditional linear mesh usage on a stepped box model.

In [P3], a further improvement to the HSD formulation is added by adding the definition to vertical transversal elements and supplementing the definition of the shear flow rate DOF. A grouping scheme for elements that share a node is presented with considerations to elements on all three principal planes. The comparison analysis defines a simplified cruise ship model and compares the accuracy of the improved HSD formulation to linear mesh results concluding in a clear increase in accuracy of the elastic response when using the HSD theory over conventional linear elements.
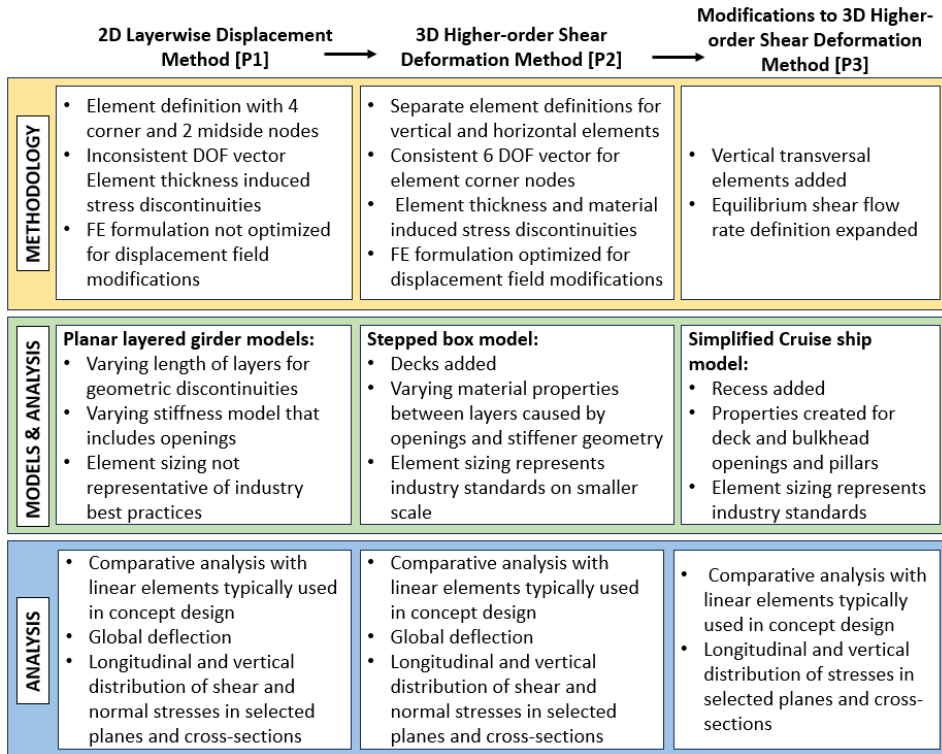
Figure 1. Publication overview for the thesis.

1.5 Limitations

The research in this thesis is limited to the following modeling aspects:

1. Elements are only positioned on the principal planes as shape functions are described in global coordinates and not in an isoparametric formulation.
2. Only in-plane response is considered to minimize computational time. Torsion and bending response are not included at this stage of the research.
3. Commercial software has been used for numerical calculations. Therefore, the proposed formulation is limited to the number of nodal degrees of freedom that are available for the plate elements available in that software.
4. Calculation of equivalent element stiffness properties is not covered as the presented formulation can be used alongside methods to calculate orthotropic properties.
5. Shear stress in an element is identical on all edges; planar stress orthogonality is not considered.
6. Elements in 3D applications need individual descriptions depending on the orientation due to the restricted number of nodal degrees of freedom.

2 Higher-order layerwise displacement formulation

2.1 Definition of variables

The higher-order layerwise displacement (HLD) theory presents a 6-node element positioned in the Cartesian coordinate system, where the in-plane x-axis refers to the ship's longitudinal direction and denotes edge length as length l and in-plane y-axis refers to the ship's vertical direction and denotes edge length as height h. This formulation places mid-side nodes on vertical edges to describe shear behavior as shown in Figure 2:
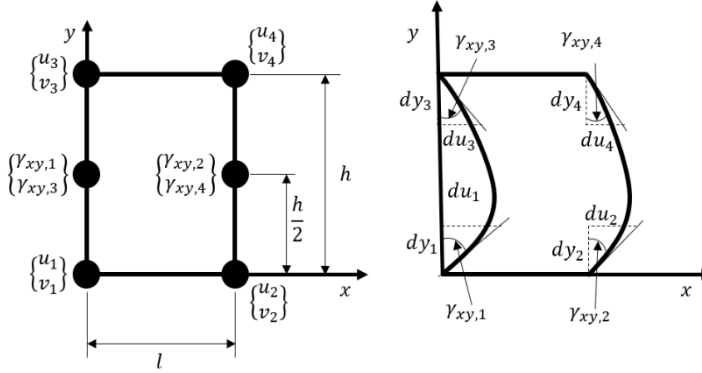

Figure 2. Beam element in the Cartesian coordinate system and explanation of shear strain DOFs. [P1]

where u_i is the longitudinal displacement in node i, v_i is the vertical displacement in node i and $\gamma_{yx,i}$ is the shear strain $\partial u/\partial z$ at the position of node i. Shear strain is described as a DOF of a mid-side node to uncouple the shear strain from nodal displacements in a global finite element formulation thus allowing discontinuous description of shear stress in the vertical direction between adjacent elements.

2.2 Definition of the displacement field

The defined DOFs are applied as polynomial function values to describe displacement fields $u(x,y)$ and $v(x,y)$. The shear deformation variables allow longitudinal displacement in the vertical direction to be described with a third-order polynomial, whereas vertical displacement in both in-plane directions and longitudinal displacement in the longitudinal direction are described with first-order polynomials. Unified representation of polynomial functions used to define element displacement fields:

$$P_3(\alpha) = A_3\alpha^3 + B_3\alpha^2 + C_3\alpha + D_3 , \tag{1}$$

$$P_1(\alpha) = A_1\alpha + B_1 , \tag{2}$$

where indexes 1 and 3 denote the order of the polynomial equation, $A; B; C; D$ are the polynomial constants, α denotes a planar direction and P is the displacement in the planar direction.

Eqs. (1), (2) can be solved for A_3, B_3, C_3, D_3 and A_1, B_1 and regrouped for arbitrary first-order and third-order polynomial variables to represent shape functions in a parametric form as:

$$\begin{cases}\psi_1(\alpha) = (\beta^3 - 3\beta\alpha^2 + 2\alpha^3)/\beta^3 \\ \psi_2(\alpha) = (\beta^2\alpha - 2\beta\alpha^2 + \alpha^3)/\beta^2 \\ \psi_3(\alpha) = (3\beta\alpha^2 - 2\alpha^3)/\beta^3 \\ \psi_4(\alpha) = (\alpha^3 - \beta\alpha^2)/\beta^2,\end{cases} \tag{3}$$

$$\begin{cases}\phi_1(\alpha) = 1 - \alpha/\beta \\ \phi_2(\alpha) = \alpha/\beta\,,\end{cases} \tag{4}$$

where β is the element edge length in α-axis direction. An example of shape function mapping to degrees of freedom is presented in a linear combination for the element description in Figure 2:

$$\begin{aligned}u(x,y) = {}&\psi_1(y)\phi_1(x)u_1 + \psi_1(y)\phi_2(x)u_3 + \psi_2(y)\phi_1(x)\gamma_{xy,1} + \\ &\psi_2(y)\phi_2(x)\gamma_{xy,3} + \psi_3(y)\phi_1(x)u_2 + \psi_3(y)\phi_2(x)u_4 + \psi_4(y)\phi_1(x)\gamma_{xy,2} + \\ &\psi_4(y)\phi_2(x)\gamma_{xy,4}\end{aligned} \tag{5}$$

$$\begin{aligned}v(x,y) = {}&\phi_1(y)\phi_1(x)v_1 + \phi_1(y)\phi_2(x)v_3 + \phi_2(y)\phi_1(x)v_2 + \\ &\phi_2(y)\phi_2(x)v_4,\end{aligned} \tag{6}$$

Shape functions in Eqs. (5), (6) obtain geometric values:

$$\begin{cases}\psi_1(y) = (h^3 - 3hy^2 + 2y^3)/h^3 \\ \psi_2(y) = (h^2y - 2hy^2 + y^3)/h^2 \\ \psi_3(y) = (3hy^2 - 2y^3)/h^3 \\ \psi_4(y) = (y^3 - hy^2)/h^2,\end{cases} \tag{7}$$

$$\begin{cases}\phi_1(y) = 1 - y/h \\ \phi_2(y) = y/h\,,\end{cases} \tag{8}$$

$$\begin{cases}\phi_1(x) = 1 - x/l \\ \phi_2(x) = x/l\,.\end{cases} \tag{9}$$

Detailed description of the finite element equations is presented in [P1] defined using the first variation of potential energy equation.

3   Higher-order shear deformation formulation

Although the layer-wise displacement theory presented in [P1] describes shear stress discontinuously between vertically adjacent elements, the asymmetric nodal positioning with midside nodes on vertical edges as well as inconsistent nodal DOF mapping complicates the implementation of such element definition. The modified HSD formulation describes a constant nodal mapping methodology with elements populating the xy-, xz-, and yz-planes, where nodes are placed only in element corners with six consistent DOFs per node. The methodology presents a definition for a novel DOF that describes an equivalent shear flow rate. The definition for such DOF presents extensions to integrate any element plane that intersects in a specified node. Individual finite element equations are introduced for elements on different principal planes, as the effect on stress behavior varies with element orientation, therefore optimizing the computational efficiency.

3.1 Definition of element displacement fields

Element displacement field descriptions are dependent on the non-zero DOFs that act in-plane to the orientation of that element type. A simplified ship model is modeled with three distinct element types: horizontal elements present in the global x-axis and y-axis direction, vertical longitudinal elements present in the global x-axis and z-axis direction, and vertical transversal elements acting in the global y-axis and z-axis direction. The highest polynomial order that can be expressed with the DOFs in these respective directions is used to define element in-plane displacement fields. Polynomial equations for elements in Figure 3 a), b) are presented in [P2], and for the element in Figure 3 c) in [P3].
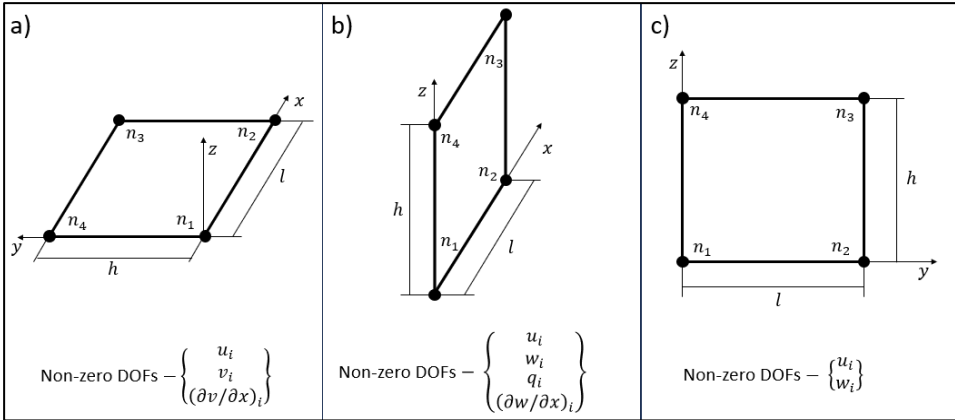

Figure 3. Element coordinate system and non-zero nodal DOF vectors for a) horizontal elements, b) vertical longitudinal elements, and c) vertical transversal elements.

In-plane displacement fields for horizontal elements can be presented in vector form or expanded to show the full linear combination:

$$u(x,y) = \phi_1(y)\phi_1(x)u_1 + \phi_1(y)\phi_2(x)u_2 + \phi_2(y)\phi_1(x)u_4 + \phi_2(y)\phi_2(x)u_3 ,$$

(10)

$$v(x,y) = \phi_1(y)\psi_1(x)v_1 + \phi_2(y)\psi_1(x)v_4 + \phi_1(y)\psi_2(x)\left(\frac{\partial v}{\partial x}\right)_1 +$$
$$\phi_2(y)\psi_2(x)\left(\frac{\partial v}{\partial x}\right)_4 + \phi_1(y)\psi_3(x)v_2 + \phi_2(y)\psi_3(x)v_3 + \tag{11}$$
$$\phi_1(y)\psi_4(x)\left(\frac{\partial v}{\partial x}\right)_2 + \phi_2(y)\psi_4(x)\left(\frac{\partial v}{\partial x}\right)_3 .$$

In-plane displacement fields for vertical longitudinal elements can be presented in vector form or expanded to show the full linear combination:

$$u(x,z) = \psi_1(z)\phi_1(x)u_1 + \psi_2(z)\phi_1(x)\left(\frac{\partial u}{\partial z}\right)_1 + \psi_1(z)\phi_2(x)u_2 +$$
$$\psi_2(z)\phi_2(x)\left(\frac{\partial u}{\partial z}\right)_2 + \psi_3(z)\phi_2(x)u_3 + \psi_4(z)\phi_2(x)\left(\frac{\partial u}{\partial z}\right)_3 + \tag{12}$$
$$\psi_3(z)\phi_1(x)u_4 + \psi_4(z)\phi_1(x)\left(\frac{\partial u}{\partial z}\right)_4 ,$$

$$w(x,z) = \phi_1(z)\psi_1(x)w_1 + \phi_2(z)\psi_1(x)w_4 + \phi_1(z)\psi_2(x)\left(\frac{\partial w}{\partial x}\right)_1 +$$
$$\phi_2(z)\psi_2(x)\left(\frac{\partial w}{\partial x}\right)_4 + \phi_1(z)\psi_3(x)w_2 + \phi_2(z)\psi_3(x)w_3 + \tag{13}$$
$$\phi_1(z)\psi_4(x)\left(\frac{\partial w}{\partial x}\right)_2 + \phi_2(z)\psi_4(x)\left(\frac{\partial w}{\partial x}\right)_3 ,$$

where definitions for $(\partial u/\partial z)_i$ variables are derived from Eq. (16) and presented in more detail in [P3].

In-plane displacement fields for vertical transversal elements can be presented in vector form or expanded to show the full linear combination:

$$v(y,z) = \phi_1(z)\phi_1(y)v_1 + \phi_1(z)\phi_2(y)v_2 + \phi_2(z)\phi_1(y)v_4 + \phi_2(z)\phi_2(y)v_3 , \tag{14}$$

$$w(y,z) = \varepsilon_1(z)\phi_1(y)w_1 + \varepsilon_1(z)\phi_2(y)w_2 + \varepsilon_2(z)\phi_1(y)w_4 + \varepsilon_2(z)\phi_2(y)w_3 . \tag{15}$$

The finite element formulations for each element positioning type are presented in [P2] by defining the strong-form differential force equations for a unit shell element. The differential equations are integrated over the volume and manipulated to create vectorized weak-form equations. Definitions for shape function matrices and differential operator matrices are presented to describe generalized finite element equations.

3.2 Definition of equilibrium shear flow variable

Element definitions are described in a typical global coordinate system used in shipbuilding, where the x-axis is aligned with the longitudinal direction, the y-axis is aligned with the transversal direction, and the z-axis is aligned with the vertical direction. The six nodal DOFs present in every node are u, v, w denoting nodal displacements in x-, y-, and z-axis directions respectively, q denoting equilibrium shear flow rate in the node, and deformations $(\partial v/\partial x)$, $(\partial w/\partial x)$ denoting consistent deformation along the x-axis as it is assumed that material performs elastically and cannot separate at element boundaries. The equilibrium shear flow rate q is defined as:

$$q = q_{el,xz} + q_{el,xy} + q_{el,yz} = \left(\frac{\partial u}{\partial z} + \frac{\partial w}{\partial x}\right)t\left(\frac{G}{G_0}\right) + \left(\left(\frac{\partial u}{\partial y}\right)^* + \right.$$
$$\left.\frac{\partial v}{\partial x}\right)t^*\left(\frac{G^*}{G_0}\right) + \left(\frac{\partial v}{\partial z} + \left(\frac{\partial w}{\partial y}\right)^{**}\right)t^{**}\left(\frac{G^{**}}{G_0}\right). \tag{16}$$

DOF value q comprises neighboring element-specific q_{el1}, q_{el2}, and q_{el3} values, where $el1$ is located on the xz-plane, $el2$ is located on the xy-plane, and $el3$ is located on the yz-plane. Additionally, t is the element thickness, $(\partial u / \partial y)^*, t^*, G^*$ are parameters of a neighboring horizontal element on xy-plane, $(\partial w / \partial y)^{**}, t^{**}, G^{**}$ are parameters of a neighboring transversal vertical element on the yz-plane. G_0 is a reference shear modulus value to account for the change in material properties in adjacent elements:

$$G_0 = \sum_{i=1}^n G_i / n, \tag{17}$$

where G_i denote the shear moduli used in the analysis and n shows the total number of shear moduli considered. The formulation can be adjusted to elements, where in-plane shear moduli vary, depending on the direction. In these applications, G_i is the relevant shear modulus along the edge where shear flow equilibrium is defined. Deformation parameters $(\partial u / \partial y)^*$ and $(\partial w / \partial y)^{**}$, are always considered in the direction of the positive axis.

Eq. (16) is explained in a small element system presented in Figure 4 a), where the maximum amount of elements surrounds the central node under consideration.
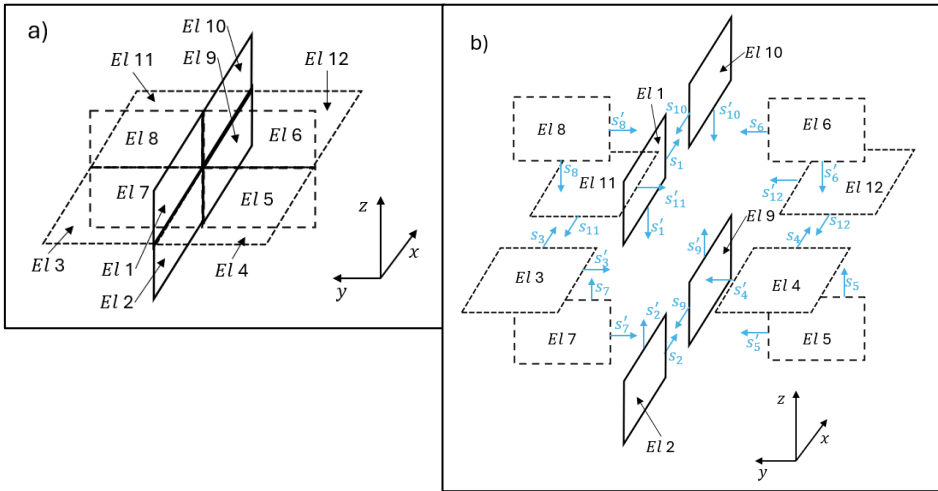

Figure 4. Example element intersection for a) non-exploded view b) for exploded view with edge normal directions. [P3]

In general form, the equilibrium between individual shear flow rates $q_{el,i}$ can be described incorporating the in-plane polarity of the element edges as:

$$\sum_{i=1}^n q_{el,i} s_i s_i' = 0, \tag{18}$$

where $q_{el,i}$ are the element-specific shear flow values and multipliers s_i and s_i' obtain polar values 1 or -1 referring to the positive or negative in-plane direction of the edge normal.

After inserting the polarity values, the equilibrium equation for shear flow rates in the central node according to the element system shown in Figure 4 b) becomes:

$$-q_{el1} + q_{el2} - q_{el3} + q_{el4} + q_{el5} - q_{el6} - q_{el7} + q_{el8} - q_{el9} + q_{el10} + q_{el11} - q_{el12} = 0. \tag{19}$$

$$q_{el2} + q_{el4} + q_{el5} + q_{el8} + q_{el10} + q_{el11} = q_{el1} + q_{el3} + q_{el6} + q_{el7} + q_{el9} + q_{el12}. \tag{20}$$

Eq. (20) is further grouped based on direct element edge adjacency that is required for Eq. (16):

$$q_{el2} + q_{el4} + q_{el5} = q_1, \tag{21}$$

$$q_{el8} + q_{el10} + q_{el11} = q_2, \tag{22}$$

$$q_{el1} + q_{el3} + q_{el6} = q_3, \tag{23}$$

$$q_{el7} + q_{el9} + q_{el12} = q_4. \tag{24}$$

In Eqs. (21) to (24) the final summation values represent the constant nodal DOF value:

$$q_1 = q_2 = q_3 = q_4 = q. \tag{25}$$

Therefore, in Eq. (16) the grouped elements share an edge and have matching multiplied polarity of edge normals. An example partial expansion of Eq. (16) involving elements on vertical longitudinal and horizontal planes is presented in [P2] and a full expansion involving all principal plans is presented in [P3].

4 Models used for validation

4.1 Modeling considerations

The models created for the analysis of HLD and HSD formulations use equivalent plate structures, where different configurations of stiffened panels are represented with equivalent plate elements. The details of calculating equivalent stiffness components are not discussed in this research, however, methods such as the smeared stiffness method or equivalent single-layer method can be applied. The different vertical stiffened panel types such as superstructure outer shell with large openings for modular cabin installation, pillar section with connecting girders, outer shell or bulkhead with small openings, and standard stiffened panel are shown in Figure 5 a). Horizontal equivalent elements substitute horizontal deck stiffened panels or hollowed deck sections, see Figure 5 b). Equivalent elements are defined by transferring orthotropic Young's modulus and Poisson ratio values, and shear modulus values as well as directly using original plating thickness to accurately describe local shear flow at element edges.

$$E_1, E_2, v_1, v_2, G, t$$
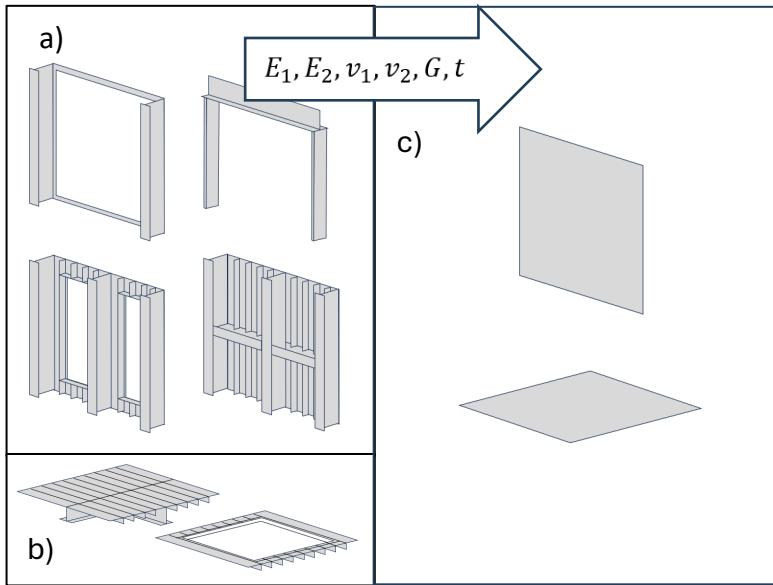
Figure 5. Structural conversion into equivalent plating for a) vertical structures, b) horizontal structures.

Additionally, the modeling in this research uses industry standards for coarse mesh applications as this decreases the time spent on model creation as well as actual solver time, both of which are a factor in the total computational cost. Especially in applications, where equivalent elements have been used to represent the added stiffness from stiffening structures or reduced stiffness from openings, it is important to limit the number of unique element descriptions needed. Figure 6 shows an example of how that number increases between coarse mesh and semi coarse mesh. In addition to increased solver time, and the number of unique orthotropic element definitions, computational cost is further increased with the application of semi-coarse mesh, as element properties cannot be applied to vertical structures simultaneously and need to be circulated between adjacent elements.
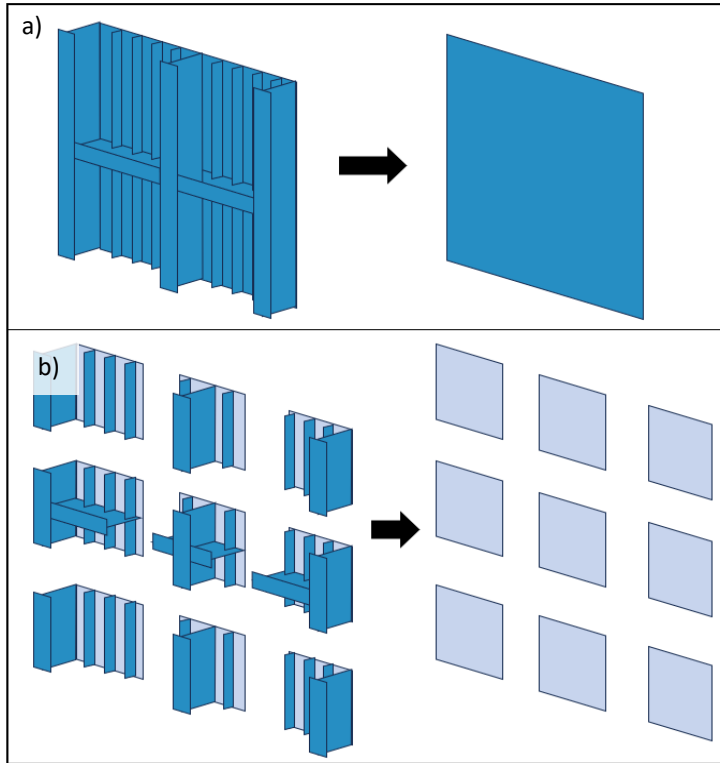
Figure 6. Equivalent plate element creation for a) coarse mesh, b) semi-coarse mesh. [P2]

4.2 Hull girder models

The HLD formulation is applied in [P1] to the case studies presented by Toming et al. (2016). The article defined two simple planar models: a stepped beam model with uniform stiffness in Figure 7 a), and a uniform beam model with varying stiffness in layers due to openings in Figure 7 b). Both models consist of three major segments between which the plate thickness varies. The varying stiffness model is further divided into three element layers in areas of openings. The analysis for the stepped beam model includes three mesh sizes: Coarse mesh that places a single element with dimensions 1000 x 3000 mm over the height of a layer, semi-coarse mesh that vertically divides layers into three elements with dimensions 1000 x 1000 mm, and fine mesh that further refines the element to dimensions 200 x 200 mm. The varying stiffness model includes two meshing configurations: Coarse mesh that uses maximum element dimensions vertically and consistent 1000 mm dimension in length, and fine mesh with dimensions 150 x 150 mm. The HLD models are meshed to match the coarse and semi-coarse mesh variations to compare performance between similarly sized mesh against the substantially finer mesh configurations. The total number of elements for both models between all meshing variations is in Table 1.

Table 1. Number of elements between meshing variations [P1].

Model	Meshing variation	Total elements
Stepped beam model	Coarse mesh	120
	Semi-coarse mesh	360
	Fine mesh	9300
Varying stiffness model	Coarse mesh	520
	Fine mesh	23000

FE models use an elastic foundation as boundary conditions which is applied by creating a row of elements with significantly reduced stiffness and fixed free nodes, see Figure 7 c).

Identical sinusoidal loading according to Eq. (26) creating a global sagging condition has been applied to the bottom edge nodes in both models.

$$p(x) = p_0 * \cos\left(\frac{2\pi x}{L_{tot}}\right). \tag{26}$$

Here, the load amplitude is $p_0 = 60$ N/mm and the total length of the model is $L_{tot} = 60$ m. Uniform material Young's modulus and Poisson ratio properties are used: $E = 210$ GPa, and $\nu = 0.3$. NX Nastran solver was used in FEMAP2021.2 software to analyze linear element models while Mathcad15 software was used to compile and analyze layerwise displacement theory models.
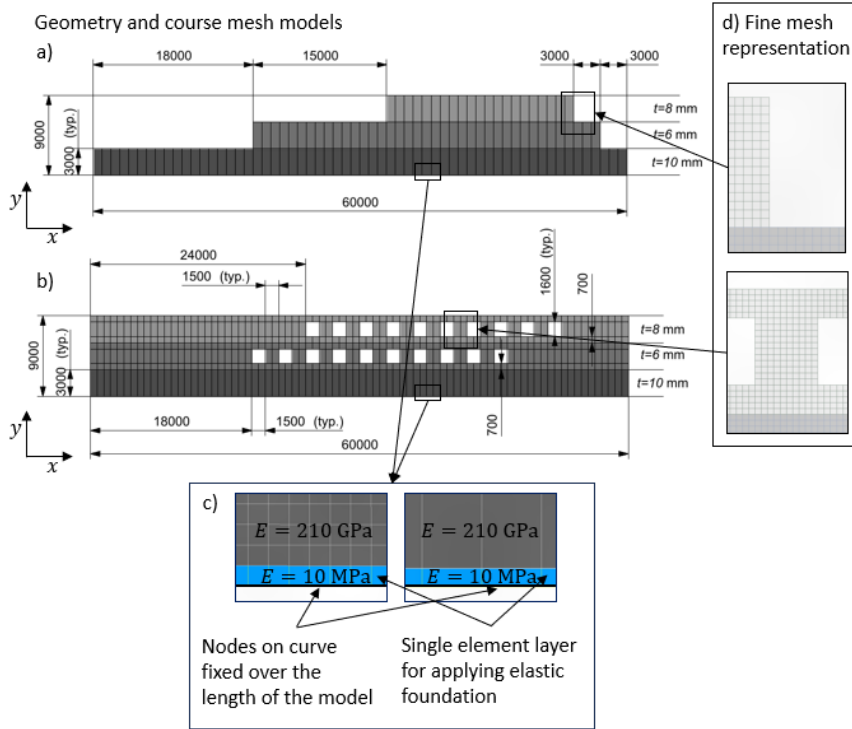
Figure 7. Geometry and FE plate models for a) stepped beam with uniform layer stiffness and b) uniform beam with varying layer stiffness; c) principles of applying elastic foundation, and d) detail views showing the comparative size of the used fine mesh. [P1]

4.3 Stepped box model

The HSD formulation is tested in [P2] on a stepped box model representing a small multideck ship that consists of outer shell sections and two inner bulkhead sections connected to six horizontal plating sections. The resemblance to a real-life stress distribution is achieved by increasing deck thickness in the bottom and top decks and including a weakened outer shell section above the horizontal midplane as windows and other openings lower the shear stress-carrying capabilities in these structures. The addition of deck plating allows for that stress to be carried into the central longitudinal bulkhead. The stepped box model has dimensions of length $L_{tot} = 60$ m, breadth $B_{tot} = 9$ m, and height $H_{tot} = 12.4$ m. Geometry models with material designations and properties as well as cross-sectional information with deck numeration are presented in Figure 8.
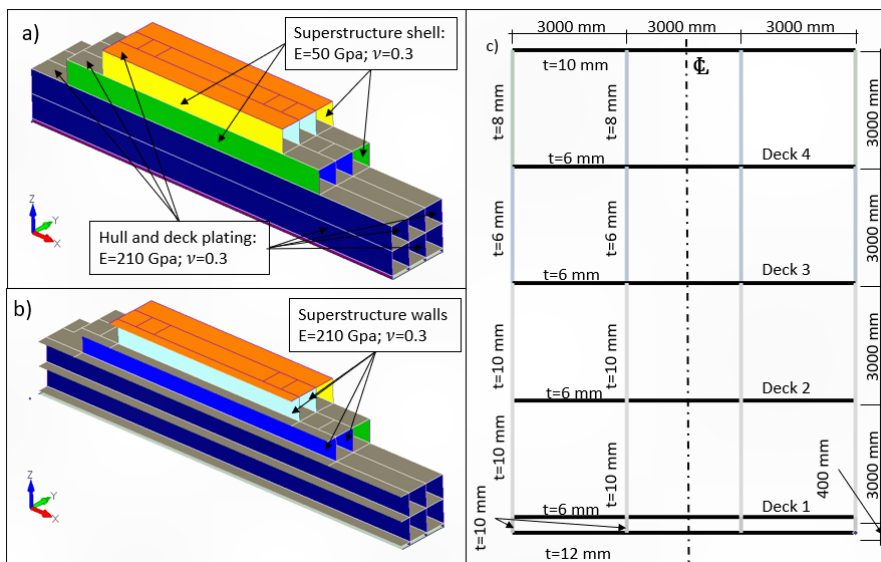
Figure 8. 3D model geometric and material parameters a) outer walls, b) superstructure walls, and c) cross-section. [P2]

Like the hull girder models, the stepped box model analysis seeks to compare the proposed HSD formulation against the typical linear mesh used in the concept design phase. Three mesh sizes are considered: course mesh used with HSD and linear element formulation, semi-coarse mesh, and fine mesh that is only used with linear element formulation. The course mesh model in Figure 9 a) consisting of a total of 728 elements, is defined based on common practices to describe every horizontal and vertical section spacing with a single element resulting in 3000 x 3000 mm dimensions in most elements excluding vertical elements between the double bottom and deck1. The semi-coarse mesh model refines the mesh size in vertical structures to 1000 x 1000 mm dimensions providing a good comparison if marginally decreasing element dimensions for linear mesh has similar effects to using higher-order element definitions. The coarse mesh model consists of a total of 3720 elements, see Figure 9 b). The fine mesh model that places 10 elements with dimensions 300 x 300 mm between decks provides results that

are considered as the base of the comparison, although this element sizing is considered unreasonably fine in the concept design phase due to the increased computational cost, see Figure 9 c).
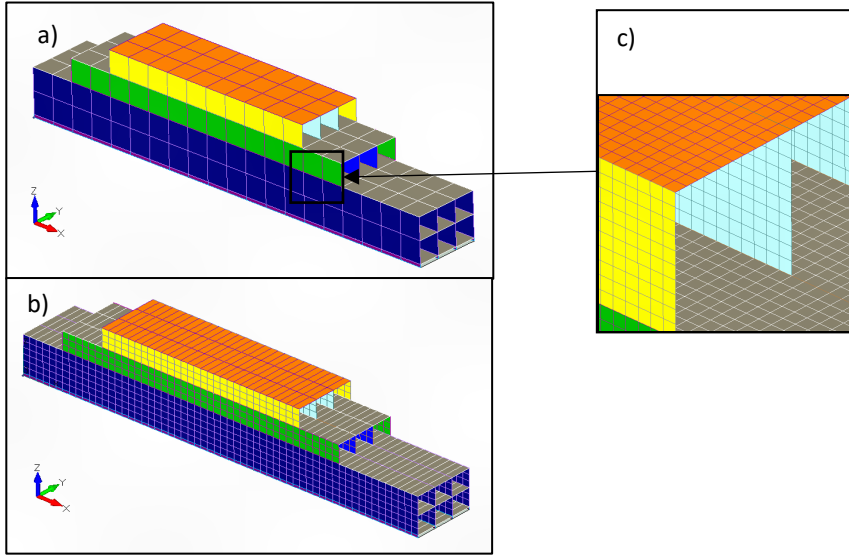

Figure 9. Finite element 3D models of stepped box model: a) coarse mesh model, b) semi-coarse mesh model, and c) fine mesh model. [P2]

Vertical distributed loading defined in Eq. (26) is applied to the bottom edges of all vertical shell sections with amplitude distributed force $p_0 = 200$ N/mm and total length of $L_{tot} = 60$ m.

Orthotropic material properties have been defined as $E_1 = E_2 = 210$ GPa, $v_1 = v_2 = 0,3$ for full-stiffness sections and $E_1 = E_2 = 50$ GPa, $v_1 = v_2 = 0,3$ for weakened sections in the superstructure outer shell. The vertical sections are supported on elastic foundations as boundary conditions.

4.4 Cruise ship model

A cruise ship model with global dimensions $L_{tot} = 300$ m, breadth $B_{tot} = 42$ m, height $H_{tot} = 51$ m has been created in [P3] to further analyze the HSD formulation after further expansion of the shear flow rate definition and the addition of transversal bulkheads. The model consists of 16 decks in total with a uniform vertical spacing of 3.4 m, including thickened layers for the double bottom and cofferdam layers. Longitudinally, the ship has two central bulkheads and three pillar lines. The cross-sectional main dimensions and structures are shown in Figure 10.

Figure 10. Conceptual cruise ship cross-section dimensions. [P3]

Figure 11 shows the side profile of the cruise ship and transversal bulkhead spacing that varies from 40 m in the aft and foreship to 30 m in the two midship watertight sections.

Figure 11. Transversal bulkhead spacing. [P3]

The cruise ship plating structures represent different configurations of stiffened panels such as is seen in Figure 5. Openings in the superstructure outer shell, bulkheads, and decks create the necessity of defining weakened material properties for these areas. In this research, the specific material stiffness values are not of great interest as identical geometric models are compared against each other. General stiffness values have been defined to achieve realistic behavior. Numerical values for different materials are consolidated in Table 2 with applications in cruise ship structures visualized in Figure 12.

Table 2. Material property definitions and applications. [P3]

Name	Young's modulus, $E_1; E_2$ [GPa]	Poisson ratio, v	Application
M1	210	0.3	Hull, bulkheads, decks,
M2	50	0.3	Superstructure shell, pillars, superstructure bulkhead openings
M3	100	0.3	Hull bulkhead openings
M4	10	0.3	Deck openings

Figure 12. The structural breakdown of the cruise ship conceptual model: a) outer shell, b) longitudinal bulkhead, c) pillars, d) deck plating, e) deck openings, f) transversal bulkheads. [P3]

Two mesh sizes have been defined for the cruise ship model: coarse mesh model, and fine mesh model. Mesh dimensions for the coarse mesh model have been derived from the cross-section definition placing the minimal amount of elements between structural elements. Longitudinal vertical elements are dimensioned as 5 x 3.4 m, with the height referring to single deck spacing and the length referring to the main frame spacing. A similar length is used for horizontal elements, however, their transversal dimension is driven by the distance between the bulkhead, pillars, and outer shell. The coarse mesh model comprises 10228 elements in total. The fine mesh model further refines the element sizing to uniform 1 x 1 m elements in vertical transversal and horizontal elements and 1 x 1.13 m in vertical longitudinal elements, placing three elements between two adjacent decks, therefore increasing the number of total elements in the model to 246438. In the concept design phase, this mesh sizing would be unreasonable due to increased computational cost as well as for the total number of equivalent element properties needed to be calculated. Therefore, the fine mesh model is used to compare with the coarse mesh models.

The cruise ship distributed curve loading has been applied on the longitudinal structures at the bottom of the model, see Figure 13 a), calculated according to Eq. (26), with amplitude force $p_0 = 200$ N/mm and total length of $L_{tot} = 300$ m.

The model is placed on an elastic foundation, which is modeled with an extra row of low-stiffness elements under the outer shell and longitudinal bulkhead structures. These elements are fixed at their bottom nodes, thus facilitating global sagging conditions under sinusoidal distributed loading. Element properties for the elastic foundation are $E_{el} = 1$ MPa; $v = 0.3$.
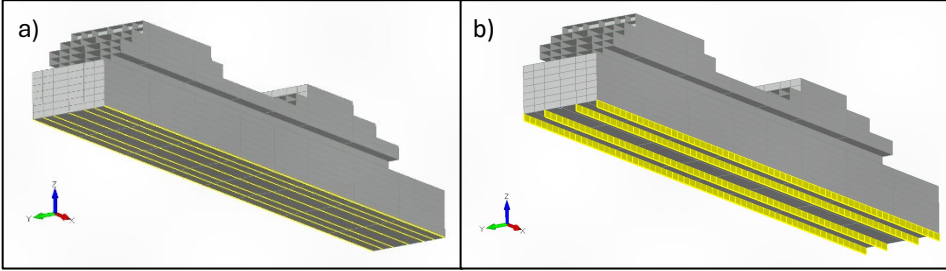
Figure 13. Cruise ship FE model a) load-carrying edges for vertical longitudinal structures, b) elastic foundation elements. [P3]

The HSD formulation is created together with Matlab 2023 and FEMAP 2021.2 software, where the geometric model is created in FEMAP 2021.2. The nodal and element cloud data has been exported into Matlab 2023, where the subroutines to create a global stiffness matrix are described. The global stiffness matrix is subsequently imported into the geometric model in FEMAP 2021.2 using the Direct Matrix Input G-set (DMIG) procedure. NX Nastran solver was used for the calculations after which post-processing was performed partly in both Matlab 2023 and FEMAP 2021.2. Although a multistep process, the desire is to perform computationally costly model and mesh creation, and matrix multiplications in a commercial solver and receive realistically displaced mesh as a result.

5 Results

The comparative analyses in this thesis are structured to give insight into the performance of the formulations developed within the publications. This thesis summarizes equally dimensioned standard linear coarse mesh calculations typically used in the marine industry for conceptual design phase calculations. By comparing linear and higher-order coarse mesh methodologies against fine mesh results that would be available in later design stages, a clear pathway for adapting higher-order formulations in computationally light models is created to bridge the gap between the tradeoff of result accuracy versus model preparation time and computational cost.

The comparisons systematically start from examining global deflection behavior and continue to define critical cross-sections and horizontal planes, where stress distributions experience nonlinearities due to topological or material changes in structures. This approach provides a thorough overview of structural performance across relevant areas effectively demonstrating the applicability of the proposed higher-order formulations over conventional linear approaches while maintaining the desired efficiency during conceptual design phases.

5.1 Hull girder model analyses

Hull girder deflection analyses in Figure 14 show minimal deviation between coarse and fine mesh formulations alluding to the reduced importance of mesh sizing when analyzing global displacements. For the stepped beam model both coarse mesh models resulted in 2–3% underestimated global deflection at the lowest point in a sagging condition. For the unified beam model with varying layer stiffness, the deflection was similarly underestimated by 2–4%.

Cross-sections for stress analysis in stepped beam models were chosen at $x = 19500$ mm, $x = 34500$ mm, and $x = 43500$ mm. Two of these cross-sections are specifically chosen to be near structural discontinuities to better evaluate maximum stress caused by corner effects in the meshing. A third cross-section is chosen to illustrate the stress magnitude difference between more linearly behaving cross-sections and stress-critical cross-sections.
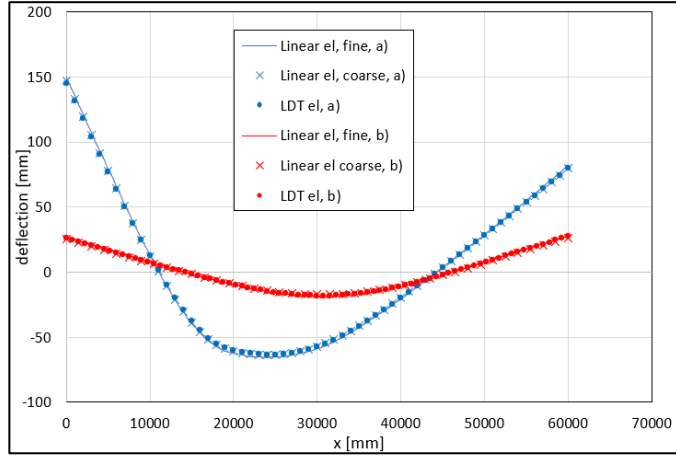
Figure 14. Comparison of deflections: a) stepped beam, b) unified beam with varying layer stiffnesses. [P1]

Normal stress distributions in Figure 15 show notable desired agreement between the LDT coarse mesh and fine linear mesh, whereas the identical mesh sizing for linear mesh shows a clear drop-off in the ability to trace fine mesh results. Most notable discrepancies between the accuracy of LDT and linear coarse mesh happen in the model boundaries. Linear elements use first-order polynomials for approximations which after partial derivation results in constant stress values within elements. Stress values at boundaries can be estimated by averaging elemental stress values into corner nodes, however, this method can significantly misrepresent stress values as evidenced.

This deficiency is further visualized in Figure 15 in shear stress distributions, where higher-order formulations trace fine linear mesh results closely, while coarse linear mesh omits most critical areas in the stress distributions, especially evident in cross-sections a) and b) in areas most prominently affected by the geometric discontinuities.
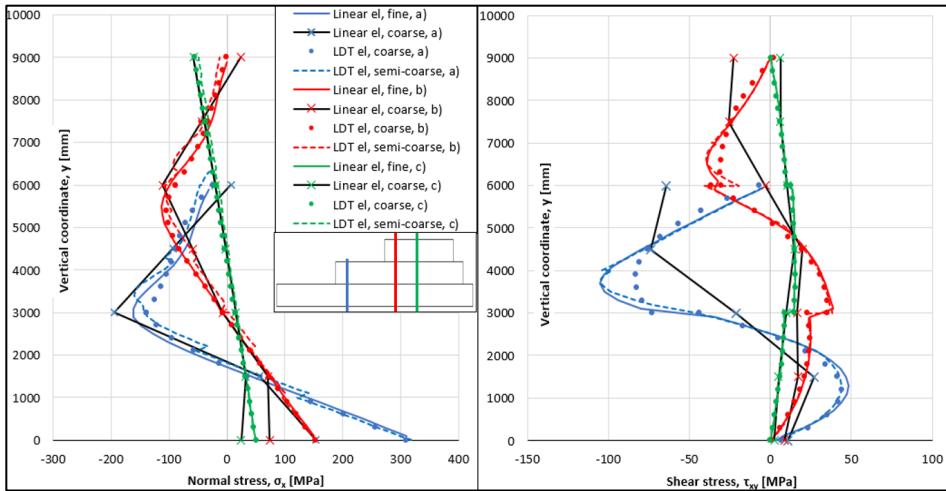
Figure 15. Normal stress, σ_{xx}, and shear stress τ_{xy} in the stepped beam at a) x = 19500 mm, b) x = 34500 mm, c) x = 43500 mm. [P1]

Cross-sections that are analyzed in the unified beam model with varying stiffness similarly present different stress behaviors for the best overall coverage. The first cross-section is defined at $x = 14625$ mm to show results that are not greatly affected by the missing elements within the layers of the model. The second cross-section at $x = 24750$ mm shows discontinuous stress distributions by crossing the openings and the third cross-section at $x = 43875$ mm evaluates the highly varying stress distributions that are influenced by the corner stress concentrations.

In general, it can be said that all mesh types are extremely coincident in cross-section a) due to a less varying stress distribution. Although less important due to the magnitude of the difference in stress values, cross-section b) once again shows how constant elemental stress value cannot be accurately averaged into nodal values in an area where corner effects are present. Cross-section c) shows a very notable and highly accurate tracing between coarse LDT mesh and fine linear mesh, whereas coarse linear mesh underestimates maximum stress values by up to 50% in some areas.
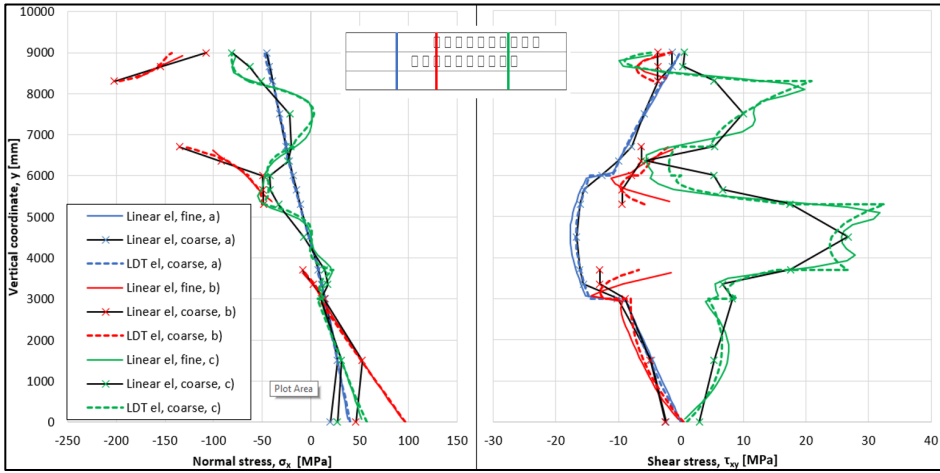
Figure 16. Normal stress, σ_{xx}, and shear stress τ_{xy} in unified beam with varying stiffness at a) x = 14625mm, b) x = 24750mm, c) x = 43875mm. [P1]

5.2 Stepped box model

The stepped box model applies the modified HSD formulation to similarly compare the applicability and the accuracy of higher-order meshing over standard linear meshes. First, the global deflection of the stepped box model is presented in Figure 17. The comparisons show that global deflection is overall highly corresponding with coarse mesh models having slightly underestimated values. In the bottom edge in Figure 17 a), the difference is around 2%, while the difference in the top edge in Figure 17 b) reaches 5% between the coarse mesh models and fine mesh model.
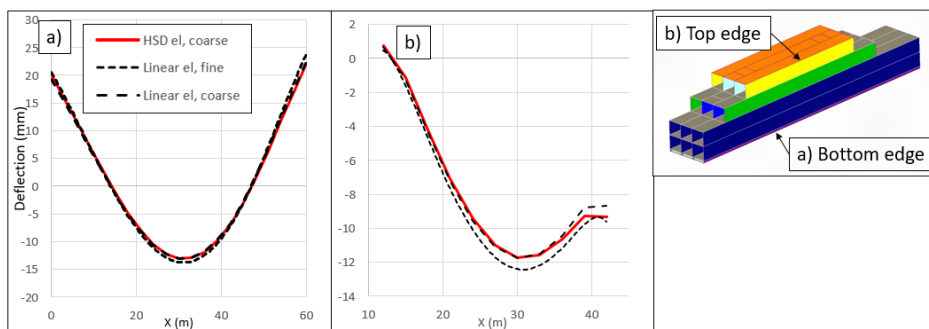
Figure 17. Global deflection comparison in a) bottom edge, b) top edge. [P2]

In addition to cross-section, stepped box model analysis adds a closer look into longitudinal stress distribution at the plane $z = 6.4$ m which is especially of great interest, as in this layer plate element thickness as well as material properties change. The plating thickness typically is lowered due to the lowered normal stress carried by the plating in global bending while the equivalent stiffness properties are lowered in the outer hull structures due to openings in the outer shell above the main deck.

The longitudinal distributions in Figure 18 consider stress values when approaching upwards to the transition layer. This means that in the fine linear mesh model, the stress values of the first element below the transition are considered, while in the coarse linear mesh model, the constant elemental stress values are averaged into nodal positions and the average stress values at the transition layer are used. In the HSD element model, the stress value directly at the layer is considered calculated in the element below the transition layer.

The comparison reveals that the HSD coarse element formulation traces fine linear formulation results to a high degree, with no clear deficiencies. Differences in maximum values can be emphasized, however, this can be attributed directly to mesh sizing effects. Additionally, HSD outperforms coarse and semi-coarse linear mesh in evaluating normal stress in the outer shell in Figure 18 d) and shear stress in the inner bulkhead in Figure 18 a). The HSD element mesh shows excellent correlation, while the coarse and semi-coarse linear mesh, although corresponding with each other, lack accuracy.

A deeper analysis of these graphs is presented in Figure 19 and Figure 20. There, stress results for fine element mesh have been given for the element above and below the transition layer separately. As coarse and semi-coarse mesh stress results can only be described in the existing nodal position, a similar direction-specific approach is not available. For the HSD formulation, the independent stress values are approximated within the relevant element at the element boundary.

Multideck ships typically have weakened outer shell structures above the main hull, as these structures have significant openings for passenger comfort and additionally have lowered thickness. As a result, a significant amount of shear stress, carried in the outer hull structures, is transferred over to the stiffer longitudinal bulkhead visible only in HSD and fine linear mesh models in Figure 19. The opposite effect is seen for normal stress distributions in Figure 20.
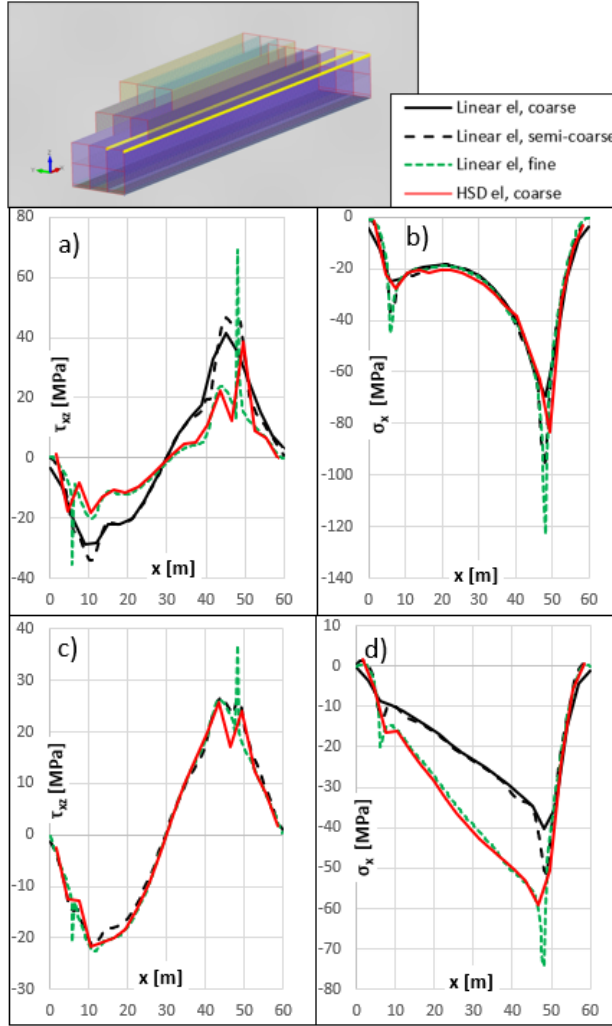
Figure 18. Longitudinal distribution at $z = 6,4$ m for a) inner wall shear stress, b) inner wall normal stress, c) outer wall shear stress, d) outer wall normal stress. [P2]

The necessity of evaluating stress results in transition layers with a direction-specific method can be reasoned when looking at the difference magnitude of secondary maximum stresses compared to the fine linear mesh values shown for shear and normal stress in Figure 19 and Figure 20.

At the aft peak coordinate $x = 11$ m, shear stress for the HSD element formulation differs from the fine element results by 5% and 2% in the upper and lower elements respectively, whereas semi-coarse mesh maximum shear stress values differ by 34% and 70% respectively. The related values for the foreship secondary maximum shear stress at $x = 43,5$ m are 16% and 3% for the HSD formulation and 70% and 47% for the semi-coarse linear element mesh. The respective normal stress difference percentages in the aft in Figure 20 are 15% and 4% for the HSD element formulation and 85% and 47% for the semi-coarse linear mesh. In the foreship secondary peak, the difference is 13% and 4% for the HSD element and 127% and 40% for the semi-coarse linear mesh.
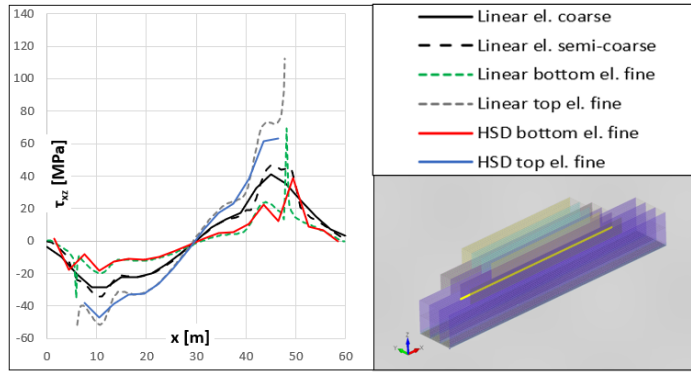
Figure 19. Shear stress longitudinal distribution at $z = 6,4$ m in inner wall. [P2]
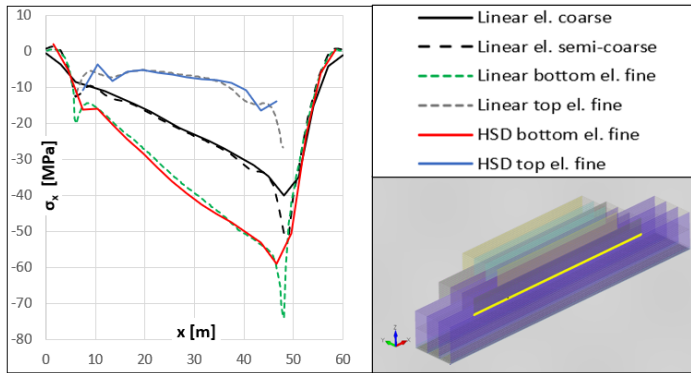
Figure 20. Normal stress longitudinal distribution at $z = 6,4$ m in outer wall. [P2]

The deficiencies of coarse linear meshing and the improved accuracy of the HSD formulation are further strengthened on vertical shear and normal stress distributions in two cross-sections at $x = 22,5$ m, shown in Figure 21 that presents an overview of a more orderly behaving cross-section, while the cross-section at $x = 40,5$ m, shown in Figure 22, includes the effects of noncontinuous structures.

Figure 21 indicates that the HSD element can accurately trace fine linear mesh results, while the average nodal normal and more prominently shear stress values lack accuracy at the transition layers and significant peak stress values are undiscovered. The HSD formulation significantly outperforms semi-coarse linear mesh, as even with decreased element sizing, the vertical stress distribution shows a lack of coverage in critical transitory layers. Figure 21 b) indicates that coarse linear mesh is a viable modeling solution, but only if the stress distribution does not experience any stress discontinuities. Even a single discontinuity, such as in Figure 21 d), can create peak stress underestimation of approximately 30% in both coarse and semi-coarse mesh models.
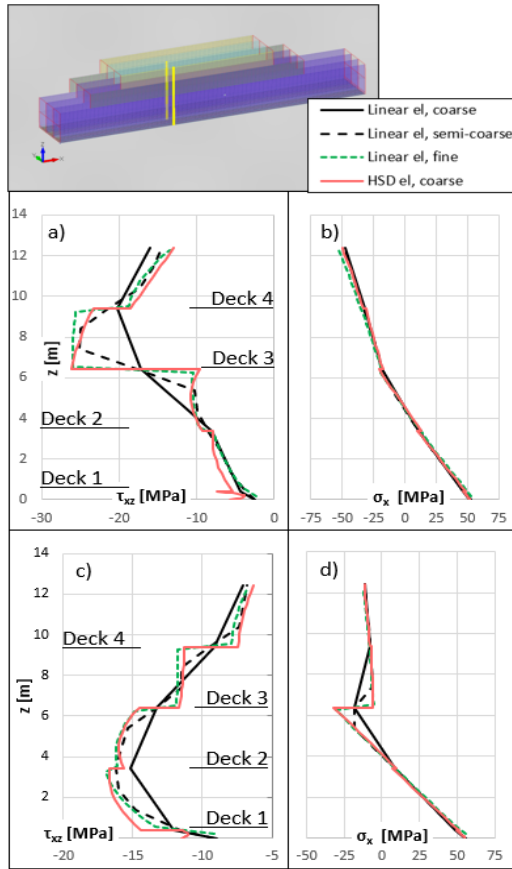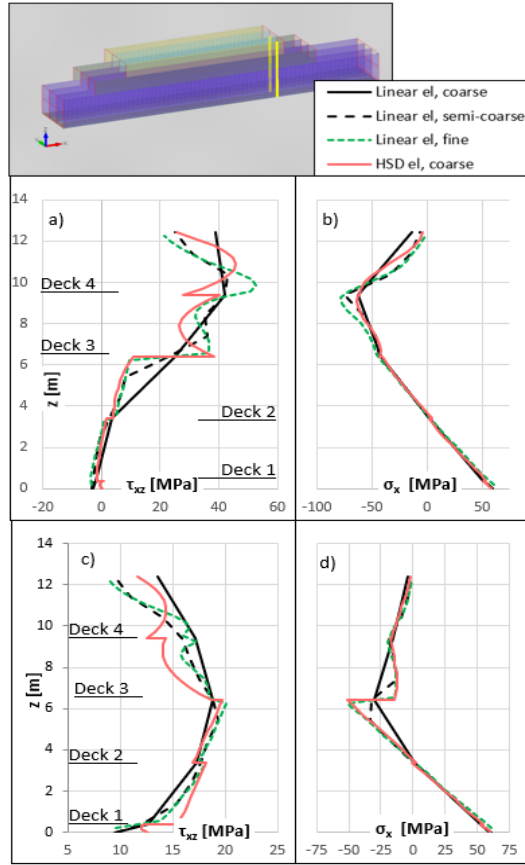
Figure 21. Vertical distributions at $x = 22{,}5$ m for a) shear stress in the inner bulkhead, b) normal stress in the inner bulkhead, c) shear stress in the outer shell, d) normal stress in the outer shell. [P2]

Although normal stress distributions close to structural discontinuities show good correlation, shear stress distributions in Figure 22 a) and Figure 22 c) exhibit bigger discrepancies as shear stress evaluation becomes more complicated in corner elements. Regardless of coarse linear mesh once again exhibiting less accurate shear stress distributions, the lowered accuracy of the HSD formulation suggests that element refinement would be beneficial.

Figure 22. Vertical distributions at $x = 40,5$ m for a) shear stress in the inner bulkhead, b) normal stress in the inner bulkhead, c) shear stress in the outer shell, d) normal stress in the outer shell. [P2]

5.3 Cruise ship model

The cruise ship model gives an overview of specifically shear stress distributions across multiple planes and cross-sections. The planes have been defined on critical deck layers, such as the main deck level, where thicker and stiffer hull structures transition into a recess shell that is weakened with openings and has thinner plating, the first cabin deck, where the recess shell expands outwards and transitions into cabin area shell, that is additionally weakened to accommodate modular cabin installments, and the cofferdam layer, where the shell and bulkhead structured are greatly diminished in length above the cofferdam. Two cross-sections show a significantly different shear stress behavior to further support the findings on the longitudinal distribution graphs. Global deflection and normal stress response have been omitted, as it is sufficiently proven that the HSD formulation can accurately predict global deflections and normal stress behavior. Shear stress is of special interest, as it is greatly affected by the simplifications made for the concept design model and has a larger impact from the introduction of the shear flow rate degree of freedom presented in this research.

Longitudinal distributions of shear stress are presented in a direction-specific format, where the vertical structures under investigation on the transition layer are further identified. Two separate comparative graphs have been presented in the figures. The low

41

approach demonstrates stress distributions, where the fine linear mesh presents results from the element under the transition layer, whereas the HSD formulation calculates the stress values at the edge for the element under the transition layer. The high approach conversely uses the elements above the transition layer for the fine linear mesh and the HSD formulation. Coarse linear mesh cannot separate stress distributions based on the approach direction and thus puts out identical distributions for both graphs.

Shear stress distribution analyses at the main deck level are shown in Figure 23 and Figure 24 In all graphs, the HSD formulation shows exceptional correlation to the fine linear mesh distribution. In addition to the general tracing, local stress maximums that are caused by proximity to structural discontinuities or weakened materials in bulkheads are well captured. Coarse linear mesh shows varying correlation, as the analysis at the bulkhead in Figure 23 illustrates the deficiency of the nodal averaging in layer transitions with the difference reaching up to 40% between the coarse and fine linear mesh distributions. Notably, the coarse linear mesh results in Figure 24 a) show a high correlation as only a single layer of vertical element stress is averaged.
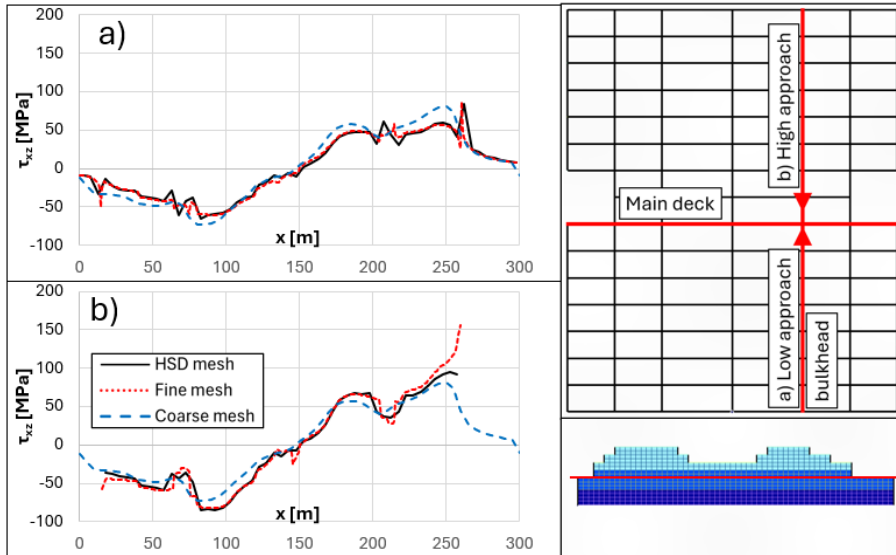
Figure 23. Longitudinal shear stress distribution in the bulkhead at the main deck level. [P3]
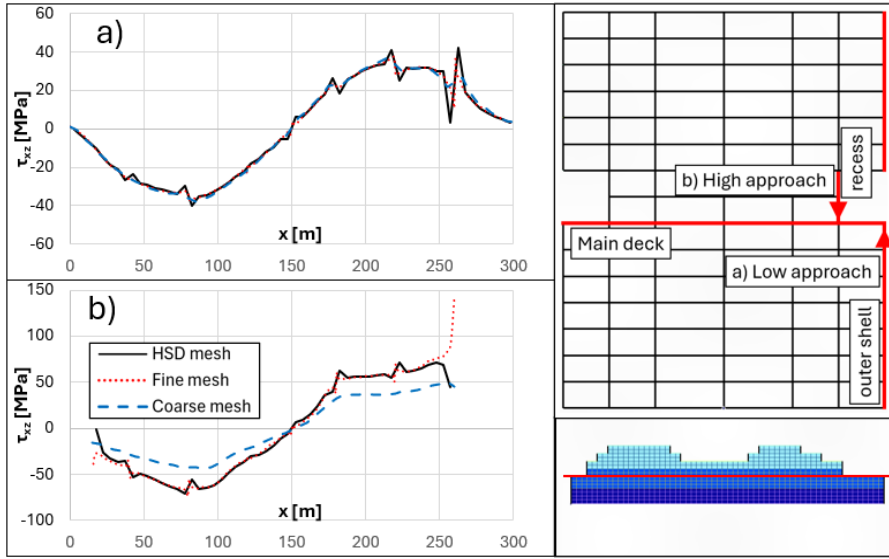
Figure 24. Longitudinal shear stress distribution in the hull outer shell and recess shell at main deck level. [P3]

Figure 25 shows the stress distributions at the cofferdam layer. Due to the proximity of geometric discontinuities, the stress distributions in this layer experience intense variance in the outer shell. Here, the HSD formulation captures the local maximums without losing any accuracy to the fine linear mesh, while the coarse linear mesh experiences significant accuracy drop-off near discontinuities. The maximum stress values near the structural ends at $x = 110 \ m$ and $x = 170$ m are underestimated by up to 75% for the coarse linear mesh and up to 20% for the coarse HSD mesh calculated in identical coordinates.
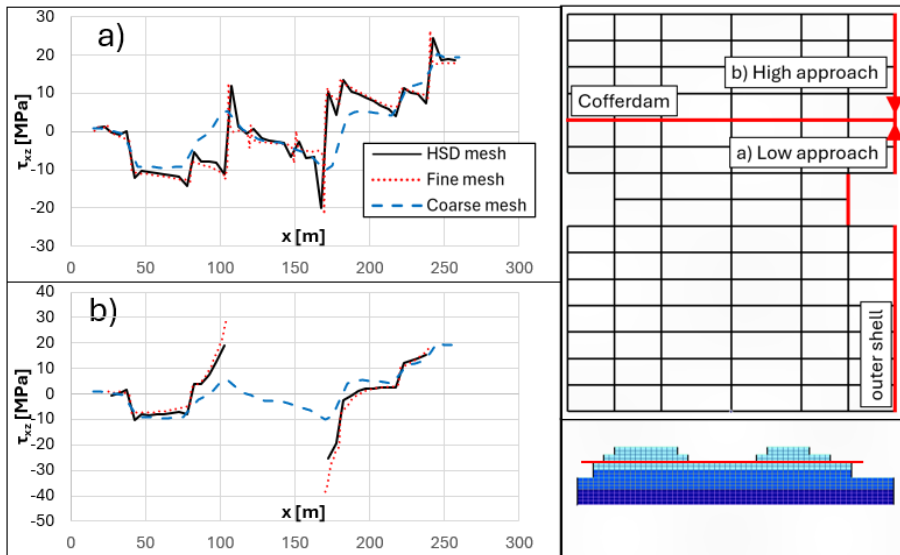
Figure 25. Longitudinal shear stress distribution in the outer shell and cofferdam level. [P3]

Cross-sections at $x = 52,5$ m and $x = 172,5$ m are additionally analyzed to better understand the accuracy that inter-elemental higher-order interpolation of stresses provides. In longitudinal distributions, singular elemental stress value has been used for the HSD formulation, as ship models have more elements longitudinally and shear stress variance within the element is less prominent. In vertical stress distribution analysis, the singular elemental stress values might often provide good accuracy, however, the discovery of maximum stress within the element often requires a higher-order approximation function.

Figure 26 gives an oversight of stress distributions in a cross-section without notable disturbances from structural discontinuities. In the inner bulkhead in Figure 26 a), the stress distributions show significant discontinuity only on the main deck level as the bulkhead thickness transitions from 10mm to 6mm thickness. The graph shows an overall good correlation between the mesh types and a notable difference at the transition, as the coarse linear mesh underestimates the maximum stress value by 15%.

Stress discontinuities at the main deck and cabin deck transitions are best visualized in outer shell structures in Figure 26 b). Here, the coarse linear mesh lacks accuracy as the stress values at the recess edges differ by up to 40% compared to the fine linear mesh. The HSD formulation shows very good accuracy and proves to be very capable of describing discontinuities along the whole vertical span of the cross-section.
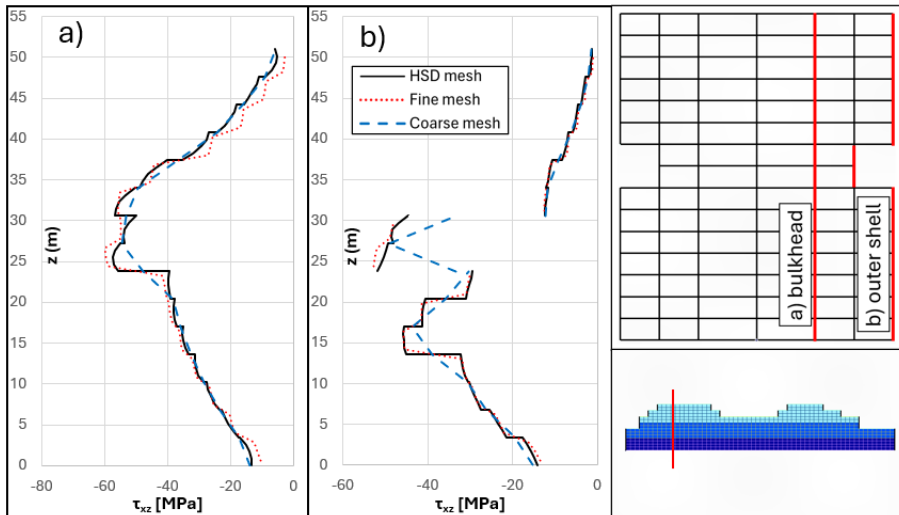

Figure 26. Vertical shear stress distribution at x = 52.5 m. [P3]

Figure 27 presents the stress distribution for a cross-section adjacent to structural discontinuities in the midship area. Proximity to the structural discontinuities in the cofferdam layer height at $z = 37,4$ m causes significant increase in shear stress that are accurately captured by the HSD formulation. Coarse mesh distribution shows how the peak stresses occurring within the element are completely missed resulting in a near 50% reduction in the predicted maximum stress values. The HSD formulation shows a slight overestimation of maximum stresses by 13% while providing a highly accurate stress distribution over the whole cross-section.
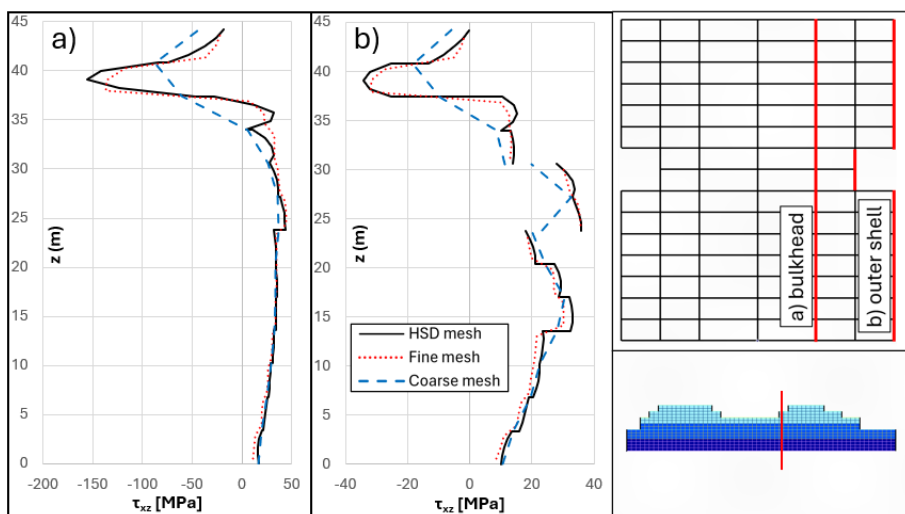
Figure 27. Vertical shear stress distribution at x = 172.5 m. [P3]

6 Discussion and conclusions

Structural analysis of ship structures follows closely the overall ship design process that is largely divided into three distinct stages: concept design, basic design, and detail design. In the concept design phase, the deck arrangement is solidified, and the major structural elements and the mainframe are defined. As the design stages are progressively longer and need more resources, the methods utilized in concept stage structural analysis need to provide as accurate data as possible with a limited amount of time and level of detail available.

The research in this thesis introduced first an asymmetric element description in [P1], where corner nodes described nodal displacements, while midside nodes on vertical edges described shear deformation at the corners. Although difficult to implement due to asymmetry, this theory can describe discontinuous stress at shared corner nodes between adjacent elements. The element description was validated on two planar model use cases that roughly represented multideck ship vertical structures. Firstly, a model with different layer lengths was used to simulate the interaction between a thick hull plating and a thinner superstructure. Secondly, with similar layer thicknesses, a model with openings was analyzed to validate the theory in areas affected by stress concentrations. The finite element analysis revealed a realistic shear and normal stress distribution for the proposed theory which significantly outperformed identically sized linear mesh when compared to fine linear mesh model results.

The theory was further developed into the higher-order shear deformation theory in [P2] and [P3], as it was favorable to rework the element descriptions into a system, where the nodal DOF vector is constant throughout the model. This was achieved by introducing an equilibrium shear flow rate DOF that would specifically ensure an accurate parametric description of shear stress. Separate element descriptions for vertical longitudinal, vertical transversal, and horizontal elements were created due to the restrictions to the size of the nodal DOF vector from the commercial software application. It was one of the main objectives of the thesis, to be able to apply the theory in commercial software as that would provide similar solver efficiency. Therefore, the proposed nodal DOF vector is limited to 6 variables consistent with the conventional displacement and rotation DOF allocation for classical plate elements.

Two analysis models have been introduced to validate the HSD formulation. The stepped box model in Paragraph 4.3 and originally presented in [P2] consists of horizontal and vertical longitudinal plating and introduces a shear-weak superstructure, where outer shell elements above the midplane have lowered thickness as well as lowered stiffness properties. This resembles a real-life superstructure structure, where plating thickness is reduced to a lower global center of mass as well as to facilitate the lowered importance of carrying bending stresses. The cruise ship model in Paragraph 4.4, originally presented in [P3], adds to the level of modeling detail and the resemblance of a real-life cruise ship. Design elements such as recess, double bottom, cofferdam, pillars, and transversal bulkheads are added. This model extensively incorporates weakened material definitions as horizontal structures introduce openings for elevator shafts or stairs and bulkheads introduce openings for passenger pathways. As local interaction between pillars and deck stiffening structures is not of major interest, pillars have been introduced into pillar line plate elements, with significant negative space within the element lowering the equivalent stiffness.

The objective of the analysis is to present a case for increased accuracy in models using the HSD formulation over a similarly sized linear element mesh. As concept design calculations in the maritime industry have a well-defined best practice for element sizing, where element dimensions are driven by deck height, main frame spacing, and the transversal distance between pillars or between a bulkhead and pillar line, the theory in this research does not seek to redefine those. It is investigated whether the use of higher-order shear deformation theory could be utilized in commercial software to achieve more accurate results without increasing modeling time and computational cost.

The results in Paragraphs 5.2 and 5.3 proved to universally increase the accuracy of the elastic response in the coarse mesh model that used the HSD formulation over traditional linear mesh formulation. Significant focus was put into investigating the longitudinal normal and shear stress distributions in critical planes, where the vertical structures transitioned in element thickness or element thickness and stiffness properties. The analysis in all cases showed that the HSD formulation can describe stresses at the transition layer depending on the directional approach. Coarse mesh formulation was significantly hampered by the nodal density as linear elements describe stress as a constant value within the element. These findings were further strengthened when analyzing vertical stress distributions, which clearly showed that maximum stress often occurs within elements, that could only be located with smaller element sizes or higher-order approaches. Coarse linear mesh lacked nodal density to locate such stress maximums and therefore the case for using the HSD theory over traditional uses of linear meshing is presented.

In practice, the HSD theory presented in this thesis enables an accurate elastic response in the conceptual design phase such that critical maximum stresses can be located and considered as early as possible. The method outperformed identically sized linear mesh in all applications and every cross-section and horizontal plane. Future developments in the development of the HSD theory include presenting a comprehensive unified theory, where elements use consistent element definitions that are transformed to fit the global positioning. In addition, an isoparametric approach would be needed to model outside of principal planes, which would increase the resemblance to real-life structures. Additionally, the theory would benefit from introducing torsional and out-of-plane response functionality. This method would also require a mass matrix definition to perform eigenvalue analyses that are of interest in the conceptual design phase. Finally, it would serve this theory greatly to develop full integration with commercial software to eliminate extra steps in data transferring and improve the applicability of the theory.

References

Andric, J., Žanic, V. 2010. The global structural response model for multi-deck ships in concept design phase. Ocean Engineering,, 37:688–704. DOI: 10.1016/j.oceaneng.2010.01.018

Avi, E., Lillemäe, I., Romanoff, J., Niemelä, A. 2015. Equivalent shell element for ship structural design. Ships Offshore Struct. 20(3):239–255. DOI: 10.1080/17445302.2013.819689

Bickford, W. B. 1982. A consistent higher order beam theory. Development in Theoretical and Applied Mechanics, SECTAM 11: 137–150.

Bleich, H. H. 1953. Nonlinear distribution of bending stresses due to distortion of the cross section. J. Appl. Mech., 20(1):95–104. DOI: 10.1115/1.4010600

Carrera, E., Antona, E. 1995. A class of two-dimensional theories for anisotropic multilayered plates analysis, Accademia delle Scienze.

Crawford, L. 1950. Theory of long ships' superstructure. Trans SNAME, 58:693–732.

DNV-GL. 2016. Direct strength analysis of hull structures in passenger ships. DNVGL-CG-0138.

Ghugal, Y. M., Sharma, R. 2009. A Hyperbolic shear deformation theory for flexure and vibration of thick isotropic beams. Int. J. Comp. Meth., 6(4):585–604. DOI: 10.1142/S0219876209002017

Ghugal, Y. M., Sharma, R. 2011. A refined shear deformation theory for flexure of thick beams. Lat. Am. J. Solids Stru., 8(2):183–195. DOI: 10.1590/S1679-78252011000200005

Hughes, OF. 1989. Ship structural design. Jersey city, New Jersey: Society of Naval Architects and Marine Engineers.

ISSC. 1997. Committee II.1 – quasi-static response. Proceedings of the 13th International Ship and Offshore Structures Congress; 1997 Aug 18–22; Trondheim, Norway. Oxford (England): Elsevier Science. p. 158–165.

Krishna Murthy, A. V. 1984. Towards a consistent beam theory, AIAA J., 22(6):811–816. DOI:10.2514/3.8685

Levinson, M. 1981. A new rectangular beam theory. J. Sound Vib., vol. 74, no. 1, pp. 81–87. DOI: 10.1016/0022-460X(81)90493-4

Morshedsoluk, F., Khedmati, M. R. 2016. Ultimate strength of composite ships' hull girders on the presence of composite superstructures. Thin-Walled Structures, 102:122–138, 2016. DOI: 10.1016/j.tws.2016.01.024

Naar, H. 2006. Ultimate strength of hull girder for passenger ships. Doctoral Dissertation, Helsinki University of Technology.

Naar, H., Varsta, P., Kujala, P. 2004. A theory of coupled beams for strength assessment of passenger ships. Mar. Struct., 17:590–611. DOI: 10.1016/j.marstruc.2005.03.004

Raikunen, J., Avi, E., Remes, H., Romanoff, J., Lillemäe-Avi, I., Niemelä, A. 2019. Optimisation of passenger ship structures in concept design stage. Ships Offshore Struct; 14(1):320–334. DOI: 10.1080/17445302.2019.1590947

Reddy, J. N. 1984. A simple Higher-Order Theory for Laminated Composite Plates. J. Appl. Mech., 51(4):745–752. DOI: 10.1115/1.3167719

Reddy, J. N. 1987. A generalization of two-dimensional theories of laminated composite plates. Commun Appl Numer Meth, 3(3):173–180. DOI: 10.1002/cnm.1630030303

Reddy, J. N. 2004. Mechanics of laminated composite plates and shells – theory and analysis, 2nd ed. Boca Raton (FL): CRC Press.

Rehan, J. 2017. One-dimensional Advanced Beam Models for Marine Structural Applications. Doctoral thesis, Politecnico di Torino. DOI: 10.6092/polito/porto/2680980

Rehfield, L. W., Murthy, P. L. N. 1982. Toward a new engineering theory of bending, Fundam. AIAA J., vol. 20, no. 5, pp. 693–699, 1982. DOI: 10.2514/3.7938.

Ringsberg, J. W., Saglam, H., Sarder, M. A., Ulfvarson, A. 2012. Lightweight design of offshore platform marine structures – optimization of weight to strength utilization of corrugated shell plating. Ships Offshore Struct. 9(1):38–53. DOI: 10.1080/17445302.2012.712005

Robbins, D. H., Reddy, J. N. 1991. Analysis of piezoelectrically actuated beams using a layer-wise displacement theory. Comput Struct, 41(2):265–279. DOI: 10.1016/0045-7949(91)90430-T

Romanoff, J., Varsta, P. 2007. Bending response of web-core sandwich plates. Compos Struct. 81:292–302. DOI: 10.1016/j.compstruct.2006.08.021

Romanoff, J., Remes, H., Varsta, P. 2013. Hull-superstructure interaction in optimised passanger ships. J. Ships Offshore Struct, 8:612–620. DOI: 10.1080/17445302.2012.675196

Romanoff, J., Karttunen, A., Varsta, P., Remes, H., Goncalves, B. R. 2020. A review on non-classical continuum mechanics with applications in marine engineering. Mech. Adv. Mater. Struct., 27(13), 1065–1075. https://doi.org/10.1080/15376494.2020.1717693

Teguh, P., Kõrgesaar, M., Jelovica, J., Tabri, K., Naar, H. 2021. Ultimate strength assessment of stiffened panel under uni-axial compression with non-linear equivalent single layer approach. Mar. Struct., 78: 103004.

Timoshenko, S. P. 1921. On the correction for shear of the differential equation for transverse vibrations of prismatic bars. Philos. Mag., series 6, pp. 742–746. DOI: 10.1080/14786442108636264

Toledano, A., Murakami, H. 1987. A high-order laminated plate theory with improved in-plane responses. Int. J. Solids and Struct., 23:111–131. DOI: 10.1016/0020-7683(87)90034-5

Toming, R., Kerge, E. H., Naar, H., Tabri, K., Romanoff, J., Remes, H. 2016. Hull and superstructure interaction using coupled beam method. Proceedings of PRADS2016, 4th-8th September, 2016, Copenhagen, Denmark, pp. 851–859.

Zanic, V., Andric, J., Prebeg, P. 2013. Design synthesis of complex ship structures. Ships Offshore Struct. 8:383–403. DOI: 10.1080/17445302.2013.783455

Appendix 1

Publication I

Taylor & Francis
Taylor & Francis Group

ORIGINAL ARTICLE

OPEN ACCESS
Check for updates

Toward the application of the layer-wise displacement theory in passenger ships—a quasi-static response

Mikk-Markus Imala[a], Hendrik Naar[a] (iD), Kristjan Tabri[a], and Jani Romanoff[b]

[a]Department of Civil Engineering and Architecture, Tallinn University of Technology, Tallinn, Estonia; [b]Department of Mechanical Engineering, Aalto University, Helsinki, Finland

ABSTRACT

This paper introduces an application of the layer-wise displacement theory for response analysis of multilayer ship girders. Quadrilateral, 6-node finite membrane elements are used for which 8 displacement degrees of freedom at corners, and 4 shear strain degrees of freedom at mid-side nodes, are defined. This approach enables accurate estimates of the shear strain between adjacent layers with different stiffness. A simple cantilever beam, non-uniform stepped girder with constant layer stiffness, and uniform girder with varying stiffness is used in the validation analysis. An excellent agreement between the fine mesh finite element model and the proposed model is observed.

1. Introduction

Today, a variety of marine structures such as tankers and cargo and single-deck ships are sufficiently accurately assessed at the preliminary stage with the simplest forms of beam analysis that describe the hull girders as a single slender beam; reviews of common structural rules for bulkers and tankers are presented by Yao [1], Sumi [2]. However, recent trends in structural design for ships have been introducing shear-weak and long, stepped, superstructures, changing the typical transfer of shear stresses to a more complex phenomenon as described by Naar et al. [3], Shi and Gao [4, 5], Romanoff et al. [6] and Morshensholuk and Khedmati [7]. Due to this complexity, today, the most widely used method for solving passenger ship response is the three-dimensional (3 D) finite element method (FEM) [8]. In addition to the high computational solution time, global finite element models are time-consuming to create. Therefore, analytical methods or coarse mesh finite element models are preferred in the early design stage where design time is limited, as described by Avi [9]. Mathematical analysis of ship hull girders was first introduced by A. N. Krylov at the start of the 20th century [10]. The hull and superstructure interaction methods using the beam theories were first introduced by Crawford et al. [11] by considering the shear and vertical coupling in a two-beam system through additional stress resultants (internal shear and vertical forces between beams). A similar approach is introduced by Bleich et al. [12], where the stresses in prismatic beams in a vertically coupled two-beam system were considered. A review paper of non-classical

continuum mechanics application in marine engineering by Romanoff et al. [13] suggested that the response of a shear-weak superstructure does not follow internally a typical shear force diagram that the entire hull-girder experiences. The paper offers two possible solutions. The first would be, to exploit non-classical continuum mechanics, and to add a micropolar correctional factor to a Timoshenko beam to estimate micropolar moments over the height of the beam, allowing the layerwise, internal variation, of shear stress resultants within the hull girder height and length. The second would exploit classical continuum mechanics such as a layer-wise formulation for the beam. The first of such layer-wise formulations was the linear Coupled Beam presented by Naar et al. [3]. The method uses shear and vertical coupling between layers to evaluate the response of multideck passenger ships. Toming et al. [14] investigated the interaction of hull and superstructure using the Coupled Beam method by implementing a piece-wise approach, where layers of a multideck ship are divided into beam segments for which the structural behavior is individually described using continuous coordinate functions to describe local structural discontinuities. Non-linear Coupled Beam theory was consequently presented by Naar [15] and Morshensholuk and Khedmati [7] to assess hull girder limit-states accounting for non-linearities arising from local buckling or yielding.

Today, most beam theory applications within the marine industry utilize the Euler-Bernoulli or Timoshenko beam theory [16] which either neglects or oversimplifies the shear behavior. The extensions to these practices in the marine structures' community could exploit the developments from

the solid mechanics community. Levinson [17], Bickford [18], Rehfield and Murthy [19], Krishna Murty et al. [20], Bhimaraddi and Chandrashekhara [21], and Baluch et al. [22] have presented parabolic shear deformation theories for beams using a higher variation of axial displacement in terms of height coordinate. Ghugal and Sharma [23] have proposed a variationally consistent hyperbolic shear deformation theory for thick beams and further refined the theory in [24]. A higher-order shear deformation theory was introduced by Reddy [25], where the in-plane displacement fields follow a third-order polynomial. Many of these beam theories have been extended to layer-wise theories, that can be applied when analyzing composite laminates or structures. These could be also applied in ships with shear-weak and stepped, long superstructures interacting with more rigid hulls deforming according to EB- or Timoshenko beam theories. An excellent overview of multilayer theories was published by Carrera [26]. The review focuses on the theories setting assumptions for the description of displacements in the cross-section's normal direction and the stresses in the thickness direction. To achieve interlaminar continuity, an equilibrium for the stresses in the thickness direction is assumed in Lekhnitskii multilayered theory [27], Ambartsumian multilayered theory [28] and the multilayered theory based on the Reissner mixed variational theorem [29]. Additionally, these theories have made several integral assumptions for a layer-wise approach such as the equilibrium of displacements in adjacent surfaces and third-order displacement field definitions used, for example, by Toledano and Murakami [30]. The layer-wise displacement theory of Reddy [31] assumes a displacement field that uses an independent approximation of variables in the thickness direction from in-plane approximations. A generalization of the layer-wise displacement theory is presented in Reddy's later research [32], where the approach is applied to beams. Carrera unified formulation (CUF) is an approach that generalizes polynomial expansion methods for beams, plates, and shells including laminated and multi fields loadings that has the potential to be applied in marine technology applications as shown by Rehan [33] for simple ship hull girders and global hull girder responses in terms of displacements. The potential of this formulation in the passenger ship context is providing the means to create refined higher-order models where the specific approximation type being used and the order to which the approximation is expanded are considered as the parametrically free problem inputs. The CUF has found many applications in both statics [34–37] and dynamics [38–40] on beams, plates and shells undergoing small and application with large displacements [41–43]. These works include originally classical papers [44–46] and recently also expansions to non-classical structural models and use-cases [47–49]. In the present paper context, the interest is in the early works which focus on beam stress analysis and related finite element formulations [34, 36, 37, 50] as the application to passenger ships calls for both and especially increased accuracy on the stress assessment.

This article includes reference data presented by Pagani et al. [37] that includes a novel hierarchical Legendre polynomial expansion model in addition to referencing analysis data using Taylor expansion models and classical beam theories. These advancements in beam theories have the potential for applications within the marine structures' community, in the analysis of complex hull girders such as in passenger ships.

This paper aims to bridge the gap between layer-wise theories typically used for composite laminates and extend their application toward the marine industry. The layer-wise method developed in this paper lends the assumptions for interlaminar continuity of displacements from the classical layer-wise displacement theory while introducing a novel membrane element definition that achieves the desired stress behavioral capabilities. In marine structures, in-plane shear stress over the height of a ship is often non-continuous due to the differences in plate thicknesses, secondary stiffening, and non-linear responses due to different failure modes in layers (e.g. local buckling, yielding). This characteristic is achieved with a novel finite element definition that in addition to in-plane displacements at element corner nodes, includes hybrid shear strain degrees of freedom (DOFs) in mid-side nodes in the ship height direction. The representation of the shear strain component values at the coordinates of the corner nodes as mid-side node DOFs enables an uncoupled description of shear stresses between vertically adjacent elements, which is necessary to describe the non-continuous nature of shear stress in adjacent structures, where topology or material properties vary. Axial displacement of the membrane element is approximated with a third-order polynomial through the ship height direction, whereas for the displacement in the ship height direction linear approximation is accurate enough. This formulation allows using large elements that can accurately approximate the displacements and normal and shear stresses that are of fundamental importance in the design of complex passenger ship hull girders, where the layers are thin, yet shear stresses can be significant and non-continuous. Thus, computational accuracy and efficiency are enhanced in comparison to the alternative 4- or 8-noded membrane elements. The presented method is validated in two stages. Firstly, a comparative analysis is performed on a layered cantilever beam for which the results are compared to an analysis performed by Pagani et al. [37]. In the article, the authors compared the results of various Carrera's Unified Formulation (CUF) models using hierarchical Legendre polynomial expansions and Taylor expansions. Secondly, the numerical results are compared between the presented method and finite element analysis using commercially available software with stepped and shear-weak hull girder models.

2. Higher-order coupled beam theory

2.1. Definition of variables

The method is described for a quadrilateral membrane element defined in the Cartesian coordinate system. The x-axis is aligned with the length l, and the y-axis with the height h, of the element. The finite element is defined with 6 nodes.
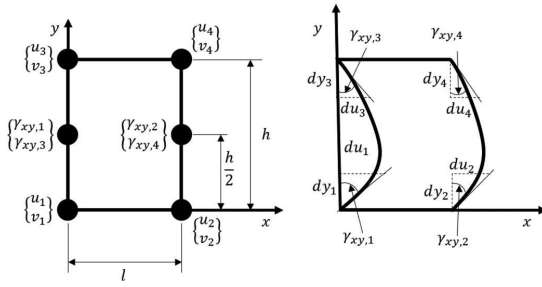
Figure 1. Beam element in the Cartesian coordinate system and explanation of shear strain DOFs.

The corner nodes, 1–4, are complemented with mid-side nodes in the y-direction, as shown in Figure 1.

DOFs in a membrane element, see Figure 1, are as follows:

- $u_1, \ldots, u_4$—displacement in x-axis direction at corner nodes
- $v_1, \ldots, v_4$—displacement in y-axis direction at corner nodes
- $\gamma_{yx,1}, \ldots, \gamma_{yx,4}$—shear strain due to horizontal shifting at the locations of the corner nodes.

As the stiffness properties of the layers in the passenger ship height direction often vary, it is necessary to uncouple shear strains between layers. Thus, the shear strain DOF is expressed in mid-side nodes leaving these variables uncoupled between adjacent elements in the ship height direction in the global stiffness matrix.

Ship structures are traditionally considered to act as thin-walled structures due to the high ratio between in-plane and thickness dimensions. Although significant i.e. for a single deck vibration analysis or a buckling analysis of a singular stiffened panel, out-of-plane behavior has little effect on the global response of a passenger ship.

2.2. Definition of the displacement field

The in-plane displacement fields $u(x, y)$ and $v(x, y)$ of the developed membrane element are individually expressed as a combination of polynomial functions in y direction as:

$$u(x_0, y) = A_{u,1}y^3 + B_{u,1}y^2 + C_{u,1}y + D_{u,1}, \tag{1}$$

$$v(x_0, y) = A_{v,1}y + B_{v,1}. \tag{2}$$

Equations (1) and (2) use the following relations to solve the polynomial equations at $x = 0$ for constants $A_{u,1}, B_{u,1}, C_{u,1}, D_{u,1}$ and $A_{v,1}, B_{v,1}$:

$$\begin{cases} u(0,0) = u_1 \\ \dfrac{\partial u}{\partial y}(0, \ 0) = \gamma_{yx,1} \\ u(0,h) = u_3 \\ \dfrac{\partial u}{\partial y}(0, \ h) = \gamma_{yx,3}, \end{cases} \tag{3}$$

$$\begin{cases} v(0,0) = v_1 \\ v(0,h) = v_3. \end{cases} \tag{4}$$

After inserting values of constants to Eqs. (1) and (2), regrouping for DOFs shown in Figure 1, and adding first-order approximations $\phi_1(x), \ \phi_2(x), \xi_1(y), \xi_2(y)$, displacement fields are described as a linear combination of shape functions and DOFs:

$$\begin{aligned} u(x,y) = {}&\psi_1(y)\phi_1(x)u_1 + \psi_1(y)\phi_2(x)u_3 + \psi_2(y)\phi_1(x)\gamma_{xy,1} \\ &+ \psi_2(y)\phi_2(x)\gamma_{xy,3} + \psi_3(y)\phi_1(x)u_2 + \psi_3(y)\phi_2(x)u_4 \\ &+ \psi_4(y)\phi_1(x)\gamma_{xy,2} + \psi_4(y)\phi_2(x)\gamma_{xy,4}, \end{aligned} \tag{5}$$

$$\begin{aligned} v(x,y) = {}&\xi_1(y)\phi_1(x)v_1 + \xi_1(y)\phi_2(x)v_3 + \xi_2(y)\phi_1(x)v_2 \\ &+ \xi_2(y)\phi_2(x)v_4, \end{aligned} \tag{6}$$

where

$$\begin{cases} \psi_1(y) = \dfrac{h^3 - 3hy^2 + 2y^3}{h^3} \\ \psi_2(y) = \dfrac{h^2y - 2hy^2 + y^3}{h^2} \\ \psi_3(y) = \dfrac{3hy^2 - 2y^3}{h^3} \\ \psi_4(y) = \dfrac{y^3 - hy^2}{h^2}, \end{cases} \tag{7}$$

$$\begin{cases} \xi_1(y) = 1 - \dfrac{y}{h} \\ \xi_2(y) = \dfrac{y}{h}, \end{cases} \tag{8}$$

$$\begin{cases} \phi_1(x) = 1 - \dfrac{x}{l} \\ \phi_2(x) = \dfrac{x}{l}. \end{cases} \tag{9}$$

or in vector form as:

$$u(x,y) = \{N\}^T\{u\}, \tag{10}$$

$$v(x,y) = \{V\}^T\{v\}. \tag{11}$$

where $\{N\}$ and $\{V\}$ are vectors of shape functions and $\{u\}$ and $\{v\}$ are vectors including nodal DOFs in axial and in the ship height direction as presented in Eqs. (5) and (6).

Ship structures are often composed of stiffened panels for which the orthotropic approach is needed as it enables modeling the stiffened panel as a homogeneous plate structure. The in-plane normal and shear strains are expressed as:

$$\begin{Bmatrix} \varepsilon_{xx} \\ \varepsilon_{yy} \\ 2\varepsilon_{xy} \end{Bmatrix} = \begin{Bmatrix} \dfrac{\partial u(x,y)}{\partial x} \\ \dfrac{\partial v(x,y)}{\partial y} \\ \dfrac{\partial u(x,y)}{\partial y} + \dfrac{\partial v(x,y)}{\partial x} \end{Bmatrix}$$

$$= \begin{Bmatrix} \left\{\dfrac{\partial N}{\partial x}\right\}^T\{u\} \\ \left\{\dfrac{\partial V}{\partial y}\right\}^T\{v\} \\ \left\{\dfrac{\partial N}{\partial y}\right\}^T\{u\} + \left\{\dfrac{\partial V}{\partial x}\right\}^T\{v\} \end{Bmatrix}. \tag{12}$$

2.3. Expression of potential energy

For an orthotropic material, where material axes (x_1, x_2, x_3) is coincident with coordinate axes (x, y, z), stress components according to the generalized Hooke's law are:

$$\left\{ \begin{array}{c} \sigma_{xx} \\ \sigma_{yy} \\ \sigma_{xy} \end{array} \right\} = \begin{bmatrix} C_{11} & C_{12} & 0 \\ C_{12} & C_{22} & 0 \\ 0 & 0 & C_{66} \end{bmatrix} \left\{ \begin{array}{c} \varepsilon_{xx} \\ \varepsilon_{yy} \\ 2\varepsilon_{xy} \end{array} \right\} \quad (13)$$

where C_{ij} are the elastic stiffnesses:

$$C_{11} = \frac{E_1}{(1 - \nu_{12}\nu_{21})}, \quad C_{22} = \frac{E_2}{(1 - \nu_{12}\nu_{21})}, \quad C_{12} = \nu_{12}C_{22}, \quad C_{66} = G_{12}. \quad (14)$$

Here, E_1 and E_2 are Young's moduli in the x and y directions, respectively, G_{12} is the in-plane shear modulus and ν_{12} and ν_{21} are Poisson ratios described as:

$$\nu_{21} = \nu_{12}\frac{E_2}{E_1}. \quad (15)$$

The potential strain energy equation for an orthotropic membrane element is written as:

$$\Pi = \frac{1}{2}\int_0^l\int_A (\sigma_{xx}\varepsilon_{xx} + \sigma_{yy}\varepsilon_{yy} + \sigma_{xy}2\varepsilon_{xy})dAdx - \int_0^l p_y v(x,y)dx$$

$$= \frac{1}{2}\int_0^l\int_A \left(C_{11}\varepsilon_{xx}^2 + C_{12}\varepsilon_{yy}\varepsilon_{xx} + C_{12}\varepsilon_{xx}\varepsilon_{yy} + C_{22}\varepsilon_{yy}^2 + C_{66}(2\varepsilon_{xy})^2\right)dAdx$$

$$- \int_0^l p_y v(x,y)dx, \quad (16)$$

for which the first variation of potential energy is:

$$\delta\Pi = \int_0^l\int_A \left(\frac{\partial \delta u}{\partial x}C_{11}\frac{\partial u}{\partial x}\right)dAdx + \int_0^l\int_A \left(\frac{\partial \delta v}{\partial y}C_{22}\frac{\partial v}{\partial y}\right)dAdx$$

$$+ \int_0^l\int_A \left(\frac{\partial \delta u}{\partial x}C_{12}\frac{\partial v}{\partial y}\right)dAdx + \int_0^l\int_A \left(\frac{\partial \delta v}{\partial y}C_{12}\frac{\partial u}{\partial x}\right)dAdx$$

$$+ \int_0^l\int_A \left(\frac{\partial \delta u}{\partial y}C_{66}\frac{\partial u}{\partial y}\right)dAdx + \int_0^l\int_A \left(\frac{\partial \delta u}{\partial y}C_{66}\frac{\partial v}{\partial x}\right)dAdx$$

$$+ \int_0^l\int_A \left(\frac{\partial \delta v}{\partial x}C_{66}\frac{\partial u}{\partial y}\right)dAdx + \int_0^l\int_A \left(\frac{\partial \delta v}{\partial x}C_{66}\frac{\partial v}{\partial x}\right)dAdx$$

$$- \int_0^l p_y \delta v(x,y)dx = 0, \quad (17)$$

where

$$\delta u = \{\delta a\}^T\{N\}, \quad (18)$$

$$\delta v = \{\delta b\}^T\{V\}. \quad (19)$$

$\{\delta a\}$ and $\{\delta b\}$ are vectors of variations of arbitrary constants. By substituting Eqs. (10), (11), (18), and (19) into Eq. (17) finite element equations become:

$$K11_{i,j} = \int_0^l\int_A \left(\left(\frac{d}{dx}N_i C_{11}\frac{d}{dx}N_j\right) + \left(\frac{d}{dy}N_i C_{66}\frac{d}{dy}N_j\right)\right)dAdx \quad (20)$$

$$K12_{i,j} = \int_0^l\int_A \left(\left(\frac{d}{dy}N_i C_{66}\frac{d}{dx}V_j\right) + \left(\frac{d}{dx}N_i C_{12}\frac{d}{dy}V_j\right)\right)dAdx \quad (21)$$

$$K21_{i,j} = \int_0^l\int_A \left(\left(\frac{d}{dx}V_i C_{66}\frac{d}{dy}N_j\right) + \left(\frac{d}{dy}V_i C_{12}\frac{d}{dx}N_j\right)\right)dAdx \quad (22)$$

$$K22_{i,j} = \int_0^l\int_A \left(\left(\frac{d}{dx}V_i C_{66}\frac{d}{dx}V_j\right) + \left(\frac{d}{dy}V_i C_{22}\frac{d}{dy}V_j\right)\right)dAdx \quad (23)$$

$$F_i = \int_0^l p_y V_i dx \quad (24)$$

The first variation of potential energy in Eq. (17) can be written using finite element equations from Eqs. (20) to (24) as:

$$\delta\Pi = \{\delta a\}^T\left([K11]\{u\} + [K12]\{v\}\right)$$

$$+ \{\delta b\}^T\left([K21]\{u\} + [K22]\{v\} - \{F\}\right)$$

$$= 0. \quad (25)$$

As $\{\delta a\}$ and $\{\delta b\}$ are vectors of arbitrary constants, the first variation can only equal to zero if the two components in brackets in Eq. (25) are individually equal to zero, thus:

$$\begin{bmatrix} [K11] & [K12] \\ [K21] & [K22] \end{bmatrix} \left\{ \begin{array}{c} u \\ v \end{array} \right\} = \left\{ \begin{array}{c} 0 \\ F \end{array} \right\}. \quad (26)$$

The vector of constants in Eq. (26) is rearranged and node-wise grouped as shown in Figure 1, where every node has 2 DOFs to facilitate the formulation of the global stiffness matrix and global loading vector as:

$$[K] \left\{ \begin{array}{c} u_1 \\ v_1 \\ u_2 \\ v_2 \\ \gamma_{xy,1} \\ \gamma_{xy,2} \\ \gamma_{xy,3} \\ \gamma_{xy,4} \\ u_3 \\ v_3 \\ u_4 \\ u_4 \end{array} \right\} = \{F\} \quad (27)$$
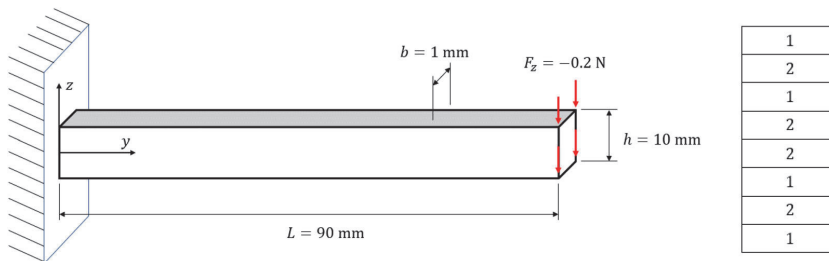
Figure 2. Cantilever beam model and layer configuration presented by Pagani et al. [37].

where $[K]$ and $\{F\}$ are the rearranged stiffness matrix and external loading vector respectively.

3. Models used for analysis

3.1. Cantilever beam model

Proof of concept analysis is performed on a cantilever beam model for which 8 separated layers defined with two different sets of material properties were incorporated. The reference data values for the analysis and the topological properties of the cantilever beam are presented in Pagani et al. [37]. The model in Figure 2 illustrates a thin cantilever beam with a varying configuration of layers to clearly distinguish the effects of changing material properties at layer transitions. The materials used to define the layers have identical transversal elastic modulus ($E_T = 1$ GPa), shear modulus ($G = 0.5$ GPa) and possion ratio ($\nu = 0.25$). Longitudinal elastic modulus is $E_{L1} = 30$ GPa for material 1 and $E_{L2} = 5$ GPa for material 2, see Figure 2 for layer configuration. The Poisson ratio and shear modulus is assumed to be constant in all directions. The cantilever beam is loaded at the free end from each cross-section corner with four equal loads summing up to $F_z = -0.2$ N. The model is located in a Cartesian coordinate system, where the y-axis is coincident with the longitudinal direction and the z-axis is coincident with the transversal direction of the model. See Figure 2 for the cantilever beam model and the layer configuration.

The cantilever beam is defined with 72 elements for the application of the presented theory, where every layer consists of 9 elements in the longitudinal direction resulting in 340 DOFs in total.

3.2. Hull girder models

To illustrate the layerwise application of the developed finite element in a marine context two case studies are considered. These are selected from Toming et al. [14] from which two simplified ship hull girders were considered,[1] one representing a stepped beam with uniform stiffness in layers and

another representing a uniform beam with varying stiffness in layers.

The stepped beam model consists of three adjacent membrane sections in the ship height direction with varying lengths. Each membrane section is described with a single layer of elements for the Quad6 and coarse mesh Quad4 models consisting of a total of 120 elements. Additionally, the Quad6 fine mesh model has been included in stepped beam model analysis to more accurately describe the corner effects by separating each membrane section into three layers of elements for which $h = 1000$ mm, thus consisting of a total of 360 elements. The fine mesh finite element (FE) model, used for comparison, consists of 9300 Quad4 membrane elements with dimensions of 200×200 mm, see Figure 3(a) for the model dimensions and the FE models. The model for the uniform beam with varying layer stiffness consists of three adjacent membrane sections with equal lengths, where the upper layers have large openings, which lower the overall stiffness of the structure and alter stress distributions. For the Quad6 and coarse mesh Quad4 models, the membrane sections with openings are both divided into three individual layers as the openings are described with offsets from beam surfaces consisting of a total of 520 elements. The fine mesh FE model consists of 23,000 Quad4 membrane elements with dimensions of 150×150 mm, see Figure 3(b) for the dimensions and the coarse FE model and Figure 3(d) for comparative size of the applied fine mesh. The elastic foundation has been used as boundary conditions for FE-models as it provides an accurate representation of a hull girder bending in waves, see Figure 3(c) for boundary principles.

Identical sinusoidal loading has been applied to all models to the bottom surface nodes excluding the elastic foundation elements as shown in Figure 4. The distributed loading is calculated as:

$$p(x) = p_0 * \cos\left(\frac{2\pi x}{L}\right), \tag{28}$$

where p_0 is load amplitude taken as 60N/mm, L is the total length of the model taken as 60 m. Material properties for elastic modulus and Poisson's ratio are used for FE membrane models: $E = 210$GPa, and $\nu = 0.3$ respectively. FE-analysis was performed using NX Nastran and FEMAP Academic version for Quad4 membrane models and Mathcad 15 software for Quad6 membrane models.

---

[1]The Cases B and C from the paper from the paper represent stepped beam with constant stiffness in layers and uniform beam with varying stifness in layers respectively. We exploit here the latter wording for physical insight.
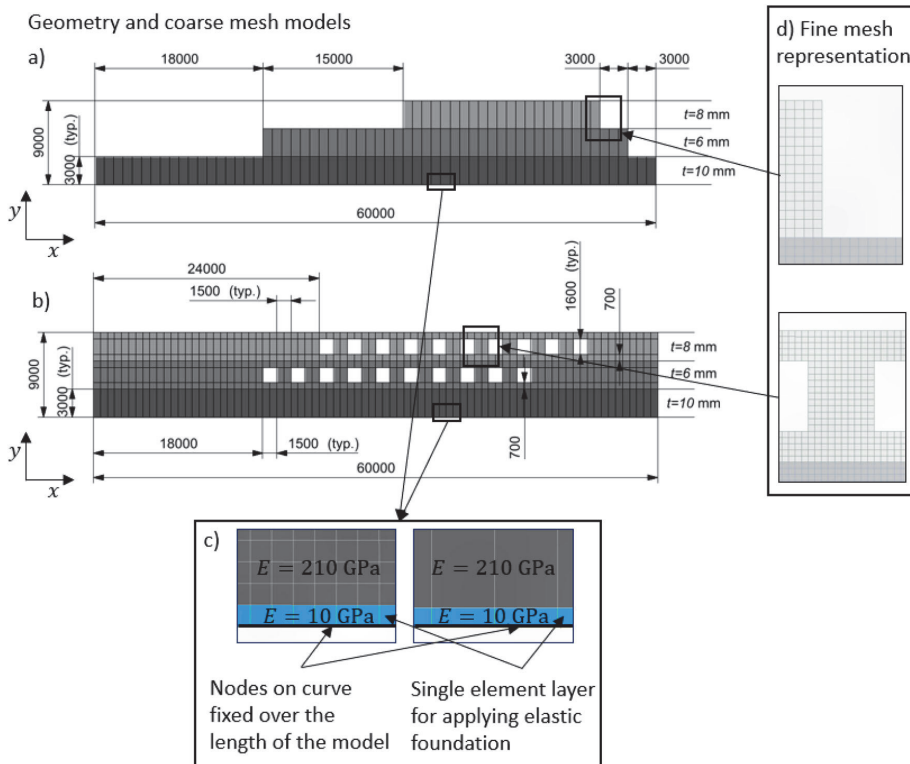
Figure 3. Geometry and FE plate models for (a) stepped beam with uniform layer stiffness and (b) uniform beam with varying layer stiffness, (c) principles of applying elastic foundation, and (d) detail views showing the comparative size of the used fine mesh.
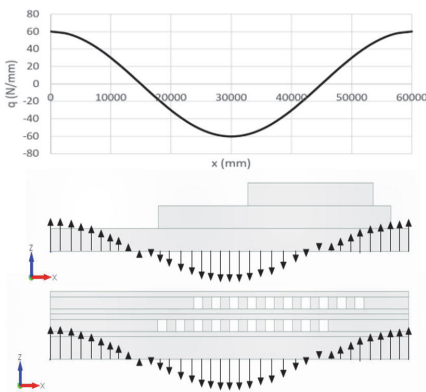

Figure 4. The applied distributed loading to the stepped beam with uniform stiffness and uniform beam with varying stiffness between layers.

4. Results

4.1. Cantilever beam model

The analysis performed for the 8-layer cantilever beam in [37] involved expressing the transversal distribution of normal and shear stress at the cross-section $y = L/2$. The

data from Figure 11 from the referenced article is lumped together depending on the coincidence of the results between the used methods. For the normal stress analysis, the Euler-Bernoulli beam method (EBBM), Timoshenko beam method (TBM), and the results for the 6-th order Taylor expansion model (TE N6) were lumped as well as the presented hierarchical Legendre expansion models (8HL2, 8HL4, 8HL6, 8HL8) with various n-th order ($n = 2, 4, 6, 8$) were lumped together due to highly coincident values. The layerwise theory presented in this article shows extremely coincident results to the hierarchical Legendre expansion models. These methods are distinguished by the ability to accurately describe the non-continuous stress behavior at the layer transitions compared to the analytical method, classical beam theory, and Taylor expansion model values, see Figure 5.

For shear stress comparison, hierarchical Legendre expansion model results (8HL2, 8HL4, 8HL6, 8HL8) are lumped, whereas the 6-th and 9-th order Taylor expansion models (TE N6, TE N9) produce highly different results. The presented layerwise theory results are similarly in good agreement with the results of the hierarchical Legendre expansion models, see Figure 6.
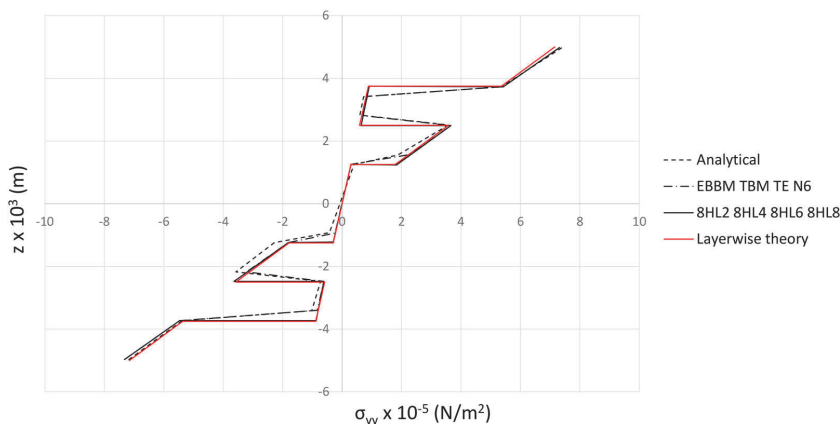
Figure 5. Transversal distribution of normal stresses at $y = L/2$ for the presented layerwise method and analyzed theories in [37].
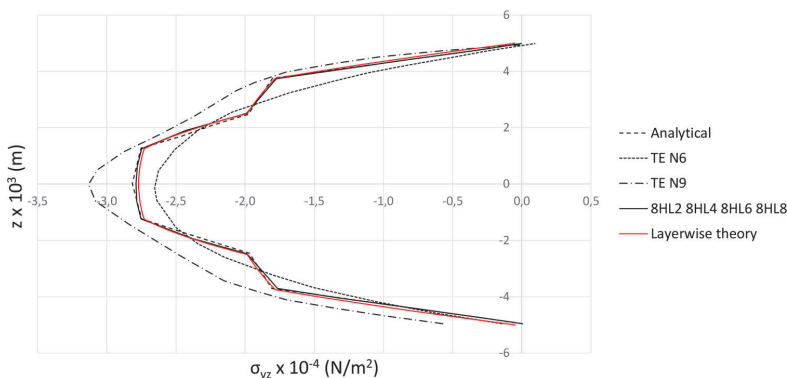

Figure 6. Transversal distribution of shear stresses at $y = L/2$ for the presented layerwise method and analyzed theories in [37].
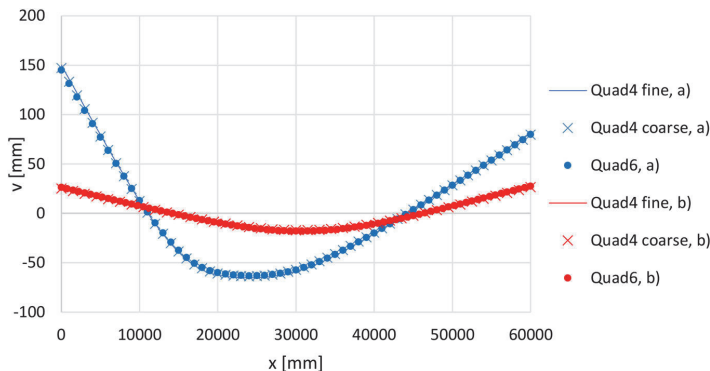

Figure 7. Comparison of deflections: (a) stepped beam, (b) unified beam with varying layer stiffnesses.

4.2. Hull girder models

Figure 7 presents the vertical displacements of different models. The global behavior of the models is in an agreement between the fine mesh and the Quad-6 mesh developed in this paper, and the coarse Quad-4 mesh.

4.2.1. Stress results for the stepped beam

For the stepped beam, the normal stresses have been analyzed in horizontal planes at $y = \frac{H}{3} = 3000$ mm and $y = \frac{2H}{3} = 6000$ mm and the top layer at $y = H = 9000$ mm, along girder length, see Figure 8. The stress results are in good agreement with the fine mesh results, however, peak stress
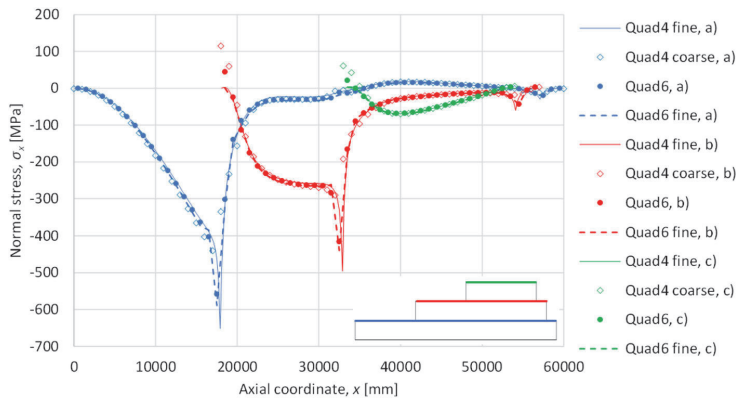
Figure 8. Longitudinal distribution of normal stress at (a) y = H/3 = 3000 mm, (b) y = 2H/3 = 6000 mm, (c) y = H = 9000 mm.
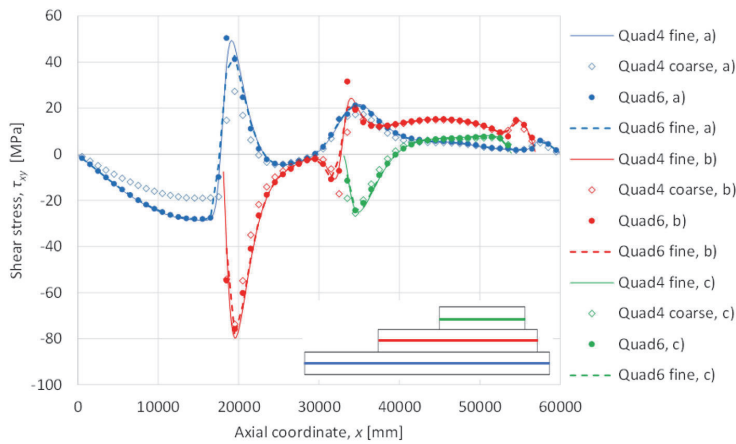
Figure 9. Longitudinal distribution of shear stress at (a) y = H/6 = 1500 mm, (b) y = H/2 = 4500 mm, (c) y = 5/6H = 7500 mm.
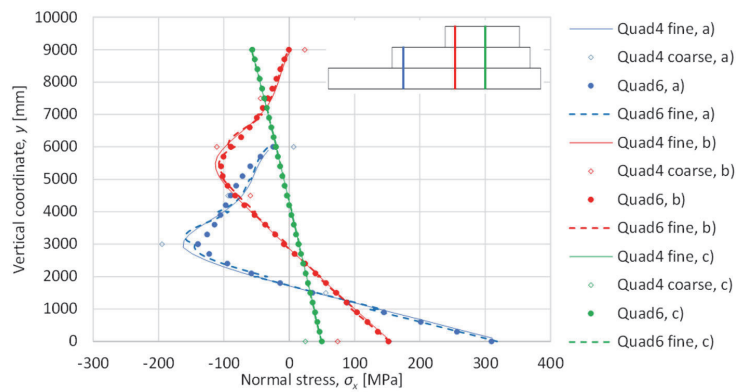

Figure 10. Normal stress, σ_x, in the stepped beam at (a) x = 19,500 mm, (b) x = 34,500 mm, (c) x = 43,500 mm.

values are generally underestimated with Quad6 and coarse mesh Quad4 model, Quad 6-results being considerably more accurate. In addition, stress decay at the vertical boundary edges is more accurately described with Quad6. When finer Quad-6 mesh is utilized the results are in excellent agreement with the fine mesh results.
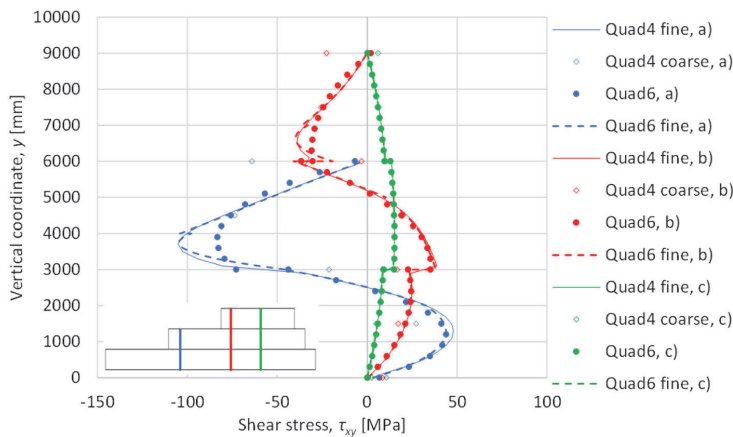
Figure 11. Shear stress of the stepped beam (a) x = 19,500 mm, (b) x = 34,500 mm, (c) x = 43,500 mm.
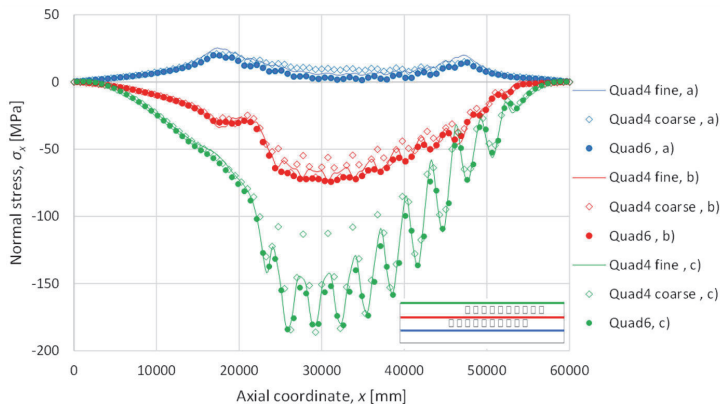
Figure 12. Longitudinal distribution of normal stress, σ_x, at (a) y = H/3 = 3000 mm, (b) y = 2H/3 = 6000 mm, (c) y = H = 9000 mm.
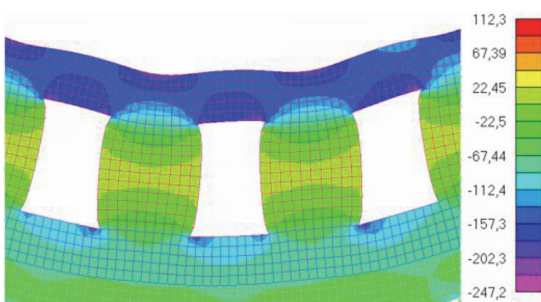
Figure 13. Local bending response in low bending stiffness areas for fine Quad4 element model of the uniform beam with varying layer stiffness.

The longitudinal distribution of shear stresses is analyzed in the middle layers of the layers at $y = \frac{H}{6} = 1500$ mm, $y = \frac{H}{2} = 4500$ mm and $y = \frac{5}{6}H = 7500$ mm, see Figure 9. In general Quad6 element models and fine mesh, model results are in agreement, whereas as coarse Quad4 element underestimates the stresses, especially at the discontinuities. Again

Quad6 mesh models show excellent performance in comparison to fine mesh when element size is decreased.

Cross-sections for analyzing the transversal distribution of normal stresses, σ_x, have been chosen such that both linear and higher-order distribution of stresses through the height of the girder can be seen. For the stepped beam with uniform stiffness in layers, cross-sections close to discontinuities at $x = \frac{L}{3.08} \approx 19,500$ mm and $x = \frac{L}{1.74} \approx 34,500$ mm and linearly behaving cross-section at $x = \frac{L}{1.38} \approx 43,500$ mm are chosen.

Vertical distribution of normal stress shows excellent agreement in all selected sections between Quad6 element model and fine mesh, with finer Quad6-mesh increasing the accuracy. In comparison, the fine mesh model does not agree with the coarse Quad4 mesh model at the places where significant discontinuities occur. This highlights the need for Quad6 element formulation, see Figure 10.

As an extension to the investigation on normal stresses, the distribution of shear stresses in the vertical direction shows highly corresponding results for fine mesh and coarse Quad6. Decreasing the Quad6 element size again improves
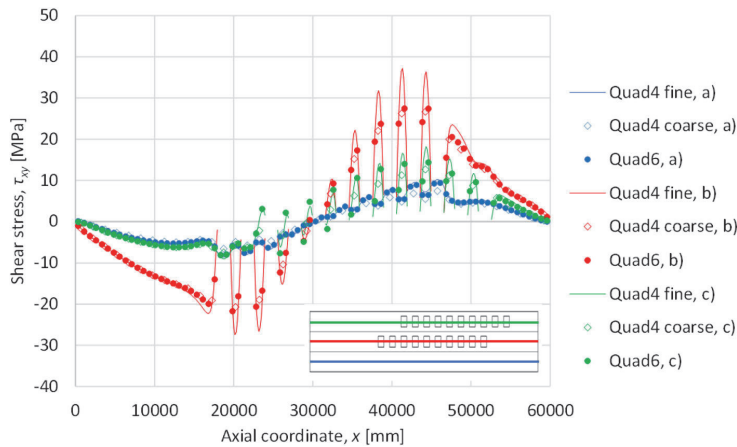
Figure 14. Longitudinal distribution of shear stress at (a) z = 1500 mm, (b) z = 4500 mm, (c) z = 7500 mm.
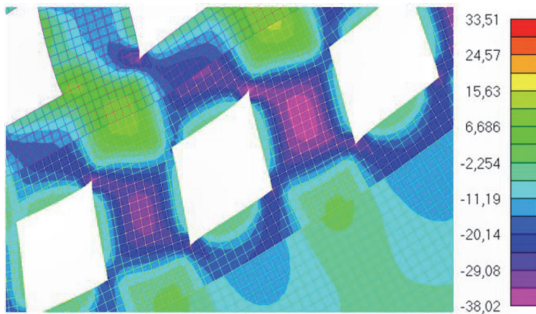

Figure 15. Local shear response in low shear stiffness areas for the fine Quad4 element model of the uniform beam with varying layer stiffness.

the agreement, while the same cannot be concluded from the Quad4 coarse mesh, see Figure 11. As in the case of normal stresses, this justifies the use of Quad6-formulation.

4.2.2. Stress results for the uniform beam with varying layer stiffness

The axial distribution of normal stresses, σ_x, in the uniform beam with varying layer stiffness shows overall good correspondence between the fine-, Quad6- and Quad4-meshes, see Figure 12. The Quad6 element model describes the oscillation of stress highly accurately when compared to the fine mesh model, while the coarse Quad4 element model overestimates the oscillation amplitude at the midspan region in planes y = 2H/3 and y = H. The oscillating normal stresses form most prominently in the top surface as openings introduce areas along the free edges, where bending stiffness is lowered and secondary shear strain occurs. In a global bending situation, the free edge geometry of openings is deformed and the structures on top of openings provide an opposite local bending response, see Figure 13.

When the shear stresses are observed in the middle of the layers, the Quad6 and Quad 4 results are in agreement with the fine mesh results, except for the peak values, see

Figure 14. As Figure 15 shows in the vicinity of openings, the traction-free stress conditions cannot be accurately described with the Quad6 or Quad4 element models. These discrepancies can be addressed by decreasing element dimensions in stress-critical areas in sub-models.

For the unified beam with varying stiffness in layers, cross-sections close to discontinuities at $x = \frac{L}{1.38} \approx 43,875$ mm, in the middle of a shear weak section at $x = \frac{L}{2.42} \approx 24,750$ mm and linearly behaving cross-section at $x = \frac{L}{4.10} \approx 14,625$ mm are chosen. Transversal distributions of normal stresses for the unified beam with varying stiffness in layers show excellent agreement between Quad6 and fine mesh models, see Figure 16. The Quad6 element model describes normal stress as a continuous function throughout the cross-sections as well as the effects of openings in high detail. Results for the coarse Quad4 element model are more scattered, especially for the cross-sections with openings.

In the same way, the shear stresses in the ship height direction are in agreement between the Quad6 and fine mesh models, while the coarse Quad 4 element model has difficulties modeling the fine mesh results, see Figure 17.

5. Concluding remarks

This paper introduced an application for the layer-wise displacement theory to evaluate displacements and stress distributions in layer-wise models with changing material and topological parameters as are present in the marine industry in passenger ships with long superstructures. This application creates a need for a 6-node finite membrane element with two displacement DOFs in corner nodes and two shear strain DOFs in mid-side nodes of transverse edges. Similar to classical 4-node membrane elements, these developed elements can be used to describe complex membrane structures. This approach generates a realistic distribution of normal and shear stresses in the hull girder. We have presented two case studies for the developed element to express the applicability in areas of discontinuous stepped layers, areas of openings or shear-weak sections and areas of
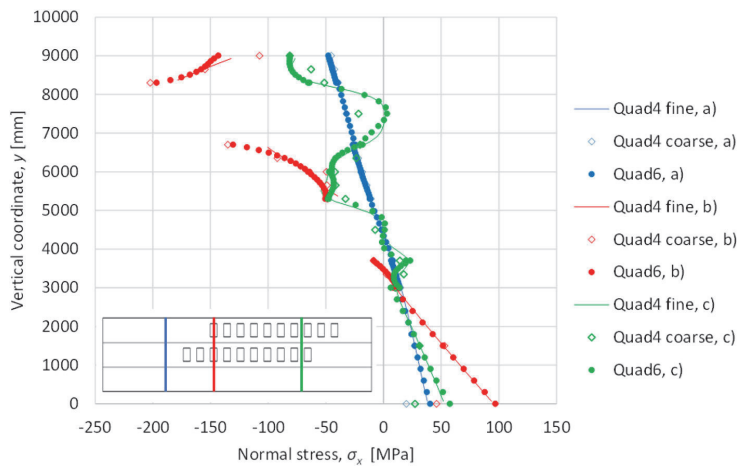
Figure 16. Vertical distribution of normal stress in cross-sections (a) x = 14,625 mm, (b) x = 24,750 mm, (c) x = 43,875 mm.
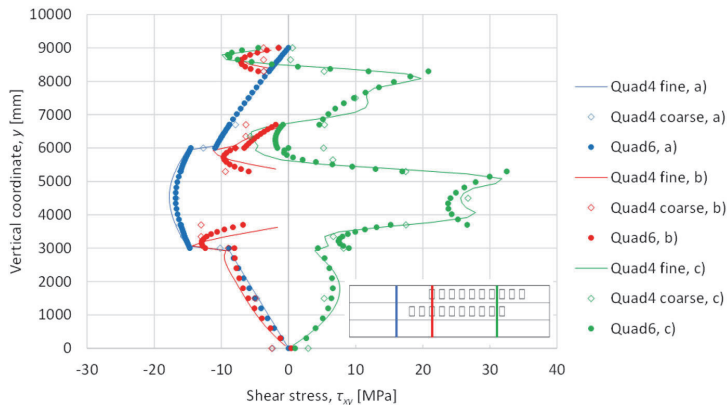

Figure 17. Vertical distribution of shear stress in cross-sections (a) x = 14,625 mm, (b) x = 24,750 mm, (c) x = 43,875 mm.

continuous structures. In real-world marine applications, these resemble hull and superstructure transitions and superstructure openings.

Simple cantilever analysis provided insight into the capabilities of the presented layerwise theory in comparison to a variety of classical theories and Carrera's unified formulations analyzed in [37] using a selection of expansion models. The presented layerwise method was highly coincident with the hierarchical Legendre expansion models presented in [37] being able to accurately describe stress behavior in a cross-section with varying stiffness regions. In addition, the formulation proved highly beneficial in problems typical for passenger ships in which stress analysis is of great importance. In areas of continuous structures, but with high stiffness variations between layers, the formulation showed excellent agreement in displacements and normal and shear stresses in comparison to the fine mesh FEA, the agreement improving with decreased element size. In the vicinity of discontinuities for stepped layers, the new formulation provides very accurate results in comparison to the fine mesh.

Underestimation of peak shear stresses with the large Quad6 elements became evident in the ship height direction, in the vicinity of the layer discontinuities. However, it was shown that decreasing the element size increases the accuracy. In shear-weak regions, the new Quad6 formulation similarly provided very accurate and better results than the Quad4 coarse mesh.

In practice, this formulation allows naval architects to perform initial stress analysis of passenger ship structures with improved accuracy. The method presented in this paper serves as an alternative method for detailed 3D FEM with good accuracy and low computational cost. In addition to the static response of structures, the lowest natural frequencies of ship structures and hull girders play a significant role in early-stage ship design. In future work, it would be beneficial to extend the method to estimate the global dynamic response of the passenger structure by continuing the work of Rehan [33]. Also, the recent non-classical continuum mechanics formulations [51] should be investigated further to define the roles of symmetric and antisymmetric

shear strain formulations more clearly in the passenger ship context.

Acknowledgments

ORCID

Hendrik Naar 🆔 http://orcid.org/0000-0003-2221-7684

References

[1] T. Yao, Hull girder strength, Mar. Struct., vol. 16, no. 1, pp. 1–13, 2003. DOI: 10.1016/S0951-8339(02)00052-7.

[2] Y. Sumi, Structural safety of ships developed by lessons learned from the 100-year history of break-in-two accidents, Mar. Struct., vol. 64, pp. 481–491, 2019. DOI: 10.1016/j.marstruc.2018.12.003.

[3] H. Naar, P. Varsta, and P. Kujala, A theory of coupled beams for strength assessment of passenger ships, Mar. Struct., vol. 17, no. 8, pp. 590–611, 2004. DOI: 10.1016/j.marstruc.2005.03.004.

[4] G. Shi and D. Gao, Analysis of hull girder ultimate strength for cruise ship with multi-layer superstructures, Ships Offshore Struc., vol. 14, no. 7, pp. 698–708, 2019. DOI: 10.1080/17445302.2018.1552548.

[5] G. Shi and D. Gao, Model experiment of large superstructures' influence on hull girder ultimate strength for cruise ships, Ocean Eng., vol. 222, p. 108626, 2021. DOI: 10.1016/j.oceaneng.2021.108626.

[6] J. Romanoff, et al., Hull-superstructure interaction in optimised passanger ships, J. Ships Offshore Struct., vol. 8, no. 6, pp. 612–620, 2013. DOI: 10.1080/17445302.2012.675196.

[7] F. Morshedsoluk and M. R. Khedmati, Ultimate strength of composite ships' hull girders on the presence of composite superstructures, Thin-Walled Struct., vol. 102, pp. 122–138, 2016. DOI: 10.1016/j.tws.2016.01.024.

[8] T. Yao, et al., Ultimate Strength (Committee III.1), 16th International Ship and Offshore Structures Congress, vol. 1, 2006.

[9] E. Avi, Equivalent shell element for passenger ship structural design, Doctoral Dissertation, Aalto University, 2021.

[10] S. P. Timoshenko, History of the Strength of Materials, McGraw-Hill, New York, pp. 434–439, 1953.

[11] L. Crawford, Theory of long ships' superstructure, Trans. SNAME., vol. 58, pp. 693–732, 1950.

[12] H. H. Bleich, Nonlinear distribution of bending stresses due to distortion of the cross section, J. Appl. Mech., vol. 20, no. 1, pp. 95–104, 1953. DOI: 10.1115/1.4010600.

[13] J. Romanoff, A. T. Karttunen, P. Varsta, H. Remes, and B. R. Goncalves, A review on non-classical continuum mechanics with applications in marine engineering, Mech. Adv. Mater. Struct., vol. 27, no. 13, pp. 1065–1075, 2020. DOI: 10.1080/15376494.2020.1717693.

[14] R. Toming, E. H. Kerge, H. Naar, K. Tabri, J. Romanoff, and H. Remes, Hull and superstructure interaction using coupled beam method, Proceedings of PRADS2016, 4–8 September, Copenhagen, Denmark, pp. 851–859, 2016.

[15] H. Naar, Ultimate strength of hull girder for passenger ships, Doctoral Dissertation, Helsinki University of Technology, 2006.

[16] S. P. Timoshenko, On the correction for shear of the differential equation for transverse vibrations of prismatic bars, Philos. Mag., Ser., vol. 6, pp. 742–746, 1921. DOI: 10.1080/14786442108636264.

[17] M. Levinson, A new rectangular beam theory, J. Sound Vib., vol. 74, no. 1, pp. 81–87, 1981. DOI: 10.1016/0022-460X(81)90493-4.

[18] W. B. Bickford, A consistent higher order beam theory, Development in Theoretical and Applied Mechanics, SECTAM, vol. 11, pp. 137–150, 1982.

[19] L. W. Rehfield and P. L. N. Murthy, Toward a new engineering theory of bending, Fundam. AIAA J., vol. 20, no. 5, pp. 693–699, 1982. DOI: 10.2514/3.7938.

[20] A. V. Krishna Murty, Towards a consistent beam theory, AIAA J., vol. 22, no. 6, pp. 811–816, 1984. DOI: 10.2514/3.8685.

[21] A. Bhimaraddi and K. Chandrashekhara, Observations on higher order beam theory, J. Aerosp. Eng., vol. 6, no. 4, pp. 408–413, 1993. DOI: 10.1061/(ASCE)0893-1321(1993)6:4(408).

[22] M. H. Baluch, A. K. Azad, and M. A. Khidir, Technical theory of beams with normal strain, J. Eng. Mech., vol. 110, no. 8, pp. 1233–1237, 1984. DOI: 10.1061/(ASCE)0733-9399(1984)110:8(1233).

[23] Y. M. Ghugal and R. Sharma, A hyperbolic shear deformation theory for flexure and vibration of thick isotropic beams, Int. J. Comput. Methods, vol. 06, no. 04, pp. 585–604, 2009. DOI: 10.1142/S0219876209002017.

[24] Y. M. Ghugal and R. Sharma, A refined shear deformation theory for flexure of thick beams, Lat. Am. J. Solids Struct., vol. 8, no. 2, pp. 183–195, 2011. DOI: 10.1590/S1679-78252011000200005.

[25] J. N. Reddy, A simple higher-order theory for laminated composite plates, J. Appl. Mech., vol. 51, no. 4, pp. 745–752, 1984. DOI: 10.1115/1.3167719.

[26] E. Carrera, Historical review of Zig-Zag theories for multilayered plates and shells, Appl. Mech. Rev., vol. 56, no. 3, pp. 287–308, 2003. DOI: 10.1115/1.1557614.

[27] S. G. Lekhnitskii, Strength calculation of composite beams, Vestnik Inzhen. i Tekhnikoc., no. 9, 1935.

[28] S. A. Ambartsumian, Theory of Anisotropic Shells, NASA TTF-118, 1964.

[29] E. Reissner, On a mixed variational theorem and on a shear deformable plate theory, Int. J. Numer. Methods Eng., vol. 23, no. 2, pp. 193–198, 1986. DOI: 10.1002/nme.1620230203.

[30] A. Toledano and H. Murakami, A high-order laminated plate theory with improved in-plane responses, Int. J. Solids Struct., vol. 23, no. 1, pp. 111–131, 1987. DOI: 10.1016/0020-7683(87)90034-5.

[31] J. N. Reddy, A generalization of two-dimensional theories of laminated composite plates, Commun. Appl. Numer. Methods, vol. 3, no. 3, pp. 173–180, 1987. DOI: 10.1002/cnm.1630030303.

[32] D. H. Robbins and J. N. Reddy, Analysis of piezoelectrically actuated beams using a layer-wise displacement theory, Comput. Struct., vol. 41, no. 2, pp. 265–279, 1991. DOI: 10.1016/0045-7949(91)90430-T.

[33] J. Rehan, One-dimensional advanced beam models for marine structural applications, Doctoral thesis, Politecnico di Torino, 2017. DOI: 10.6092/polito/porto/2680980.

[34] A. Catapano, G. Giunta, S. Belouettar, and E. Carrera, Static analysis of laminated beams via a unified formulation, Compos. Struct., vol. 94, no. 1, pp. 75–83, 2011. DOI: 10.1016/j.compstruct.2011.07.015.

[35] A. J. M. Ferreira, et al., Analysis of thick isotropic and cross-ply laminated plates by generalized differential quadrature method and a Unified Formulation, Compos. B., vol. 58, pp. 544–552, 2014. DOI: 10.1016/j.compositesb.2013.10.088.

[36] M. Filippi, E. Carrera, and A. M. Zenkour, Static analyses of FGM beams by various theories and finite elements, Compos. B, vol. 72, pp. 1–9, 2015. DOI: 10.1016/j.compositesb.2014.12.004.

[37] A. Pagani, A. G. de Miguel, M. Petrolo, and E. Carrera, Analysis of laminated beams via Unified Formulation and Legendre polynomial expansions, Compos. Struct., vol. 156, pp. 78–92, 2016. DOI: 10.1016/j.compstruct.2016.01.095.

[38] E. Carrera, M. Petrolo, and P. Nali, Unified formulation applied to free vibrations finite element analysis of beams with arbitrary

section, Shock Vib., vol. 18, no. 3, pp. 485–502, 2011. DOI: 10.3233/SAV-2010-0528.

[39] E. Carrera, F. Miglioretti, and M. Petrolo, Computations and evaluations of higher-order theories for free vibration analysis of beams, J. Sound Vib., vol. 331, no. 19, pp. 4269–4284, 2012. DOI: 10.1016/j.jsv.2012.04.017.

[40] A. Pagani, M. Boscolo, J. R. Banerjee, and E. Carrera, Exact dynamic stiffness elements based on one-dimensional higher-order theories for free vibration analysis of solid and thin-walled structures, J. Sound Vib., vol. 332, no. 23, pp. 6104–6127, 2013. DOI: 10.1016/j.jsv.2013.06.023.

[41] A. Pagani and E. Carrera, Large-deflection and post-bucking analysis of laminated composite beams by Carrera Unified Formulation, Compos. Struct., vol. 170, pp. 40–52, 2017. DOI: 10.1016/j.compstruct.2017.03.008.

[42] A. Pagani, R. Augello, and E. Carrera, Frequency and mode change in the large deflection and post-buckling of compact and thin-walled beams, J. Sound Vib., vol. 432, pp. 88–104, 2018. DOI: 10.1016/j.jsv.2018.06.024.

[43] B. Wu, A. Pagani, M. Filippi, W. Q. Chen, and E. Carrera, Large-deflection and post-bukling analyses of isotropic rectangular plates by Carrera Unified Formulation, Int. J. Non Linear Mech., vol. 116, pp. 18–31, 2019. DOI: 10.1016/j.ijnonlinmec.2019.05.004.

[44] E. Carrera and E. Antona, A class of two-dimensional theories for anisotropic multilayered plates analysis, Accademia delle Scienze, 1995.

[45] E. Carrera, Evaluation of layerwise mixed theories for laminated plates analysis, AIAA J., vol. 36, no. 5, pp. 830–839, 1998. DOI: 10.2514/2.444.

[46] E. Carrera, Developments, ideas, and evaluations based upon Reissner's Mixed Variational Theorem in the modeling of multilayered plates and shells, Appl. Mech. Rev., vol. 54, no. 4, pp. 301–329, 2001. DOI: 10.1115/1.1385512.

[47] E. Carrera, M. Filippi, and E. Zappino, Free vibration analysis of rotating composite blades via Carrera Unified Formulation, Compos. Struct., vol. 106, pp. 317–325, 2013. DOI: 10.1016/j.compstruct.2013.05.055.

[48] E. Carrera and E. Zappino, Carrera unified formulation for free-vibration analysis of aircraft structures, AIAA J., vol. 54, no. 1, pp. 1–13, 2015. DOI: 10.2514/1.J054265.

[49] R. B. Bharati, M. Filippi, P. K. Mahato, and E. Carrera, Flutter analysis of llaminated composite structures using Carrera Unified Formulation, Compos. Struct., vol. 253, no. 1, p. 112759, 2020. DOI: 10.1016/j.compstruct.2020.112759.

[50] A. Pagani and E. Carrera, Unified formulation of geometrically nonlinear refined beam theories, Mech. Adv. Mater. Struct., vol. 25, no. 1, pp. 15–31, 2018. DOI: 10.1080/15376494.2016.1232458.

[51] E. Carrera and V. V. Zozulya, Carrera unified formulation (CUF) for the micropolar beams: Analytical solutions, Mech. Adv. Mater. Struct., vol. 28, no. 6, pp. 583–607, 2021. DOI: 10.1080/15376494.2019.1578013.

Appendix 2

Publication II

Imala, M. M., Naar, H., & Tabri, K. 2025. Higher-order shear deformation formulation for the structural response of a multideck ship. Ships and Offshore Structures, 1–26. DOI: 10.1080/17445302.2025.2507714

Taylor & Francis
Taylor & Francis Group

🔓 OPEN ACCESS   Check for updates

Higher-order shear deformation formulation for the structural response of a multideck ship

Mikk-Markus Imala 🔟, Hendrik Naar and Kristjan Tabri

Tallinn University of Technology, School of Engineering, Tallinn, Estonia

ABSTRACT

This paper presents a higher-order shear deformation (HSD) finite element formulation for evaluating the global static response of passenger ship hull girders. The method aims to provide stress analysis with improved accuracy in complex ship structures with varying topology while maintaining low computational costs. This formulation introduces definitions for vertical and horizontal 4-node membrane elements with constant nodal degree-of-freedom mapping. The approach was tested on a simply supported beam model and a stepped box model with a shear-weakened superstructure. The results showed excellent agreement with the fine mesh linear analysis, particularly in stress distributions at the topological and parametrical transition layers. The HSD element outperformed identically dimensioned linear elements by capturing the discontinuities and maximum values in the stress distributions. This method provides an efficient solution for the 3D analysis in conceptual ship design, offering good accuracy at a low computational cost.

1. Introduction

Over the past decades, the size and structural complexity of passenger ships have substantially increased, leading to an overall increase in the size of scantlings, global dimensions, and structural mass. Harsh competition for customers drives ship owners to opt for more complex architectural solutions while striving for lightweight ships necessitating more accurate structural analysis in the conceptual design phase. Traditional rules of classification societies lack coverage for niche structural elements as evidenced by numerous specialised research. Shear-weak superstructures that introduce a more complex transfer of stresses are described by Naar et al (2004), Shi and Gao (2019, 2021), Romanoff et al. (2013), Morshensholuk (2016) and Bergström (2010). The feasibility of a new 425.5 m long megaship has been analysed by Tsitsilonis et al. (2018). Non-load-carrying passenger accommodation decks for modular cabin area design were analysed by Parmasto et al. (2013). The effects of utilising a superthin superstructure deck with smaller stiffener profiles on hull girder response were investigated by Lillemäe et al. (2014).

The challenges of complex structures have driven significant developments in theoretical approaches to structural analysis. Beam theories were first utilised by Crawford et al. (1950) to describe the hull and superstructure interaction by introducing additional stress resultants for vertical and shear coupling in a two-beam system. A similar coupled stress approach for a two-beam system was introduced by Bleich et al. (1953), For multi-deck passenger ships, Naar et al. (2004) presented a linear Coupled Beam method using shear and vertical coupling modeled as force-carrying springs between layers. The Coupled Beam method was implemented by Toming et al. (2016) to analyse the interaction of the hull and superstructure on simple 2D models. Yang et al. (2022) proposed a multibeam method to simplify stress distribution description in passenger ship superstructures. Romanoff et al. (2020) proposed a micropolar approach to evaluate global hull girder response for better local stress evaluation accuracy.

Numerous advancements for more accurate throughthickness shear stress descriptions have been developed in thick beam applications and composite laminate analysis. Parabolic shear deformation theories applied

to thick beams were developed by Bickford (1982), Krishna Murty et al. (1984), and Bhimaraddi et al. (1993). Ghugal and Sharma (2009, 2011) proposed a variationally consistent hyperbolic shear deformation theory for thick beams and introduced further refinements. Higher-order shear deformation theories for composite laminates were developed by Reddy (1984) and Toledano (1987) by utilising a third-order polynomial description for in-plane displacement. A noncontinuous approximation of variables in the thickness direction between plates was used in the layer-wise displacement theory presented by Reddy (1987) and later utilised on piezo-electrically actuated layered beams (1991).

Despite advances in beam theories and analytical models, 3D finite element analysis (FEA) is still the most preferred and suggested method for evaluating the structural response of passenger ships according to ISSC (1997) and DNV-GL (2016). As detailed mesh FEA is extremely costly, it is only used in small-scale ranges and during later design phases. In the conceptual design phase, classification society rules and modelling optimisation research have set best practices for element dimensions as utilising deck, web frame and pillar spacings minimises the number of unique orthotropic element definitions. Hughes (1989) utilised a modelling approach for the concept design phase, where shell structures comprised of two-layer elements, where the first layer represented the plating and the second layer represented the orthotropic stiffener layer, which were summed to create an element stiffness matrix. In modelling optimisation research, Ringsberg et al. (2012) and Raikunen et al. (2019) presented an optimisation method for passenger ships in the conceptual design phase by utilising an evolutionary optimisation algorithm and indirect constraint relaxation. Zanic et al. (2007) and Zanic et al. (2013) modeled stiffened panels with equivalent orthotropic elements in passenger ships. Romanoff and Varsta (2007) developed an equivalent element for a web-core sandwich panel based on the equivalent single-layer theory proposed by Reddy (2004). Avi et al. (2015) used the equivalent single-layer technique to describe a three-layer laminate element, where the characteristics of stiffeners and spacing can be implemented into the orthotropic material description. Teguh et al. (2021) performed stiffened panel ultimate strength analyses using an equivalent single-layer approach. A layer-wise displacement theory for passenger ships that introduced a higher-order shear deformation element formulation was presented by Imala et al. (2022). The formulation used midside nodes in the element description to describe the

discontinuous shear stress in element boundaries in topologically changing layers.

This paper aims to further add to modelling optimisation techniques in the ship concept design phase by introducing a formulation to increase the accuracy of the finite element (FE) formulation of the shell elements that have already been optimised to describe stiffening structures within the shell element definition by utilising orthogonal definitions. This paper presents a higher-order shear deformation method, improving on the formulation presented by Imala et al. (2022) for applications in the conceptual design phase of multideck passenger ships. The shear stress response is often discontinuous and exhibits a rapidly changing gradient owing to orthotropic varying material properties influenced by the varying plate thicknesses, secondary stiffening and openings, and structural discontinuities in the superstructure. Standard linear meshing falls short in analysing these areas due to the nodal averaging of stresses and the lack of accuracy within the element boundaries when using linear approximations. Higher accuracy can only be achieved by increasing nodal density thus making the analysis computationally more costly and significantly increasing the model preparation time as decreasing element size introduces new unique orthotropic element definitions. The method presented in this paper employs a dual-element formulation within a global six DOF nodal mapping system. The vertical element formulation utilises topologic and geometric data to define a shear flow DOF that ensures shear flow equilibrium in the shared edge between adjacent elements. The formulation for horizontal elements deploys a more simplified formulation as they are used to disperse stress between the vertical elements and are not of great interest in analysing inter-elemental stress distribution. An asymmetric approach to approximations is used for both element definitions to lower computational costs and the number of necessary nodal DOFs, while prioritising higher-order approximations for the equilibrium shear flow definition.

2. Higher-order shear deformation formulation

2.1. Motivation for the modified formulation

The layer-wise displacement theory presented by Imala et al. (2022) introduced an element definition that incorporated a six-node definition for a single element, where shear deformation variables at corner node locations were described in mid-side nodes on vertical
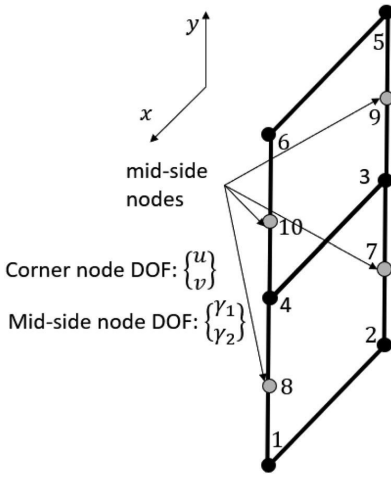
Figure 1. Layerwise displacement theory element variables presented by Imala et al. (2022).

edges, see Figure 1. This approach enabled discontinuous shear stress description between elements, however, the formulation lacks applicability, as asymmetric nodal positioning as well as inconsistent nodal DOF vectors are not easily implemented into a finite element analysis. In addition, the layerwise displacement theory formulation kept the simplified definition for shear deformation component $\partial v/\partial x$ in Eq. (1) as constant inter-elemental value as vertical displacement is linearly approximated in the x-axis direction between nodes.

$$\varepsilon_{xz} = \frac{\partial u(x, y)}{\partial y} + \frac{\partial v(x, y)}{\partial x}, \qquad (1)$$

where $u(x, y)$ is the planar longitudinal displacement field and $v(x, y)$ is the planar vertical displacement field.

The methodology in this paper presents a higher-order shear deformation formulation that operates in a constant nodal mapping system with six consistent DOFs per node, integrating a dual-element definition to distinguish between the vertical and horizontal element characteristics. A novel DOF describing nodal shear flow rate utilising geometric and material properties of neighboring elements enables a direction-specific solution that can evaluate discontinuous shear deformation and stress between elements. This variable definition ensures shear flow rate equilibrium along vertical element longitudinal edges by defining an equilibrium equation for elemental components in Eq. (6) and assigning the equilibrium shear flow rate value as the DOF value. In addition, the formulation further

improves the shear deformation evaluation by incorporating an increased order of magnitude to approximate the vertical displacement field.

The finite element equilibrium equations distinguish between horizontal and vertical elements, optimising computational efficiency. Horizontal elements employ a simplified formulation sufficient for their primary role in stress distribution, while vertical elements utilise the full stress-specific formulation with the equilibrium shear flow rate degree of freedom defined in Eq. (2).

2.2. Definition of equilibrium shear flow rate variable

Element definitions are presented in a ship coordinate system with longitudinal x-axis, transversal y-axis, and vertical z-axis. Although the longitudinal vertical elements and horizontal elements have unique sets of DOF approximations, every node is defined with similar 6 degrees of freedom in the global coordinate system:

u, v, w – translations respectively in x, y, z axis directions,

q – equilibrium shear flow rate

$\frac{\partial v}{\partial x}, \frac{\partial w}{\partial x}$ – deformations in the direction of the shared edge between the elements.

The equilibrium shear flow rate degree of freedom q is expressed as:

$$q = \left(\frac{\partial u}{\partial z} + \frac{\partial w}{\partial x}\right) t \left(\frac{G}{G_0}\right)$$
$$+ \left(\left(\frac{\partial u}{\partial y}\right)^* + \frac{\partial v}{\partial x}\right) t^* \left(\frac{G^*}{G_0}\right), \qquad (2)$$

Where t is element thickness and $\left(\frac{\partial u}{\partial y}\right)^*$, t^*, G^* are parameters of a neighboring horizontal element and G_0 is a reference shear modulus value to account for the change in material properties in adjacent elements. The numerical value is taken such that the components G/G_0 ; G^*/G_0 do not have a significant effect on skewing the global stiffness matrix towards the larger stiffness components. The reference shear modulus value is calculated as:

$$G_0 = \frac{\sum_{i=1}^{n} G_i}{n} , \qquad (3)$$

where G_i denote the shear moduli used in the analysis. In an orthogonal element definition where $G_{12} \neq G_{21}$, the shear moduli used in the Eq. (2) are defined along the relevant edge. Planar shear moduli are not separated further in this article. Change in longitudinal displacement in parameter $(\partial u/\partial y)^*$ is always considered in
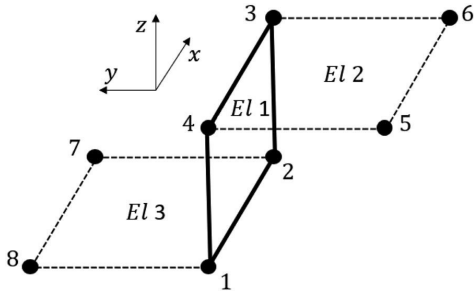
Figure 2. Pairing elements for $\partial u/\partial y$ degree of freedom definition.

the direction of the positive y-axis, i.e. in Figure 2:

$$\left(\frac{\partial u}{\partial y}\right)_4 = \frac{u_4 - u_5}{h_{el2}}, \tag{4}$$

$$\left(\frac{\partial u}{\partial y}\right)_1 = \frac{u_8 - u_1}{h_{el3}}, \tag{5}$$

Element principal dimensions are defined as length l_{el} and height h_{el} for the primary and the secondary edge

lengths. Vertical elements are positioned on the global xz-plane making the x-axis the primary edge direction and the z-axis the secondary edge direction, while the horizontal elements on the xy-plane have primary edge along the x-axis and secondary edge along the y-axis direction.

The shear flow rate equilibrium in the shared edge in Figure 3 is described as:

$$q_{el1}s_{el1,z} + q_{el2}s_{el2,z} + q_{el3}s_{el3,y} + q_{el4}s_{el4,y} = 0 \tag{6}$$

where $s_{el1,z}, \ldots, s_{el4,y}$ obtain the polar values $(1; -1)$ according to the edge normal direction respective to a collinear principal axis. The equilibrium equation can be re-written considering the edge normal scalars based on Figure 3 as:

$$q_{el2} + q_{el3} = q_{el1} + q_{el4} , \tag{7}$$

where

$$q_{el2} + q_{el3} = q_{pos}, \tag{8}$$

$$q_{el1} + q_{el4} = q_{neg}. \tag{9}$$

The equilibrium shear flow rate degree of freedom is the representation of the summation of shear flow rate
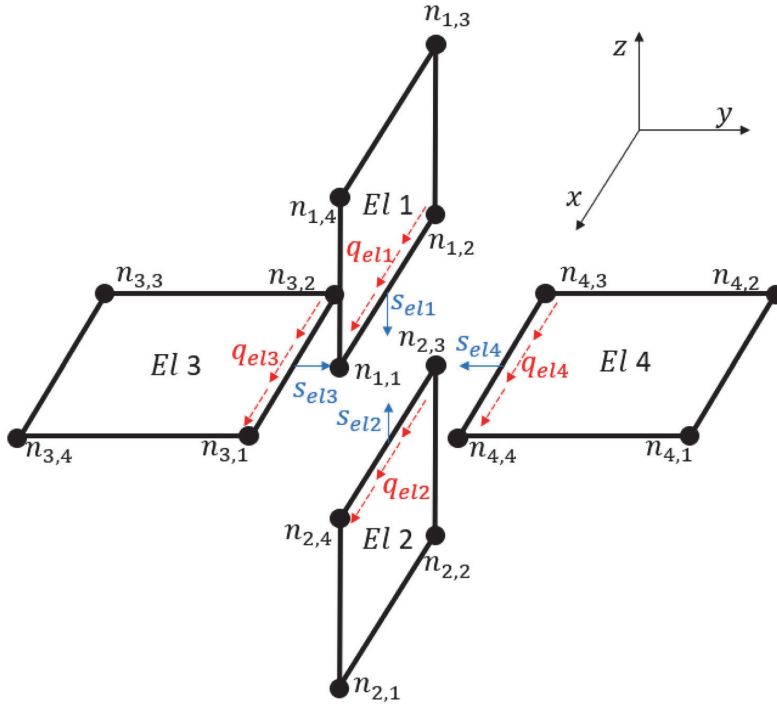

Figure 3. Shear flow equilibrium in coincident element edge (This figure is available in colour online).

components on positive or negative edges $q_{pos} = q_{neg} = q$, where the indexes pos, neg represent the direction of the edge normal.

After replacing Eqs. (4) and (5) and further opening Eq. (2), q can be defined in nodes on the positive and negative edge respectively as:

$$q_2 = q_3$$

$$= \left(\frac{\partial u}{\partial z} + \frac{\partial w}{\partial x}\right)t\left(\frac{G}{G_0}\right)$$

$$+ \left(\frac{u^* - u}{h^*} + \frac{\partial v}{\partial x}\right)t^*\left(\frac{G^*}{G_0}\right), \qquad (10)$$

$$q_1 = q_4$$

$$= \left(\frac{\partial u}{\partial z} + \frac{\partial w}{\partial x}\right)t\left(\frac{G}{G_0}\right)$$

$$+ \left(\frac{u - u^*}{h^*} + \frac{\partial v}{\partial x}\right)t^*\left(\frac{G^*}{G_0}\right), \qquad (11)$$

where indexes 1–4 denote the node in counterclockwise numeration, see Figure 5.

2.3. Definition of the horizontal element

A simplified nodal description for non-zero degrees of freedom is used for horizontal element description. The horizontal element DOF values play a key role in the solvability of Eq. (10) and (11). The non-zero degrees of freedom for the deck plating elements are shown in Figure 4.

Approximations for deck plating:

$$u(x_0, y) = A_{u_y}y + B_{u_y}, \qquad (12)$$

$$v(x_0, y) = A_{u_x}y + B_{u_x} \qquad (13)$$

$$u(x, y_0) = A_{u_x}x + B_{u_x}, \qquad (14)$$

$$v(x, y_0) = A_{v_x}x^3 + B_{v_x}x^2 + C_{v_x}x + , \qquad (15)$$

where A, B, C, D are the polynomial multipliers with the index denoting the relevant displacement field between u-longitudinal displacement and v-vertical displacement and the changing variable between x, y coordinates. Values x_0 and y_0 represent the constant variable, as independent polynomial equations are defined for each displacement field variable.

Constant values for vertical plating approximations:

$$\begin{cases} u(0, 0) = u_1 \\ u(0, h) = u_4 \end{cases}, \qquad (16)$$

$$\begin{cases} v(0, 0) = v_1 \\ v(0, h) = v_4 \end{cases}, \qquad (17)$$

$$\begin{cases} u(0, 0) = u_1 \\ u(0, l) = u_2 \end{cases}, \qquad (18)$$

$$\begin{cases} v(0, 0) = v_1 \\ \frac{\partial v}{\partial x}(0, 0) = \frac{\partial v_1}{\partial x} \\ v(0, l) = v_2 \\ \frac{\partial v}{\partial x}(0, l) = \frac{\partial v_2}{\partial x} \end{cases}. \qquad (19)$$

After inserting the values of the constants into Eq. (12) to (15), regrouping for the DOFs shown in Figure 4, the displacement fields are described as a linear
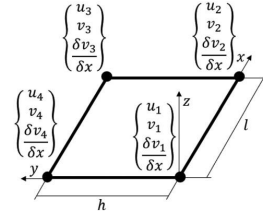

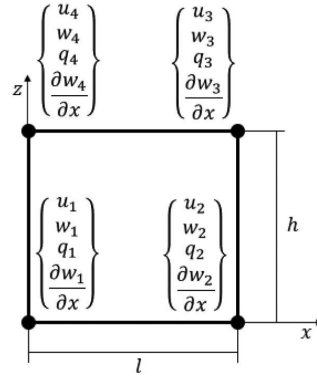**Figure 4.** Degrees of freedom for deck plating element.

Figure 5. Degrees of freedom for vertical plating elements.

combination of shape functions and DOFs:

$$u(x, y) = \varepsilon_1(y)\phi_1(x)u_1 + \varepsilon_1(y)\phi_2(x)u_2$$
$$+ \varepsilon_2(y)\phi_1(x)u_4 + \varepsilon_2(y)\phi_2(x)u_3 \qquad (20)$$

$$v(x, y) = \varepsilon_1(y)\omega_1(x)v_1 + \varepsilon_2(y)\omega_1(x)v_4$$
$$+ \varepsilon_1(y)\omega_2(x)\left(\frac{\partial v}{\partial x}\right)_1 + \varepsilon_2(y)\omega_2(x)\left(\frac{\partial v}{\partial x}\right)_4$$
$$+ \varepsilon_1(y)\omega_3(x)v_2 + \varepsilon_2(y)\omega_3(x)v_3$$
$$+ \varepsilon_1(y)\omega_4(x)\left(\frac{\partial v}{\partial x}\right)_2 + \varepsilon_2(y)\omega_4(x)\left(\frac{\partial v}{\partial x}\right)_3$$
$$(21)$$

Transversal and longitudinal shape function approximations for the axial and transversal displacement are first-order polynomials:

$$\begin{cases} \varepsilon_1(y) = 1 - \dfrac{y}{h}, \\ \varepsilon_2(y) = \dfrac{y}{h}, \end{cases} \qquad (22)$$

$$\begin{cases} \phi_1(x) = 1 - \dfrac{x}{l}, \\ \phi_2(x) = \dfrac{x}{l}. \end{cases} \qquad (23)$$

The longitudinal shape function approximations for the transverse displacement are third-order polynomials:

$$\begin{cases} \omega_1(x) = \dfrac{l^3 - 3lx^2 + 2x^3}{l^3} \\ \omega_2(x) = \dfrac{l^2 x - 2lx^2 + x^3}{l^2} \\ \omega_3(x) = \dfrac{3lx^2 - 2x^3}{h^3} \\ \omega_4(x) = \dfrac{x^3 - lx^2}{x^2}, \end{cases} \qquad (24)$$

Displacement fields can alternatively be expressed in vector form as

$$u(x, y) = \{U\}^{\mathrm{T}}\{u\}, \qquad (25)$$

$$v(x, y) = \{V\}^{\mathrm{T}}\{v\}, \qquad (26)$$

where $\{U\}$, $\{V\}$ are vectors of shape functions and $\{u\}$, $\{v\}$ are vectors of nodal degrees of freedom values.

2.4. Definition of the longitudinal vertical element

The longitudinal vertical element utilises the shear flow rate DOF description in Eq. (2) in an asymmetric approximation definition to improve the accuracy of the shear stress evaluation. The non-zero degrees of freedom for the vertical plating elements are shown in Figure 5.

The approximations for the vertical plating formulation:

$$u(x_0, z) = A_{u_z}w^3 + B_{u_z}w^2 + C_{u_z}w + D_{u_z}, \qquad (27)$$

$$w(x_0, z) = A_{w_z}w + B_{w_z} \qquad (28)$$

$$u(x, z_0) = A_{u_x}x + B_{u_x}, \qquad (29)$$

$$w(x, z_0) = A_{w_x}x^3 + B_{w_x}x^2 + C_{w_x}x + D_{w_x}. \qquad (30)$$

Similar logic is applied to the definitions of polynomial constants A, B, C, D as it was explained for Eqs. (12) to (15).

The constant values for the vertical plating approximations, where deformation $\partial u/\partial z$ is derived from Eq. (10) and (11) as:

$$\begin{cases} u(0, 0) = u_1 \\ \dfrac{\partial u}{\partial z}(0, 0) = \left(\dfrac{\partial u}{\partial z}\right)_1 = \dfrac{q_1 G_0}{tG} - \left(\dfrac{\partial w}{\partial x}\right)_1 \\ - \left(\dfrac{u_1^* - u_1}{h^*} + \left(\dfrac{\partial v}{\partial x}\right)_1\right)\dfrac{t^* G^*}{tG} \\ u(0, h) = u_4 \\ \dfrac{\partial u}{\partial z}(0, h) = \left(\dfrac{\partial u}{\partial z}\right)_4 = \dfrac{q_4 G_0}{tG} \\ - \left(\dfrac{\partial w}{\partial x}\right)_4 - \left(\dfrac{u_4 - u_4^*}{h^*} + \left(\dfrac{\partial v}{\partial x}\right)_4\right)\dfrac{t^* G^*}{tG}, \end{cases} \qquad (31)$$

$$\begin{cases} w(0, 0) = w_1 \\ w(0, h) = w_4, \end{cases} \qquad (32)$$

$$\begin{cases} u(0, 0) = u_1 \\ u(0, l) = u_2, \end{cases} \qquad (33)$$

$$\begin{cases} w(0, 0) = w_1 \\ \dfrac{\partial w}{\partial x}(0, 0) = \dfrac{\partial w_1}{\partial x} \\ w(0, l) = w_2 \\ \dfrac{\partial w}{\partial x}(0, l) = \dfrac{\partial w_2}{\partial x}, \end{cases} \qquad (34)$$

After inserting the values of the constants into Eq. (27) to (30), regrouping for DOFs, as shown in Figure 5, the displacement fields are described as a linear

combination of shape functions and DOFs:

$$u(x, z) = \psi_1(z)\phi_1(x)u_1 + \psi_2(z)\phi_1(x)$$
$$\left(\frac{q_1 G_0}{tG} - \left(\frac{\partial w}{\partial x}\right)_1 - \left(\frac{u_1^* - u_1}{h^*} + \left(\frac{\partial v}{\partial x}\right)_1\right)\frac{t^* G^*}{tG}\right)$$
$$+ \psi_1(z)\phi_2(x)u_2 + \psi_2(z)\phi_2(x)$$
$$\left(\frac{q_2 G_0}{tG} - \left(\frac{\partial w}{\partial x}\right)_2 - \left(\frac{u_2^* - u_2}{h^*} + \left(\frac{\partial v}{\partial x}\right)_2\right)\frac{t^* G^*}{tG}\right)$$
$$+ \psi_3(z)\phi_2(x)u_3 + \psi_4(z)\phi_2(x)$$
$$\left(\frac{q_3 G_0}{tG} - \left(\frac{\partial w}{\partial x}\right)_3 - \left(\frac{u_3 - u_3^*}{h^*} + \left(\frac{\partial v}{\partial x}\right)_3\right)\frac{t^* G^*}{tG}\right)$$
$$+ \psi_3(z)\phi_1(x)u_4 + \psi_4(z)$$
$$\phi_1(x)\left(\frac{q_4 G_0}{tG} - \left(\frac{\partial w}{\partial x}\right)_4 - \left(\frac{u_4 - u_4^*}{h^*} + \left(\frac{\partial v}{\partial x}\right)_4\right)\frac{t^* G^*}{tG}\right),$$

$$(35)$$

$$w(x, z) = \xi_1(z)\omega_1(x)w_1 + \xi_2(z)\omega_1(x)w_4$$
$$+ \xi_1(z)\omega_2(x)\left(\frac{\partial w}{\partial x}\right)_1 + \xi_2(z)\omega_2(x)\left(\frac{\partial w}{\partial x}\right)_4$$
$$+ \xi_1(z)\omega_3(x)w_2 + \xi_2(z)\omega_3(x)w_3$$
$$+ \xi_1(z)\omega_4(x)\left(\frac{\partial w}{\partial x}\right)_2 + \xi_2(z)\omega_4(x)\left(\frac{\partial w}{\partial x}\right)_3,$$

$$(36)$$

where

$$\begin{cases} \psi_1(z) = \dfrac{h^3 - 3hz^2 + 2z^3}{h^3} \\ \psi_2(z) = \dfrac{h^2 z - 2hz^2 + z^3}{h^2} \\ \psi_3(z) = \dfrac{3hz^2 - 2z^3}{h^3} \\ \psi_4(z) = \dfrac{z^3 - hz^2}{h^2} \end{cases}$$

$$(37)$$

$$\begin{cases} \xi_1(z) = 1 - \dfrac{z}{h} \\ \xi_2(z) = \dfrac{z}{h} \end{cases}$$

$$(38)$$

The shape functions ω_i and ϕ_j are identical to those used for the horizontal element definitions. The displacement fields can alternatively be presented in vector form as:

$$u(x, z) = \{U\}^{\mathrm{T}}\{u\},$$

$$(39)$$

$$w(x, z) = \{W\}^{\mathrm{T}}\{w\},$$

$$(40)$$

where $\{U\}$ and $\{W\}$ are vectors of the shape functions and $\{u\}$ and $\{w\}$ are vectors of the nodal degrees of freedom.

2.5. Finite element formulation

Finite element formulation has been exemplified for a planar element on the x – and z-axes, which follows the definition of the vertical plating element. A similar finite element formulation has been used for horizontal plating elements, where the elements are defined on the xy-plane. Unique $\{\Psi\}$ matrices are defined in Eq. (63) and (70) to describe the relevant degrees of freedom with the shape functions presented in Eqs. (20), (21), (35). and (36). Non-zero degrees of freedom were included in $\{\Psi\}$ matrices to simplify the creation of the global stiffness matrix by using a homogeneous nodal definition.

An orthotropic approach has been used to define the finite element formulation, as in real-life applications, where the elements would represent stiffened panels that make up the structure of ships. Thus, depending on the stiffening elements of the stiffened panel, the material properties must be orthogonal while satisfying the following conditions:

$$\begin{Bmatrix} \varepsilon_{xx} \\ \varepsilon_{zz} \\ 2\varepsilon_{xz} \end{Bmatrix} = \begin{Bmatrix} \dfrac{\partial u(x, z)}{\partial x} \\ \dfrac{\partial w(x, z)}{\partial z} \\ \dfrac{\partial u(x, z)}{\partial z} + \dfrac{\partial w(x, z)}{\partial x} \end{Bmatrix}$$
$$= \begin{Bmatrix} \left\{\dfrac{\partial U}{\partial x}\right\}^{\mathrm{T}}\{u\} \\ \left\{\dfrac{\partial W}{\partial z}\right\}^{\mathrm{T}}\{w\} \\ \left\{\dfrac{\partial U}{\partial z}\right\}^{\mathrm{T}}\{u\} + \left\{\dfrac{\partial W}{\partial x}\right\}^{\mathrm{T}}\{w\} \end{Bmatrix},$$

$$(41)$$

$$\begin{Bmatrix} \sigma_{xx} \\ \sigma_{zz} \\ \sigma_{xz} \end{Bmatrix} = \begin{bmatrix} C_{11} & C_{12} & 0 \\ C_{12} & C_{22} & 0 \\ 0 & 0 & C_{66} \end{bmatrix} \begin{Bmatrix} \varepsilon_{xx} \\ \varepsilon_{zz} \\ 2\varepsilon_{xz} \end{Bmatrix},$$

$$(42)$$

where C_{ij} are the elastic stiffnesses:

$$C_{11} = \frac{E_1}{(1 - \nu_{12}\nu_{21})},$$

$$(43)$$

$$C_{22} = \frac{E_2}{(1 - \nu_{12}\nu_{21})},$$

$$(44)$$

$$C_{12} = \nu_{12}C_{22},$$

$$(45)$$

$$C_{66} = G_{12} = G_{21}.$$

$$(46)$$

Here, E_1 and E_2 are the Young's moduli, G_{12} and G_{21} are the in-plane shear moduli and ν_{21} and ν_{12} are the orthogonal planar Poisson ratios are defined as:

$$\nu_{21} = \nu_{12}\frac{E_2}{E_1}.$$

$$(47)$$

The finite element formulation starts from defining simplified differential equations for stress equilibrium in in-plane directions for planar elements with unit thickness and planar unit dimensions dx, dz, shown in Figure 6.

Force equilibrium for planar axis:

$$\sum F_x = -\sigma_{xx}(dz*1) - \sigma_{zx}(dx*1)$$
$$+ \left[\sigma_{xx} + \frac{\partial \sigma_{xx}}{\partial x}dx\right](dz*1)$$
$$+ \left[\sigma_{zx} + \frac{\partial \sigma_{zx}}{\partial z}dz\right](dx*1) + f_x$$
$$= \frac{\partial \sigma_{xx}}{\partial x}dxdz + \frac{\partial \sigma_{zx}}{\partial z}dxdz + f_x = 0 \quad (48)$$

$$\sum F_z = -\sigma_{zz}(dx*1) - \sigma_{xz}(dz*1)$$
$$+ \left[\sigma_{zz} + \frac{\partial \sigma_{zz}}{\partial z}dz\right](dx*1)$$
$$+ \left[\sigma_{xz} + \frac{\partial \sigma_{xz}}{\partial x}dx\right](dz*1) + f_z$$
$$= \frac{\partial \sigma_{zz}}{\partial z}dxdz + \frac{\partial \sigma_{xz}}{\partial x}dxdz + f_z = 0. \quad (49)$$

In this formulation, it is ultimately assumed that the planar shear stress is constant, however, the formulation can be optimised to include such orthogonal materials. By assuming that the area $dxdz$ is one unit, the differential equations can be simplified:

$$\frac{\partial}{\partial x}\sigma_{xx} + \frac{\partial}{\partial z}\sigma_{zx} + f_x = \frac{\partial}{\partial x}\sigma_{xx} + \frac{\partial}{\partial z}\sigma_{xz} + f_x = 0, \quad (50)$$

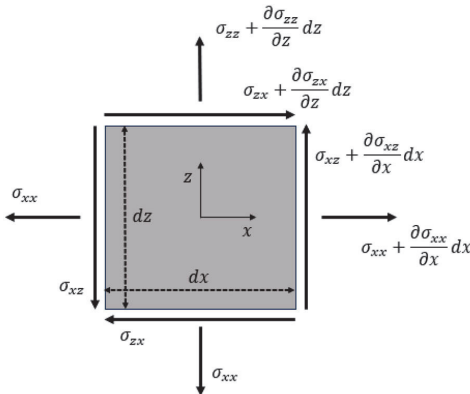$$\frac{\partial}{\partial z}\sigma_{zz} + \frac{\partial}{\partial x}\sigma_{xz} + f_z = 0. \quad (51)$$

Figure 6. Equilibrium of planar unit element.

Strong form differential equations are multiplied with weight functions and integrated over the volume which is then simplified to a surface integral as the plating is considered as thin-walled structures:

$$\int_V \left(s_1\left(\frac{\partial}{\partial x}\sigma_{xx} + \frac{\partial}{\partial z}\sigma_{xz} + f_x\right)\right)dV$$
$$= \int_\Omega t\left(s_1\left(\frac{\partial}{\partial x}\sigma_{xx} + \frac{\partial}{\partial z}\sigma_{xz} + f_x\right)\right)dxdz = 0. \quad (52)$$

$$\int_V \left(s_2\left(\frac{\partial}{\partial z}\sigma_{zz} + \frac{\partial}{\partial x}\sigma_{xz} + f_z\right)\right)dV$$
$$= \int_\Omega t\left(s_2\left(\frac{\partial}{\partial z}\sigma_{zz} + \frac{\partial}{\partial x}\sigma_{xz} + f_z\right)\right)dxdz = 0. \quad (53)$$

Weak form equations are created by using Gauss theorem for partial integration of surface integral that states:

$$\int_\Omega w\frac{\partial G(x, y)}{\partial x}dxdy = \oint_\Gamma n_x[wG(x, y)]ds$$
$$- \int_\Omega \frac{\partial w}{\partial x}G(x, y)dxdy. \quad (54)$$

Weak formulation is expressed using Eqs. (52) to (54) as:

$$\int_\Omega t\frac{\partial s_1}{\partial x}\sigma_{xx}dxdy + \int_\Omega t\frac{\partial s_1}{\partial z}\sigma_{xz}dxdy$$
$$- \oint_\Gamma ts_1(n_x\sigma_{xx} + n_z\sigma_{xz})ds - \int_\Omega ts_1 f_x dxdy$$
$$= 0 \quad (55)$$

$$\int_\Omega t\frac{\partial s_2}{\partial x}\sigma_{xz}dxdy + \int_\Omega t\frac{\partial s_2}{\partial z}\sigma_{zz}dxdy$$
$$- \oint_\Gamma ts_2(n_x\sigma_{xz} + n_z\sigma_{zz})ds - \int_\Omega ts_2 f_z dxdy$$
$$= 0 \quad (56)$$

Weak-form equations are further simplified to omit the boundary integral components as external forces are directly applied as nodal forces. Therefore, the final

weak form equations are:

$$\int_\Omega t \frac{\partial s_1}{\partial x} \sigma_{xx} dxdy + \int_\Omega t \frac{\partial s_1}{\partial z} \sigma_{xz} dxdy - \int_\Omega t s_1 f_x dxdy$$
$$= 0 \qquad (57)$$

$$\int_\Omega t \frac{\partial s_2}{\partial x} \sigma_{xz} dxdy + \int_\Omega t \frac{\partial s_2}{\partial z} \sigma_{zz} dxdy - \int_\Omega t s_2 f_z dxdy$$
$$= 0 \qquad (58)$$

The weak formulation is transferred into vector form:

$$\int_\Omega t \left\{ \begin{array}{c} \frac{\partial s_1}{\partial x} \\ \frac{\partial s_2}{\partial z} \\ \frac{\partial s_1}{\partial z} + \frac{\partial s_2}{\partial x} \end{array} \right\}^T \left\{ \begin{array}{c} \sigma_{xx} \\ \sigma_{zz} \\ \sigma_{xz} \end{array} \right\} dxdz$$

$$- \int_\Omega t \left\{ \begin{array}{c} s_1 \\ s_2 \end{array} \right\}^T \left\{ \begin{array}{c} f_x \\ f_z \end{array} \right\} dxdz$$

$$= 0. \qquad (59)$$

The components in the above equation can be alternatively written as:

$$\left\{ \begin{array}{c} \frac{\partial s_1}{\partial x} \\ \frac{\partial s_2}{\partial z} \\ \frac{\partial s_1}{\partial z} + \frac{\partial s_2}{\partial x} \end{array} \right\}^T = \begin{bmatrix} s_1 & s_2 \end{bmatrix} \begin{bmatrix} \frac{\partial}{\partial x} & 0 & \frac{\partial}{\partial z} \\ 0 & \frac{\partial}{\partial z} & \frac{\partial}{\partial x} \end{bmatrix}$$

$$= \left\{ \begin{array}{c} s_1 \\ s_2 \end{array} \right\}^T [D_1]^T, \qquad (60)$$

$$\left\{ \begin{array}{c} \sigma_{xx} \\ \sigma_{zz} \\ \sigma_{xz} \end{array} \right\} = \left\{ \begin{array}{c} C_{11} \frac{\partial u}{\partial x} + C_{12} \frac{\partial w}{\partial z} \\ C_{12} \frac{\partial u}{\partial x} + C_{22} \frac{\partial w}{\partial z} \\ C_{66} \left(\frac{\partial u}{\partial z} + \frac{\partial w}{\partial x} \right) \end{array} \right\}$$

$$= \begin{bmatrix} C_{11} & C_{12} & 0 \\ C_{12} & C_{22} & 0 \\ 0 & 0 & C_{66} \end{bmatrix} \begin{bmatrix} \frac{\partial}{\partial x} & 0 \\ 0 & \frac{\partial}{\partial z} \\ \frac{\partial}{\partial z} & \frac{\partial}{\partial x} \end{bmatrix}$$

$$\times \left\{ \begin{array}{c} u \\ w \end{array} \right\}$$

$$= [C][D_1] \left\{ \begin{array}{c} u \\ w \end{array} \right\}, \qquad (61)$$

$$\int_\Omega t \left\{ \begin{array}{c} s_1 \\ s_2 \end{array} \right\}^T [D_1]^T [C][D_1] \left\{ \begin{array}{c} u \\ w \end{array} \right\} dxdz$$

$$- \int_\Omega t \left\{ \begin{array}{c} s_1 \\ s_2 \end{array} \right\}^T \left\{ \begin{array}{c} f_x \\ f_z \end{array} \right\} dxdz$$

$$= 0, \qquad (62)$$

where vectors $\{u\}$, $\{w\}$, $\{s_1\}$ and $\{s_2\}$ for vertical plating elements are defined as the linear combination of the shape function vectors and the nodal degree of freedom value vectors:

$$\left\{ \begin{array}{c} u \\ w \end{array} \right\} = \begin{bmatrix} \psi_1\phi_1 + \psi_2\phi_1 D & 0 & 0 & \psi_2\phi_1 S & -\psi_2\phi_1 F & -\psi_2\phi_1 & \psi_1\phi_2 + \psi_2\phi_2 D & 0 & 0 & \psi_2\phi_2 S & -\psi_2\phi_2 F & -\psi_2\phi_2 \\ 0 & 0 & \omega_1\xi_1 & 0 & 0 & \omega_2\xi_1 & 0 & 0 & \omega_3\xi_1 & 0 & 0 & \omega_4\xi_1 \\ \psi_3\phi_2 - \psi_4\phi_2 D2 & 0 & 0 & \psi_4\phi_2 S & -\psi_4\phi_2 F2 & -\psi_4\phi_2 & \psi_3\phi_2 - \psi_4\phi_1 D2 & 0 & 0 & \psi_4\phi_1 S & -\psi_4\phi_1 F2 & -\psi_4\phi_1 \\ 0 & 0 & \omega_3\xi_2 & 0 & 0 & \omega_4\xi_2 & 0 & 0 & \omega_1\xi_2 & 0 & 0 & \omega_2\xi_2 \end{bmatrix} \cdots$$

$$(63)$$

$$\cdots \begin{bmatrix} -\psi_2\phi_1 D & -\psi_2\phi_2 D & \psi_4\phi_2 D2 & \psi_4\phi_1 D2 \\ 0 & 0 & 0 & 0 \end{bmatrix} * \begin{bmatrix} u_1 & v_1 & w_1 & q_1 & \frac{\partial v_1}{\partial x} & \frac{\partial w_1}{\partial x} & u_2 & \cdots & \frac{\partial w_4}{\partial x} & u_1^* & u_2^* & u_3^* & u_4^* \end{bmatrix}^T = [\Psi_1]\{\Delta_1\}$$

$$\left\{ \begin{array}{c} s_1 \\ s_2 \end{array} \right\} = [\Psi_1] * \begin{bmatrix} a_1 & a_2 & \cdots & a_{27} & a_{28} \end{bmatrix}^T = [\Psi_1]\{a\}$$

$$(64)$$

where

$$S = \frac{G_0}{tG_1}, \qquad (65)$$

$$D = \frac{t_m G_{1,m}}{h_m tG_1}, \qquad (66)$$

$$F = \frac{t_m G_{1,m}}{tG_1}, \qquad (67)$$

$$D2 = \frac{t_o G_{1,o}}{h_o tG_1}, \qquad (68)$$

$$F2 = \frac{t_o G_{1,o}}{tG_1}. \qquad (69)$$

Indexes m, o represent parameters of positive edge and negative edge pairing elements m, o respectively. If a pairing element does not exist, $D = F = D2 = F2 = 0$.

Similarly to Eq. (63) and (64), vectors $\{u\}$, $\{v\}$, $\{s_1\}$ and $\{s_2\}$ for the horizontal plating elements are defined as the linear combination of the shape function vectors and the nodal degree of freedom value vectors:

$$\left\{ \begin{matrix} u \\ v \end{matrix} \right\} = \begin{bmatrix} \varepsilon_1 \phi_1 & 0 & 0 & 0 & 0 & 0 & \varepsilon_1 \phi_2 & 0 & 0 & 0 & 0 & 0 \\ 0 & \varepsilon_1 \omega_1 & 0 & 0 & \varepsilon_1 \omega_2 & 0 & 0 & \varepsilon_1 \omega_3 & 0 & 0 & \varepsilon_1 \omega_4 & 0 \end{bmatrix}$$

$$\dots \begin{matrix} \varepsilon_2 \phi_2 & 0 & 0 & 0 & 0 & 0 & \varepsilon_2 \phi_1 & 0 & 0 & 0 & 0 & 0 \\ 0 & \varepsilon_2 \omega_3 & 0 & 0 & \varepsilon_2 \omega_4 & 0 & 0 & \varepsilon_2 \omega_1 & 0 & 0 & \varepsilon_2 \omega_2 & 0 \end{matrix} \Big] *$$

$$\dots \begin{bmatrix} u_1 & v_1 & w_1 & q_1 & \dfrac{\partial v_1}{\partial x} & \dfrac{\partial w_1}{\partial x} & u_2 & v_2 & w_2 & \dots & q_4 & \dfrac{\partial v_4}{\partial x} & \dfrac{\partial w_4}{\partial x} \end{bmatrix}^T = [\Psi_2]\{\Delta_2\}$$

$$(70)$$

$$\left\{ \begin{matrix} s_1 \\ s_2 \end{matrix} \right\} = [\Psi_2] \begin{bmatrix} a_1 & a_2 & \dots & a_{23} & a_{24} \end{bmatrix}^T$$

$$= [\Psi_2]\{a\} \qquad (71)$$

By grouping the vectors of weight constants $\{a\}$ the finite element equation for the vertical plating element becomes:

$$\{a\}^T \left(\int_\Omega t[\Psi_1]^T [D_1]^T [C][D_1][\Psi_1] dxdz \{\Delta_1\} - \int_\Omega t[\Psi_1]^T \left\{ \begin{matrix} f_x \\ f_y \end{matrix} \right\} dxdz \right) = 0$$

$$(72)$$

As the vector of weight constants cannot equal zero, the components in the brackets must do so. The matrix multiplication can be expressed as $[D_1][\Psi_1] = [B_1]$,

where

$$\int_\Omega t[B_1]^T [C][B_1] dxdz \{\Delta_1\} - \int_\Omega t[\Psi_1]^T \left\{ \begin{matrix} f_x \\ f_z \end{matrix} \right\} dxdz$$

$$= 0, \qquad (73)$$

$$\int_\Omega t[B_1]^T [C][B_1] dxdz = [K_1], \qquad (74)$$

$$\int_\Omega t[\Psi_1]^T \left\{ \begin{matrix} f_x \\ f_z \end{matrix} \right\} dxdz = \{F_1\}. \qquad (75)$$

For horizontal plating elements Eqs. (73) to (75) would be alternatively presented as:

$$\int_\Omega t[B_2]^T [C][B_2] dxdy \{\Delta_2\} - \int_\Omega t[\Psi_2]^T \left\{ \begin{matrix} f_x \\ f_y \end{matrix} \right\} dxdy$$

$$= 0, \qquad (76)$$

$$\int_\Omega t[B_2]^T [C][B_2] dxdy = [K_2], \qquad (77)$$

$$\int_\Omega t[\Psi_2]^T \left\{ \begin{matrix} f_x \\ f_y \end{matrix} \right\} dxdy = \{F_2\}, \qquad (78)$$

where

$$[D_2] = \begin{bmatrix} \dfrac{\partial}{\partial x} & 0 \\ 0 & \dfrac{\partial}{\partial y} \\ \dfrac{\partial}{\partial y} & \dfrac{\partial}{\partial x} \end{bmatrix}. \qquad (80)$$

3. Analysis models

3.1. Simple beam model

The initial validation of the HSD formulation is performed on a simple hollow beam model with a total length of 10 m, total height of 4 m, and total depth of 1 m. Two configurations are created to independently analyse the accuracy of the proposed methodology with changing thicknesses and material properties in planar directions. In the first configuration in Figure 7, Young's modulus is defined throughout the sections as $E_1 = E_2 = E = 200$ GPa and Poisson's ratio as $v = 0.3$, whereas the thickness changes in the range from 5 mm to 20 mm with a 1:2 thickness ratio between every adjacent quadrant. The second configuration in Figure 8, has uniformly defined thickness as $t = 10$ mm, however, the Young's moduli varies in the range from 50 GPa to 200 GPa in a similar 2:1 ratio between quadrants.

E=200 Gpa; $v=0.3$; t=10 mm

E=200 Gpa; $v=0.3$; t=5 mm

E=200 Gpa; $v=0.3$; t=20 mm

E=200 Gpa; $v=0.3$; t=10 mm
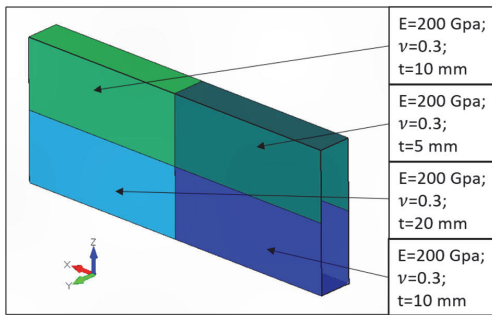
Figure 7. Beam model parameters with constant Young's moduli (This figure is available in colour online).

E=200 Gpa; $v=0.3$; t=10 mm

E=100 Gpa; $v=0.3$; t=10 mm

E=100 Gpa; $v=0.3$; t=10 mm
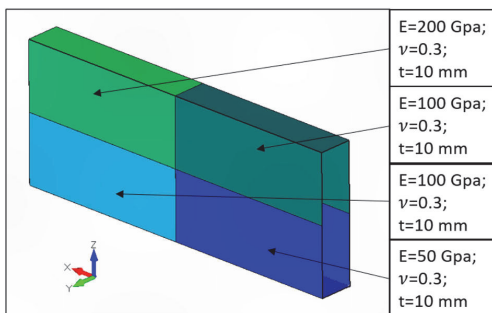
E=50 Gpa; $v=0.3$; t=10 mm

Figure 8. Beam model parameters with constant plate thickness (This figure is available in colour online).

Three mesh sizes are applied to the models to analyse the accuracy of the HSD element against the traditional quadrilateral 4-node first-order element. The finest mesh configuration is modeled with 2500 200×200 mm elements, see Figure 9(c). This mesh is considered to be significantly denser than what is reasonable for concept design analysis and thus is used as the reference fine mesh against which coarser mesh sizes are compared. A semi-coarse mesh with an element size of 500×500 mm, see Figure 9(b) and a fully coarse mesh with an element size of 1000×1000 mm are used with the HSD formulation and the first-order 4-node elements.

The models apply simply supported beam constraints in both ends and distributed load $p = -1000$ N/mm along the longitudinal edges in the bottom of the beams.

3.2. Stepped box model

The accuracy of the HSD element formulations presented in this article is analysed on a box structure that is dimensioned to the size of a small multideck ship. The box structure consists of four vertical sections representing the vertical shell structures, longitudinal bulkheads, and superstructure shell, and six horizontal sections representing the double bottom and deck plating and upper deck plating. The plate thicknesses for the bottom and upper deck plating are increased in comparison to general deck plating. The global dimensions of the box structure are the length $L_{tot} = 60$ m, breadth $B_{tot} = 9$ m, and height $H_{tot} = 12, 4$ m.

shows the geometry models, cross-sectional dimensions, and deck numeration (Figure 10).

In addition to examining hull girder global response, the HSD formulation aims to increase accuracy in predicting stress values in two critical areas. First of such is the transition between different structural sections throughout the hull girder, see Figure 11. These transitions are best noticed in two distinct areas. Firstly, in the transition from main hull wall structures to passenger deck wall structures introducing large windows for better customer experience and thinner plating due to the proximity of the global neutral bending plane and lowered normal stress loads. Secondly, in the transition from passenger decks to cabin decks, where cabins are modularly inserted further diminishing load carrying capabilities of outer wall structures in these areas. In the concept design phase, these different structural regions can be alternatively presented as equivalent plating, where plate thickness is usually derived from the original plate thickness as this greatly dictates the shear flow equilibrium in the transition surfaces and the local peak shear stress values. Equivalent Young's
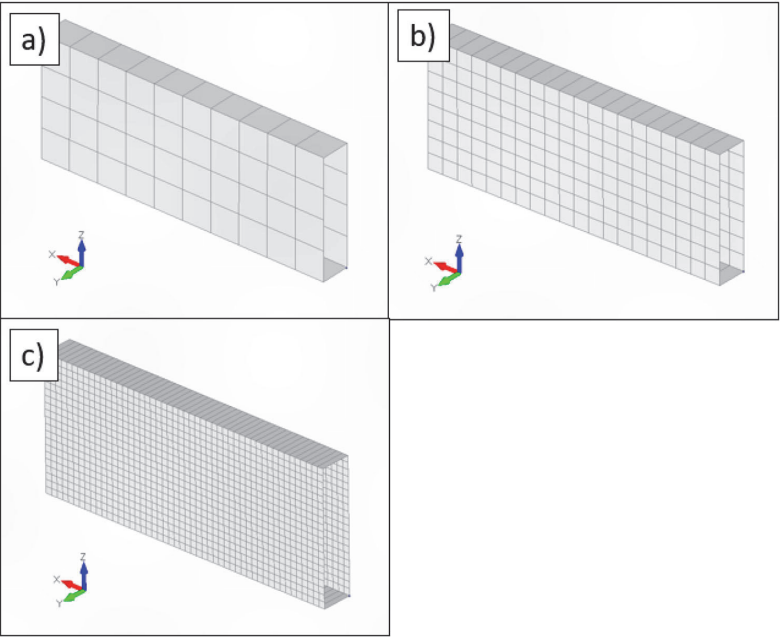
Figure 9. Beam models mesh sizing: (a) coarse mesh – 1000 × 1000 mm, (b) semi-coarse mesh – 500 × 500 mm, (c) fine mesh – 200 × 200 mm (This figure is available in colour online).
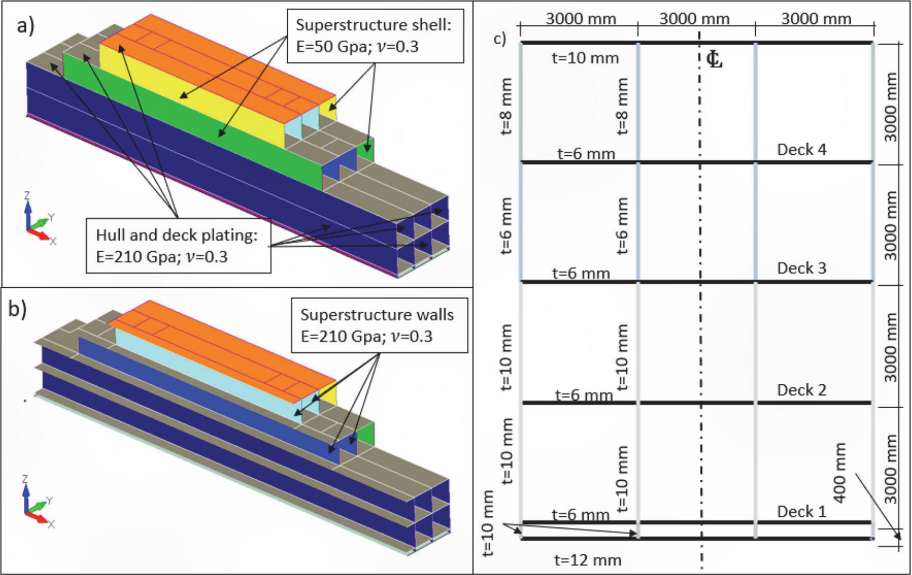

Figure 10. 3D model geometric and material parameters (a) outer walls, (b) superstructure walls, and (c) cross-section (This figure is available in colour online).
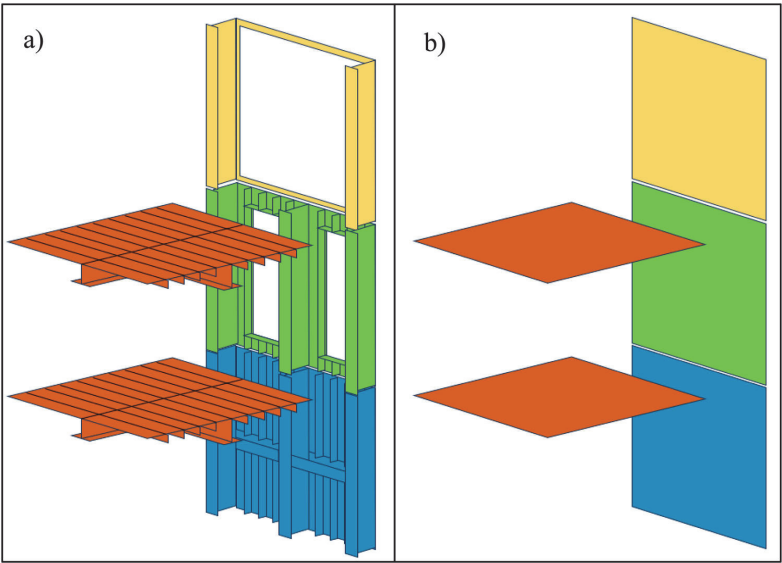
Figure 11. Simplified representation of (a) ship structures with openings and stiffeners as (b) equivalent plating elements (This figure is available in colour online).
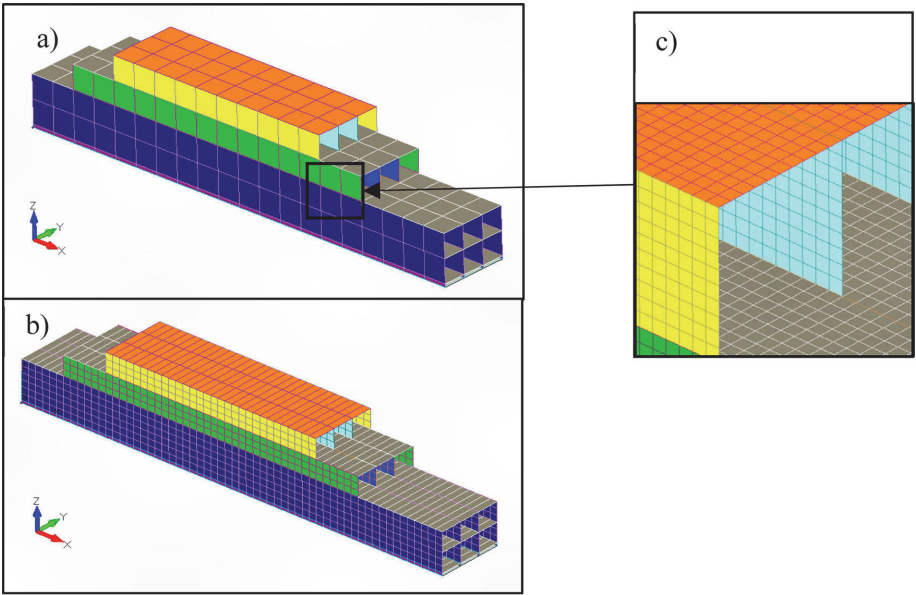
Figure 12. Finite element 3D models of stepped box model: (a) coarse mesh model, (b) semi-coarse mesh model, and (c) fine mesh model (This figure is available in colour online).

moduli are derived from stiffened panel calculations considering the size of openings and the dimensions and orientation of stiffening elements. Typical methods for doing so are the smeared stiffness-based method, where the added stiffness from stiffening structures or the decreased stiffness due to openings is divided

equally over the equivalent plating. Another option would be to use an equivalent single-layer method, that describes the equivalent plating as a ply where every layer has equivalent stiffness and thickness dependent on the geometry and configuration of the stiffening structures.

The second of such areas is the stepped superstructure decks. As passenger ships typically have balcony areas or other open spaces in passenger and cabin deck ends, the load-carrying structures naturally have a stepped configuration creating shear stress concentrations that need a more local approach to stress evaluation. Even though larger passenger ships have naturally fuller side profiles mitigating the issue, this phenomenon is additionally present in longitudinal bulkhead openings in open areas such as concert halls, open atriums, conference halls, and open restaurants.

The coarse mesh model uses uniform element dimensions in vertical structures, as well as horizontal plating with an aspect ratio of 1:1 (3000×3000 mm),

which follows the common best practices in coarse mesh modelling of ship structures, where deck spacing in vertical structures is described with a single element. The vertical shell elements between the bottom plate and the first deck plate have a limited height dimension of 400 mm. The total model consists of 524 nodes and 728 elements, see Figure 12(a). The semi-coarse mesh model places three elements between the decks in vertical structures and uses elements with 1/3 edge length of those used in the coarse mesh model. Conversely, deck elements were not divided. The semi-coarse mesh models had 3084 nodes and 3720 elements, see Figure 12(b). The results from coarse and semi-coarse mesh models are compared against a fine mesh linear element model, where the element dimension is 300×300 mm, placing 10 elements between decks resulting in 56854 nodes and 58400 elements, see Figure 12(c).

In concept design, computational cost comprises of several factors. The easiest to measure component is the actual solver time to calculate the finite element
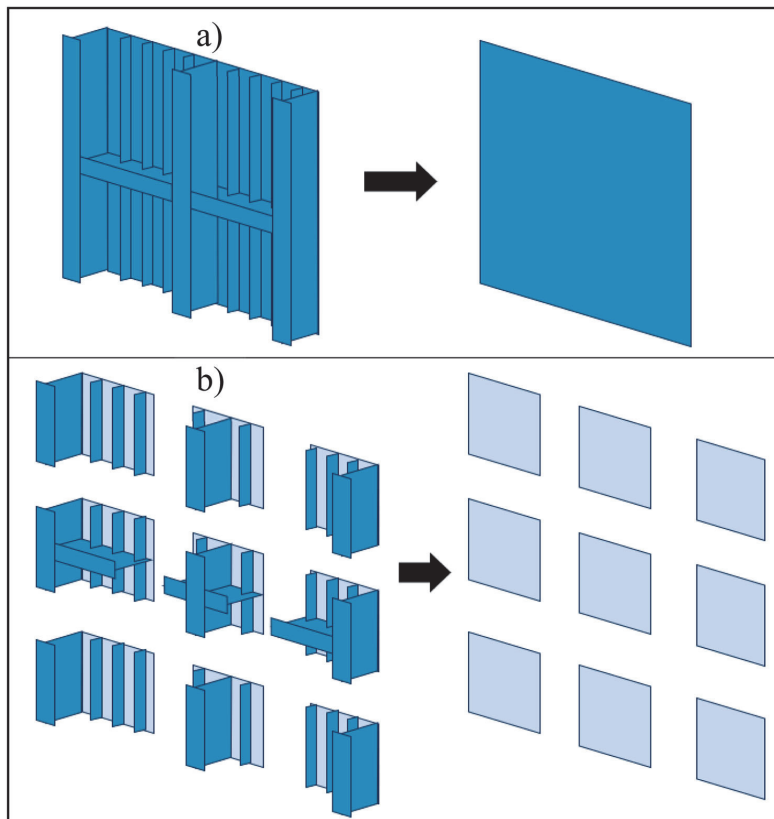

Figure 13. Equivalent plate element creation for (a) coarse mesh, (b) semi-coarse mesh (This figure is available in colour online).

equations. For this, a good overall indicator is the number of DOFs present in the model that dictates the size of the global stiffness matrix which does not directly convert over to solver time difference but does give a good insight into the solving complexity. Even more importantly, the time needed to create the model must be considered under computational cost. The concept design phase analyses aim to keep elements as big as possible to limit the number of unique equivalent element definitions used in the model. An example in Figure 13 illustrates how the coarse mesh model needs a singular element definition in shell and bulkhead structures, whereas in the semi-coarse model, where the element size is 1/3 of the coarse element size, the number of unique element definitions needed increases significantly. When expanded to include the whole global model, this added preparation time far exceeds the difference in actual solver time.

The calculation of specific equivalent element stiffness properties is outside of the scope of the models created and the analysis presented in this article. The equivalent stiffness properties presented for the stepped box model in Figure 10 are defined to extenuate the non-linear stress behaviour within the structures. The same principle is used for the fine mesh model, as the analysis aims to evaluate the gained accuracy over the similarly sized linear mesh and not replace the need for detailed 3D FEM analysis in later design stages. Therefore, modelling the stiffening elements is omitted as that level of detail is deemed not necessary for the comparison of different coarse mesh formulations.

Vertical distributed sinusoidal loading per unit length has been applied to the bottom edges of all vertical shell sections according to the equation:

$$p(x) = p_0 * \cos\left(\frac{2\pi x}{L}\right), \qquad (81)$$

with amplitude $p_0 = 200$ N/mm and total length of $L_{tot} = 60$ m. The material properties are taken as typical for full-stiffness orthotropic steel definition: $E_1 = E_2 = 210$ GPa, $\nu_1 = \nu_2 = 0, 3$. For the superstructure shell, Young's modulus has been lowered to account for the weakened structures. For superstructure shell $E_1 = E_2 = 50$ GPa, $\nu_1 = \nu_2 = 0, 3$ are used. The box model is simulated on an elastic foundation applied to the bottom nodes of the vertical shell sections.

4. Results

The global deflection, longitudinal, and vertical stress distributions have been analysed for the simply supported beam and a stepped box structure. The accuracy of the obtained numerical results using the proposed HSD element formulation has been compared with the coarse, semi-coarse, and fine mesh linear FEM numerical results in all models.

Numerical results have been collected from static analysis on the FEMAP 2021.2 software using the Simcenter Nastran solver. FEMAP's Direct Matrix Input G-set (DMIG) capabilities are deployed to import the global stiffness matrix using the shear element definitions.

4.1. Numerical results for the simply supported beam models

Comparative analysis for simply supported beam models includes global deflection, vertical shear stress, and normal stress distribution at 3/4 length of the beam and longitudinal shear stress and normal stress distribution at 3/4 height of the beam. The deflection analysis in Figure 14 shows high correspondence between all mesh sizes and element types. Differences between peak deflections for thickness varying beam model stay below 2% of the reference 200×200 mm
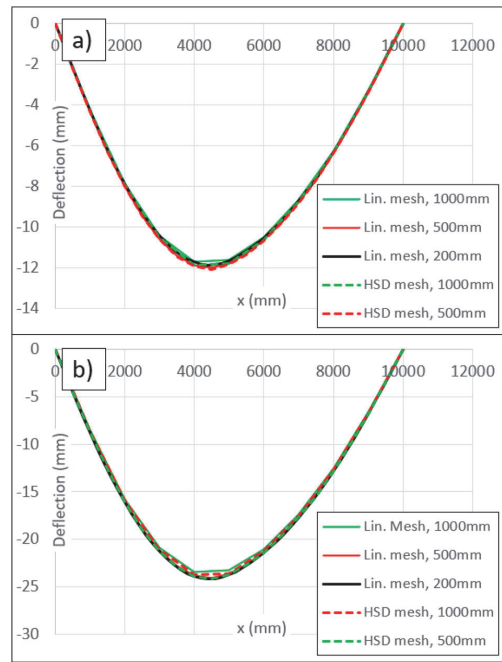

Figure 14. Deflection comparison in simply supported beam models with (a) changing thickness, and (b) changing material properties (This figure is available in colour online).
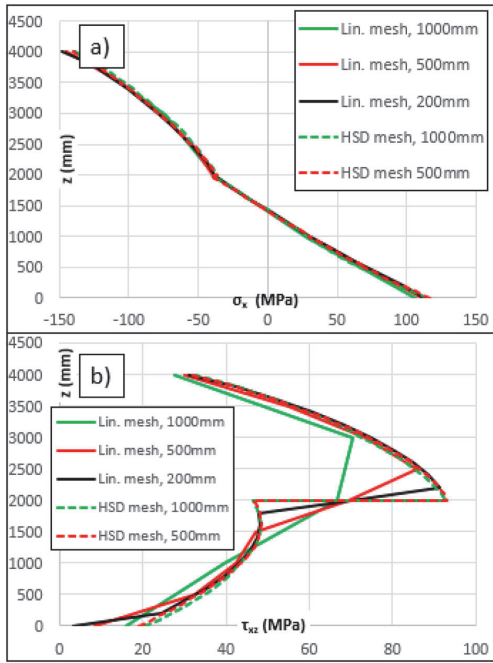
Figure 15. Vertical distributions for (a) normal stress and (b) shear stress in beam model with varying plate thickness (This figure is available in colour online).
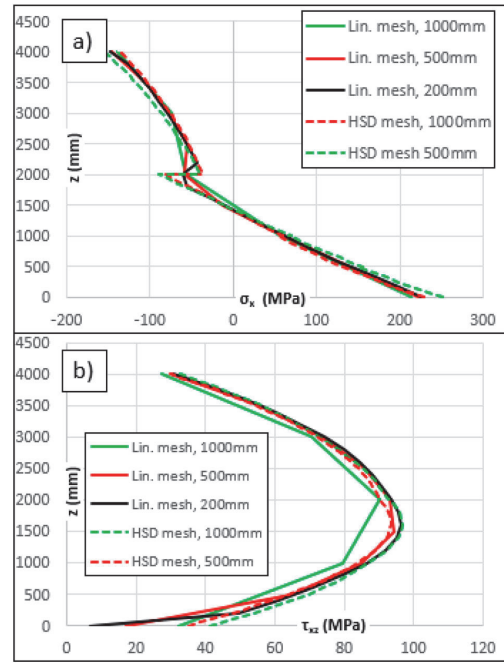

Figure 16. Vertical distributions for (a) normal stress and (b) shear stress in beam model with varying material properties (This figure is available in colour online).

linear mesh values and 3% for the varying material beam model.

Vertical stress distribution for varying thickness model in Figure 15, and varying material model in Figure 16 reveal insights into stress behaviour at the transition layer. Differences in normal stress distributions can be explained using general Hooke's:

$$\sigma = E * \varepsilon$$

where geometric constraints prohibit individual elongation creating a continuous deformation ε curve over the height of the beam. Normal stress is thus dependent on Young's modulus E resulting in a non-continuous distribution in the material variance model and a continuous distribution in the thickness variance model. Figure 15(a) shows how all meshing methods provide accurate results, however, non-continuous normal stress is only captured with the HSD mesh types in Figure 16(a) with no clear reduced accuracy between the HSD mesh sizes in simple bending conditions.

Vertical shear stress distributions for thickness variance in Figure 15(b) and material variance in Figure 16(b) similarly show different behaviour at the transition layer. Here, shear stress becomes non-continuous

based on Hooke's law for shear stress:

$$\sigma = G * \varepsilon, \tag{83}$$

where thickness is in direct correlation with stiffness and consequently in inverse correlation with deformation and stress: $t \sim K \sim 1/\varepsilon \rightarrow t \sim 1/\sigma$. The HSD formulation, regardless of the mesh size interpolates stress values closer to the transition and provides more accurate stress results than fine linear mesh. For simple bending conditions, the 1000, 500, and 200 mm linear mesh peak stress values are 22%, 7,2%, and 1,6% underestimated respectively compared to the 1000 mm HSD formulation mesh.

Shear stress values for material variance in Figure 16(b) show indifference to material variance as shear modulus is in direct correlation with shear stress based on Eq. (76) as well as in inverse relation to deformation: $G \sim K \sim 1/\varepsilon$. Although results show overall coincidence, the HSD formulation is applicable with a coarse 1000 mm mesh, whereas linear mesh in that size shows a clear lack of nodal density with peak stress being underestimated by 6% compared to each other.

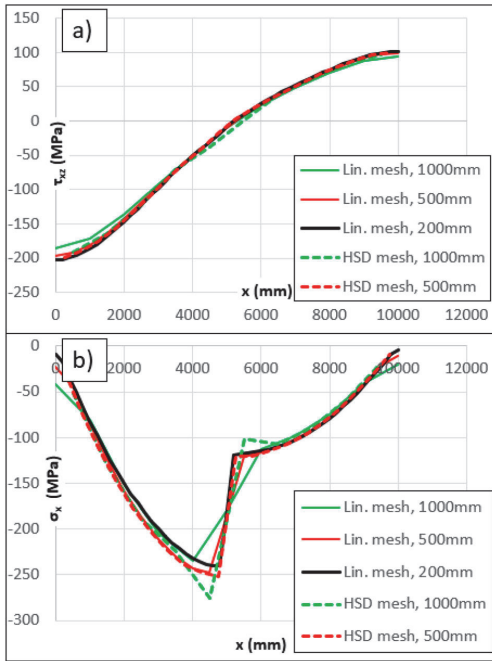Figures 17 and 18 reveal highly corresponding longitudinal normal and shear stress distributions. However,

Figure 17. Longitudinal distributions for (a) shear stress and (b) normal stress in beam model with varying plate thickness (This figure is available in colour online).

Figure 18. Longitudinal distributions for (a) shear stress and (b) normal stress in beam model with varying material properties (This figure is available in colour online).

critical limitations emerge in the degrees of freedom assumptions in elements adjacent to the transition plane at the beams midlength. In longitudinally varying models, deflection rate $\partial w/\partial x$ cannot be considered consistent in neighboring elements at the transition layer, which leads to stress evaluation discrepancies. Stress results between 1000 and 500 mm HSD mesh models show that with decreased element sizing this deficiency is mitigated. Additionally, normal stress distributions show highly corresponding results as this limitation is not noticeable in linearly behaving midship areas in Figure 17(a) and Figure 18(a).

4.2. Numerical results for the 3D box stepped box model

A good indication of the general accuracy of global response between all mesh types is evident in the deflection distribution graphs in Figure 19. Numeric results in the bottom and top edges are highly accurate as the graphs show differences of 2,0% and 5,3% respectively in maximum deflection for both coarse mesh types compared to fine mesh results.

The horizontal and vertical stress distribution graphs are shown for a selection of planes and cross-sections.
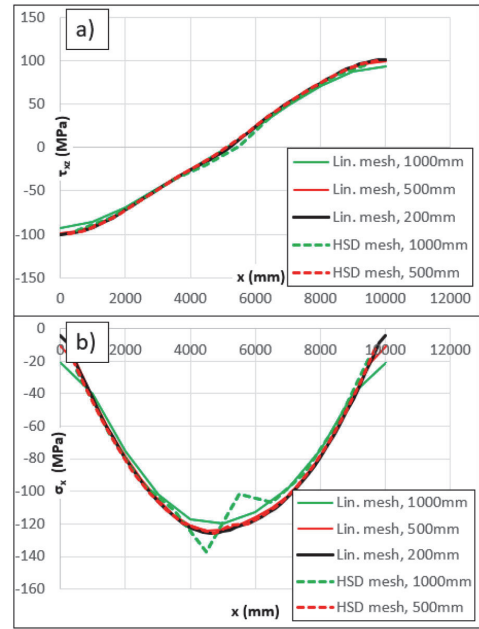
Shear stress horizontal planes are defined in the stress-critical transitional layers between changing plate thicknesses and material properties where stress distribution is discontinuous. Cross-sections are chosen to describe a more linearly behaving section in the midship and the steep gradient behaviour close to structural discontinuities.

Longitudinal stress distributions have been analysed in transitional layers at $z = 6, 4$ m, where the hull transitions into superstructure which includes the lowering of Young's modulus in the outer layer as well as the transition from 10 mm thick plating into 6 mm thick plating in both the outer and inner longitudinal walls. The second layer has been defined at $z = 9, 4$ m, where the superstructure experiences an additional step and the transition from 6 mm thick plating into 8 mm thick plating. The third layer is defined at $z = 12, 4$ m which marks the topmost layer of the vertical walls at the intersection with the top deck plating.

In the fine linear mesh, the stress values are described as elemental values in the first elements under the transition layer. For coarse and semi-coarse linear mesh models, elemental stress values of vertical elements have been averaged into nodal values and thus the stress
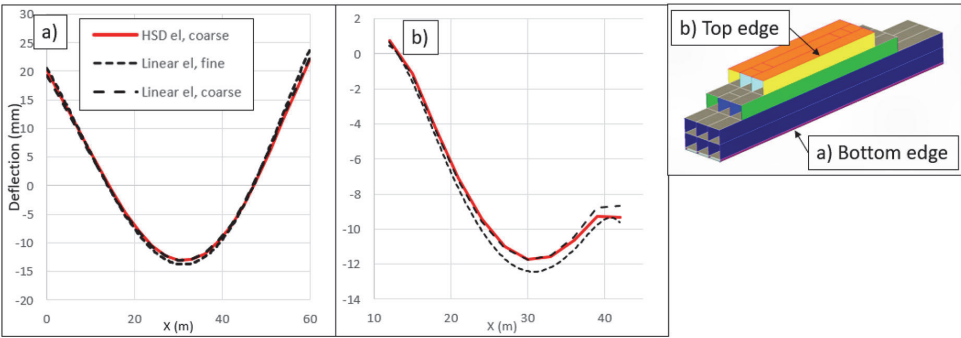
Figure 19. Global deflection comparison in (a) bottom edge, (b) top edge (This figure is available in colour online).

values are described directly at the transition layer. In the HSD elements, the stress values are approximated at the transition layer.

The normal and shear stress distributions in Figures 20–22 show a generally good agreement between the different meshing with clear deficiencies in evaluation
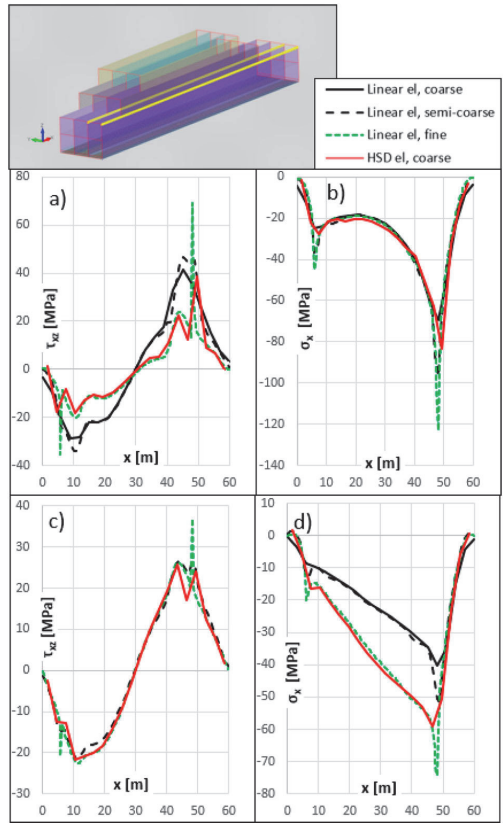

Figure 20. Longitudinal distribution at $z = 6, 4$ m for (a) inner wall shear stress, (b) inner wall normal stress, (c) outer wall shear stress, (d) outer wall normal stress (This figure is available in colour online).
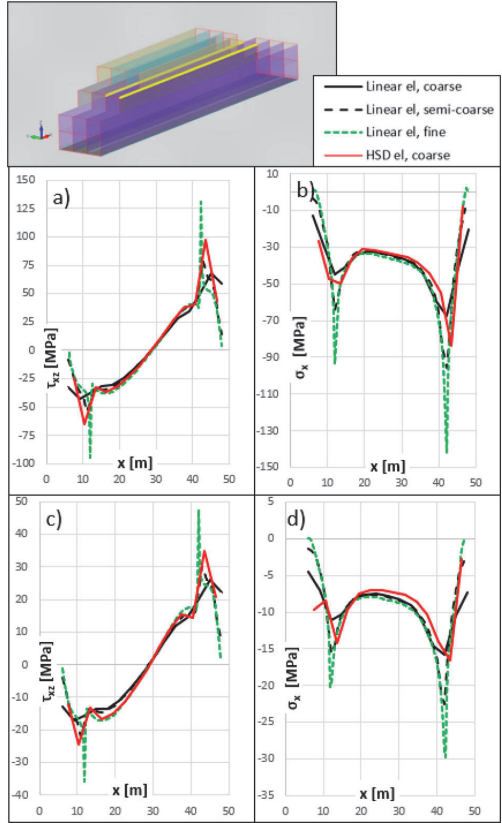

Figure 21. Longitudinal distribution at $z = 9, 4$ m for (a) inner wall shear stress, (b) inner wall normal stress, (c) outer wall shear stress, (d) outer wall normal stress (This figure is available in colour online).
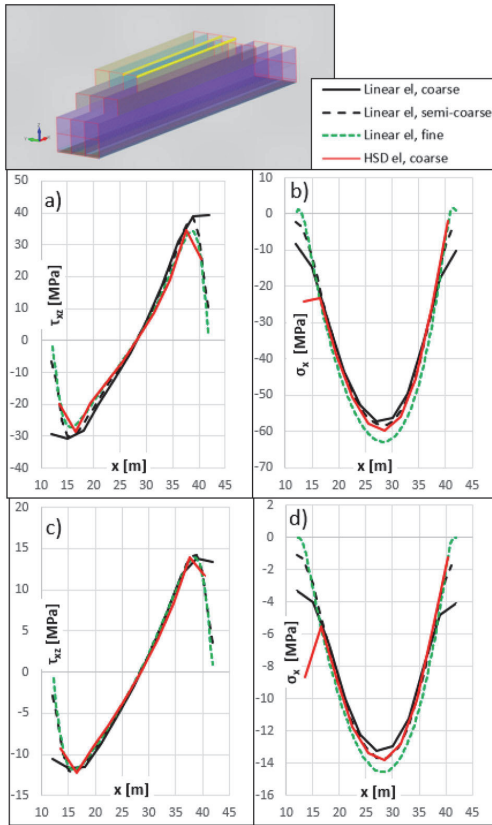
accuracy of discontinuities in stress distributions and peak stress values.

Due to big variation in material stiffness in the outside walls at plane $z = 6, 4$ m, the normal stress values in the outer wall and shear stress values in the inner walls show big inconsistencies between the linear course and semi-coarse mesh, when analysed for the agreement with linear fine mesh results. The HSD mesh shows excellent consistency to fine mesh results in these areas.

As the load-carrying abilities in the superstructure outside walls decrease due to the lowered material properties, the shear stress load path travels from the outside wall to the inner longitudinal bulkhead, thus significantly increasing shear stress values above deck 3, see Figure 10(c). In coarse mesh linear element models, this change is not accurately captured close to the transition layers, where significant peak values might occur due to nodal averaging of stresses. HSD element values, however, show particularly good accuracy compared to the fine linear mesh model. Shear stress values are presented in Figure 23 for both approach directions denoted as top and bottom elements referencing the positioning regards the transition layer. At the coordinate $x = 11$ m, where secondary peak stresses occur, coarse HSD element mesh produces results within a 5% and 2% margin in the upper and lower element respectively. Semi-coarse linear mesh produces results within 34% and 70% margin respectively. At the foreship secondary peak stress area at $x = 43, 5$ m the correlating margin percentages are 16% and 3% for HSD element mesh and 70% and 47% for semi-coarse linear mesh respectively. Secondary peak stress areas are analysed as local peak stress effects are more limited.
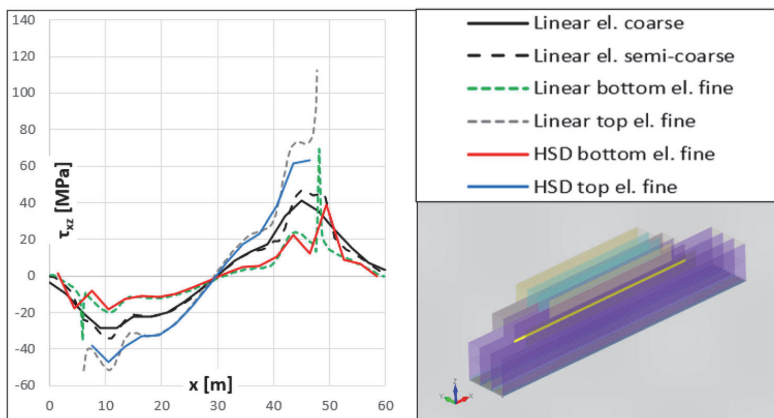

Figure 22. Longitudinal distribution at $z = 12, 4$ m for (a) inner wall shear stress, (b) inner wall normal stress, (c) outer wall shear stress, (d) outer wall normal stress (This figure is available in colour online).

Figure 23. Shear stress longitudinal distribution at $z = 6, 4$ m in inner wall (This figure is available in colour online).
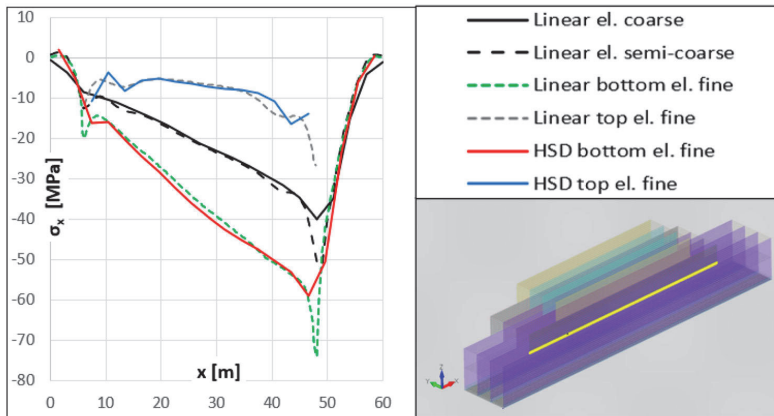
Figure 24. Normal stress longitudinal distribution at $z = 6, 4$ m in outer wall (This figure is available in colour online).

When analysing the normal stress values in the transition layer in the outer wall in Figure 24, the nodal stress description between the coarse and semi-coarse linear mesh results shows higher inconsistencies than the HSD element results about the fine linear mesh results. At secondary peak stress areas at $x = 13, 5$ m, normal stress margins in the upper and lower element for HSD element are 15% and 4%, and for linear semi-coarse mesh 85% and 47% respectively. In the foreship secondary peak stress location at $x = 43, 5$ m HSD element normal stress margins are 13% and 4% in the upper and lower element and 127% and 40% respectively for semi-coarse linear mesh.

Second, a general conclusion can be made that the peak stress values in the areas of discontinuities are generally underestimated due to the bigger element size when compared to the linear fine mesh model. Table 1 presents peak stress difference percentages between coarse linear, semi-coarse linear, and coarse HSD mesh models compared to fine linear mesh model in both aft and foreship areas. A consistently lower difference percentage can be concluded for the HSD mesh when compared to the coarse linear mesh. A clear conclusion cannot be made between semi-coarse linear mesh results and coarse HSD mesh, however, the difference in mesh sizes suggests that the HSD element formulation can be used for computational cost benefits without losing accuracy in peak stresses.

The analysis of cross-sectional stress distributions shows more in detail the deficiencies that coarse linear meshes have and how these are mitigated with HSD elements. Four cross-sections have been analysed, of which one cross-section at $x = 22, 5$ $x = 43, 5$ m (Figure 25) represents the behaviour in the midship

portion of the stepped box model, while cross-sections at $x = 34, 5$ m, $x = 40, 5$ m, and $x = 43, 5$ m (Figures 26–28) describe the stress distributions in the area of structural discontinuities. While the HSD element can describe the noncontinuity of stresses, averaged nodal stress values for coarse and semi-coarse linear mesh lose a significant amount of peak stress data in all vertical stress distribution graphs. The results for HSD element mesh and fine linear element mesh are highly coincident making this approach the better solution for an accurate description of stresses in structures with varying material and geometric properties. In cross-sections where the discontinuities in the model do not play a significant role, the coarse HSD element mesh provides highly accurate results.

Shear stress distributions in Figure 27(a) and Figure 27(c) show higher inconsistencies due to the proximity to the discontinuous structural edge and the top corners of the structure being inefficient in carrying shear loads.

The limiting effects of linear approximations and coarse mesh modeling are evident in Figure 28, where the shear stress value is highly inaccurate for the coarse HSD element mesh at the top surface, however, when analysed with the nodal stress values from the fine linear mesh model at $z = 9, 4$ m it is clear, how the used linear approximations in Eqs. (31) to (34) average out the peak stress values at approx. – 130 MPa and – 52 MPa, see Figure 29 and plot shear stress value at approx. – 90 MPa in Figure 29.

The effect of mesh sizing for the HSD element analysis around the discontinuities in cross-sections at $x = 40, 5$ m and $x = 43, 5$ m has been presented in Figures 30 and 31. The HSD mesh size has been

Table 1. Peak stress differences between coarse mesh models and fine linear mesh models in (a) outer wall and (b) inner wall.

a) Outer wall		Aft			Foreship		
		Lin. El. coarse	Lin. El. semi-coarse	HSD El. coarse	Lin. El. coarse	Lin. El. semi-coarse	HSD El. coarse
	Normal stress (x=7,5 / 46,5 m, Fig 20d)	57,9%	37,1%	18,8%	45,8%	30,4%	20,3%
z=9,4 m	**Shear stress** (x=10,5 / 43,5 m, Fig 21c)	52,3%	55,3%	31,8%	45,0%	36,0%	26,7%
	Normal stress (x=13,5 / 43,5 m, Fig 21d)	45,1%	22,4%	29,5%	46,8%	24,3%	44,3%
z=12,4 m	**Shear stress** (x=16,5 / 36,5 m, Fig 22c)	1,2%	-3,4%	-3,5%	0,5%	-2,9%	-0,3%
	Normal stress (x=28,5 m, Fig 22d)	8,9%	5,7%	4,9%	n/a	n/a	n/a

b) Inner wall		Aft			Foreship		
		Lin. El. coarse	Lin. El. semi-coarse	HSD El. coarse	Lin. El. coarse	Lin. El. semi-coarse	HSD El. coarse
z=6,4 m	**Shear stress** (x=4,5 / 49,5 m, Fig 20a)	42,7%	31,4%	50,4%	64,9%	62,5%	44,2%
	Normal stress (x=7,5 / 49,5 m, Fig 20b)	44,6%	18,5%	37,9%	43,3%	21,0%	31,8%
z=9,4 m	**Shear stress** (x=10,5 / 43,5 m, Fig 21a)	55,0%	56,5%	31,1%	48,3%	53,2%	25,8%
	Normal stress (x=13,5 / 43,5 m, Fig 21b)	52,0%	28,0%	47,2%	52,7%	19,8%	41,2%
z=12,4 m	**Shear stress** (x=16,5 / 37,5 m, Fig 22a)	-13,0%	-10,7%	-5,0%	-13,3%	-12,4%	-0,6%
	Normal stress (x=28,5 m, Fig 22b)	9,1%	7,2%	5,0%	n/a	n/a	n/a

increased to the semi-coarse mesh size shown in Figure 12(b). The analysis shows that by increasing mesh size, the previously shown discrepancies in Figures 27 and 28 are solved the semi-coarse HSD mesh produces highly coincident stress distributions to the fine linear mesh.

5. Concluding remarks

Structural analysis in the concept design phase seeks to describe ship structures as accurately as possible with minimal time. This is achieved by applying industry-standard meshing guidelines to element dimensioning such as implemented in Zanic et al. (2007) and various methods for defining orthogonal element descriptions such as Hughes (1989) and Avi et al. (2015). The research presented in this article further develops the finite element formulation created by Imala et al. (2022) to improve the accuracy of concept design analyses by utilising higher-order formulations in the finite element descriptions that are specifically created for marine industry applications.
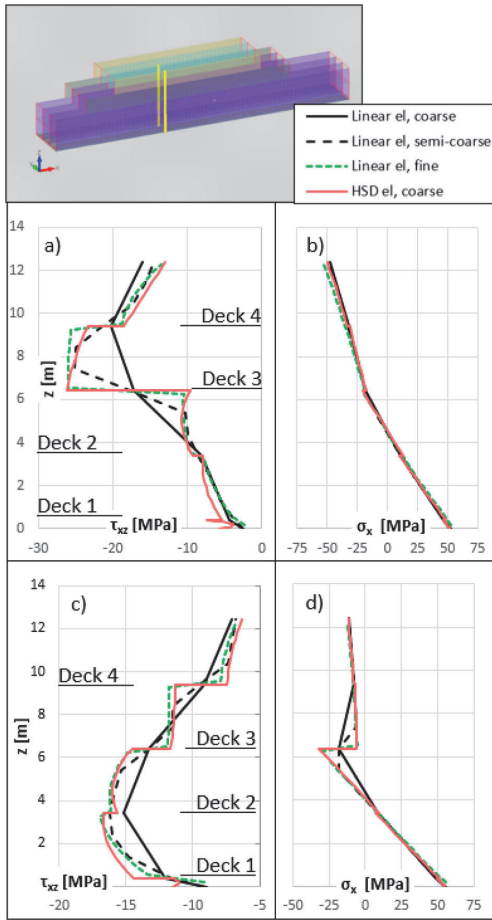
Figure 25. Stress vertical distributions at $x = 22, 5$ m for (a) shear stress in inner bulkhead, (b) normal stress in inner bulkhead, (c) shear stress in outer shell, (d) normal stress in outer shell (This figure is available in colour online).

Figure 26. Stress vertical distributions at $x = 34, 5$ m for (a) shear stress in inner bulkhead, (b) normal stress in inner bulkhead, (c) shear stress in outer shell, (d) normal stress in outer shell (This figure is available in colour online).

In complex structures, stress concentrations at geometrical discontinuities and in layers with changing topological characteristics have a significant impact on the feasibility of structural design. The higher-order shear deformation formulation presented in this article evaluates the global static response of a hull girder with special emphasis on evaluating stress distributions in structural transition layers. The formulation introduces separate definitions for a 4-node shear element positioned vertically and horizontally due to different sets of approximations between homogeneous six-degree-of-freedom nodes. The vertical element proposes a finite element description that allows normal and
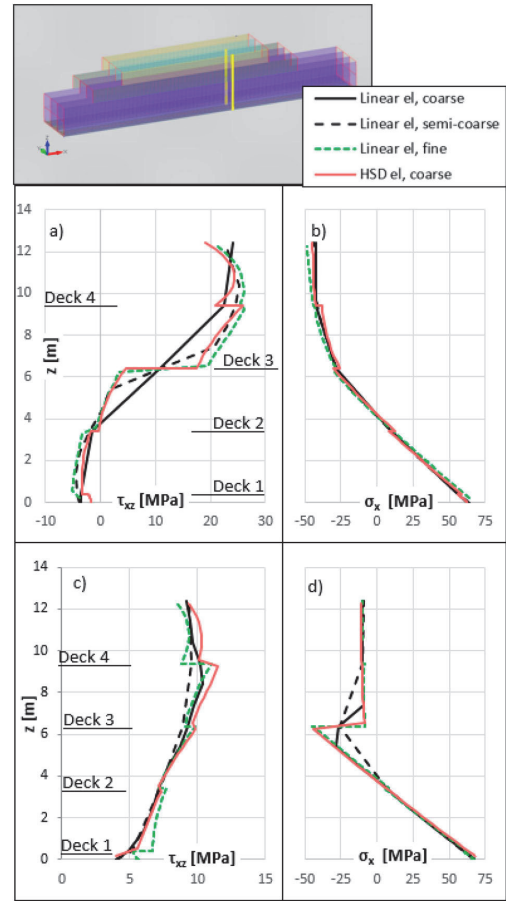
shear stress to be calculated in a node independently for all elements containing that node by including element-specific material and thickness information.

The proposed methodology is initially validated on a simple beam model and then tested in marine structure applications, where the material and topological parameters for structures are highly varying. In all analyses, the numeric results from a fine mesh linear element model are defined as the comparison standard. The numerical results of the similarly sized linear mesh model and the HSD element mesh model are evaluated against the standard.

The initial validation analysis defines a simple beam model with varying plate thicknesses and material
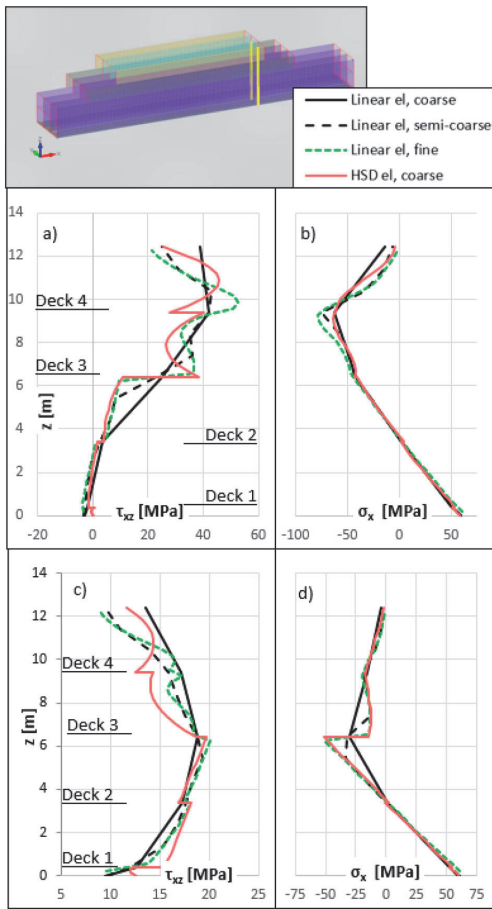
Figure 27. Stress vertical distributions at $x = 40, 5$ m for (a) shear stress in inner bulkhead, (b) normal stress in inner bulkhead, (c) shear stress in outer shell, (d) normal stress in outer shell (This figure is available in colour online).

Figure 28. Stress vertical distributions at $x = 43, 5$ m for (a) shear stress in inner bulkhead, (b) normal stress in inner bulkhead, (c) shear stress in outer shell, (d) normal stress in outer shell (This figure is available in colour online).

properties in vertical and longitudinal directions to evaluate mesh sizing effects on a beam bending response. The marine analysis focuses on a 3D stepped box model use case that introduces a shear-weakened superstructure outer shell using lowered stiffness parameters and reduced plate thickness resembling real-world marine applications which allows for more realistic stress distributions to be investigated.

In the simply supported beam analyses, the HSD coarse mesh models showed excellent ability to evaluate stresses at transition layers, whereas linear mesh models underestimated peak stress values by 22% in the coarse mesh model and 1.6% in the fine mesh model, showing the potential of evaluating non-linear and non-continuous stress distributions with a limited number of
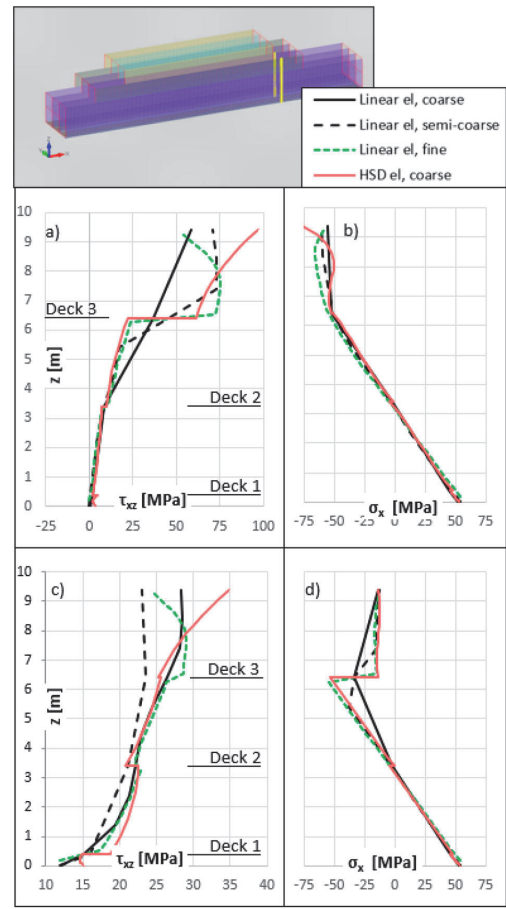
elements over the height of the beam. Additionally, the HSD formulation proved to be highly accurate for the typical static response analysis for passenger ships. In topological or parametrical transition layers, the coarse HSD mesh models showed excellent agreement in normal and shear stress comparisons with linear fine mesh results outperforming coarse and semi-coarse linear mesh models. The HSD element further validated the ability to describe the discontinuities in shear and normal stress vertical distributions as well as more accurately assess peak stress values for longitudinal stress distributions.

In practice, this higher-order finite element formulation allows for an accurate estimation of ship structures in the conceptual design phase outperforming
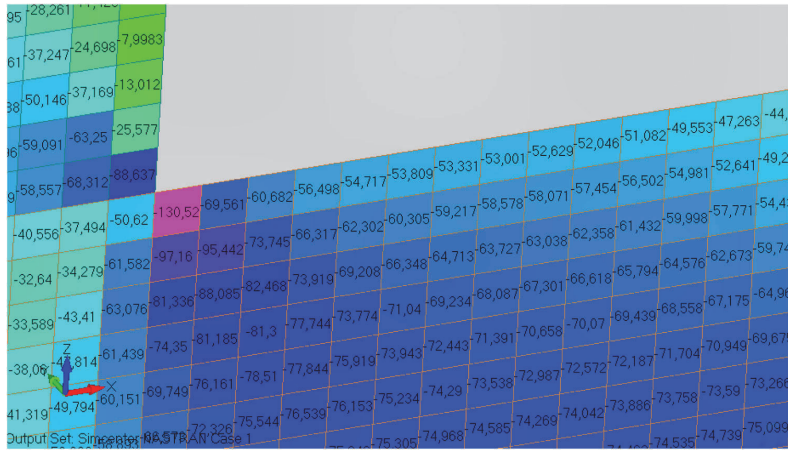
Figure 29. Local elemental shear stress values in the inner wall at cross-section $x = 43, 5$ m (This figure is available in colour online).
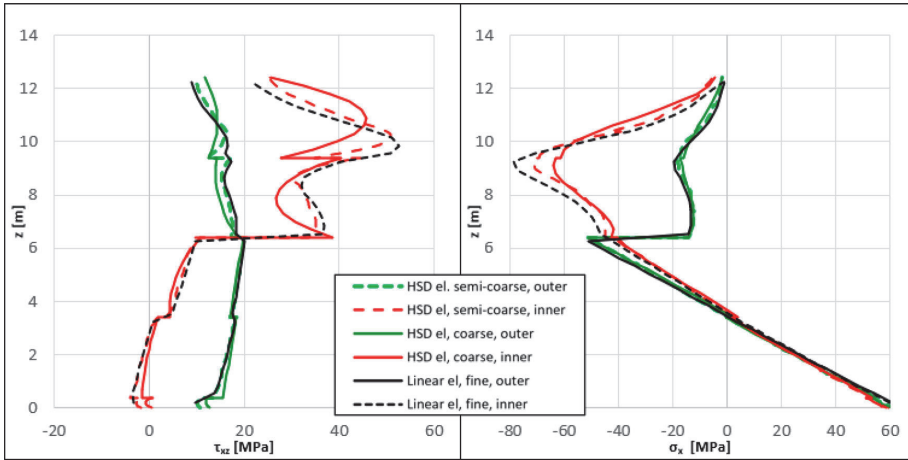

Figure 30. Effects of HSD mesh sizing on stress distributions at $x = 40, 5$ m (This figure is available in colour online).
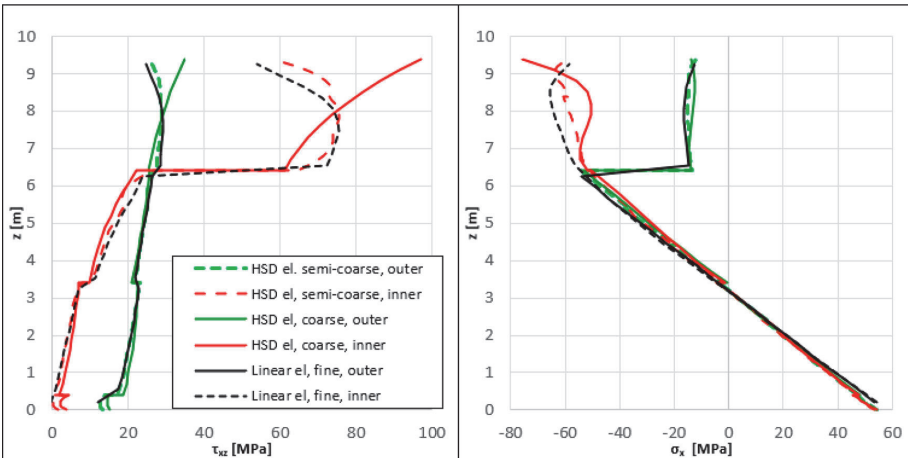

Figure 31. Effects of HSD mesh sizing on stress distributions at $x = 43, 5$ m (This figure is available in colour online).

identically sized linear finite element mesh. The method serves as an alternative for detailed 3D finite element analysis providing good accuracy at low computational cost. Complimentary to introducing the method, future developments are needed to introduce an isoparametric methodology that allows the use of oblique elements in the model. This would unlock the use of 4-node and 3-node elements and release the precondition to only use main planes to orientate elements. Furthermore, a unified formulation could be developed to introduce out-of-plane degrees of freedom as well as allow user-defined order for shape function approximations to better align with the specific use case.

Disclosure statement

No potential conflict of interest was reported by the author(s).

Funding

Data availability statement

The data that support the findings of this study are openly available in TalTech Data Repository at https://doi.org/10.48726/dexst-9z588.

ORCID

Mikk-Markus Imala http://orcid.org/0000-0001-7278-3428

References

Avi E, Lillemäe I, Romanoff J, Niemelä A. 2015. Equivalent shell element for ship structural design. Ships Offshore Struct. 20(3):239–255. doi:10.1080/17445302.2013.819689.

Bergström M. 2010. Longitudinal strength analysis of a cruise ship with a narrow superstructure, master's thesis. Espoo. Aalto University. http://urn.fi/URN:NBN:fi:aalto-2020122357833.

Bhimaraddi A, Chandrashekhara K. 1993. Observations on higher order beam theory. J. Aerospace Eng.- ASCE. 6(4):408–413. doi:10.1061/(ASCE)0893-1321(1993)6:4(408).

Bickford WB. 1982. A consistent higher order beam theory. Development in Theoretical and Applied Mechanics, SECTAM. 11:137–150.

Bleich HH. 1953. Nonlinear distribution of bending stresses due to distortion of the cross section. J Appl Mech 20(1):95–104. doi:10.1115/1.4010600.

Crawford L. 1950. Theory of long ships' superstructure. Trans SNAME. 58:693–732.

DNV-GL. 2016. Direct strength analysis of hull structures in passenger ships. DNVGL-CG-0138.

Ghugal YM, Sharma R. 2009. A hyperbolic shear deformation theory for flexure and vibration of thick isotropic beams. Int. J. Comp. Meth. 6(4):585–604. doi:10.1142/S0219876209002017.

Ghugal YM, Sharma R. 2011. A refined shear deformation theory for flexure of thick beams. Lat. Am. J. Solids Stru. 8(2):183–195. doi:10.1590/S1679-78252011000200005.

Hughes OF. 1989. Ship structural design. Jersey city: Society of Naval Architects and Marine Engineers.

Imala MM, Naar H, Tabri K, Romanoff J. 2022. Toward the application of the layer-wise displacement theory in passenger ships—a quasi-static response. Mech Adv Mater Struct. 30(22):4698–4710. doi:10.1080/15376494.2022.2103859.

ISSC. 1997. Committee II.1 – quasi-static response. Proceedings of the 13th International Ship and Offshore Structures Congress; 1997 Aug 18–22; Trondheim, Norway. Oxford: Elsevier Science. p. 158–165.

Lillemäe I, Remes H, Romanoff J. 2014. Influence of initial distortion of 3 mm thin superstructure decks on hull girder response for fatigue assessment. Mar Struct. 37:203–218. doi:10.1016/j.marstruc.2014.04.001.

Morshedsoluk F, Khedmati MR. 2016. Ultimate strength of composite ships' hull girders on the presence of composite superstructures. Thin-Walled Struct. 102:122–138. doi:10.1016/j.tws.2016.01.024.

Murty K, V A. 1984. Towards a consistent beam theory. AIAA J. 22(6):811–816. doi:10.2514/3.8685.

Naar H, Varsta P, Kujala P. 2004. A theory of coupled beams for strength assessment of passenger ships. Mar. Struct. 17:590–611. doi:10.1016/j.marstruc.2005.03.004.

Parmasto O, Romanoff J, Remes H. 2013. Hull-superstructure interaction induced secondary effects in passenger ships. In: Proceedings of the 12th International Symposium on Practical Design of Ships and Other Floating Structures. PRADS2013:290–294.

Raikunen J, Avi E, Remes H, Romanoff J, Lillemäe-Avi I, Niemelä A. 2019. Optimisation of passenger ship structures in concept design stage. Ships Offshore Struct. 14(1):320–334. doi:10.1080/17445302.2019.1590947.

Reddy JN. 1984. A simple higher-order theory for laminated composite plates. J Appl Mech 51(4):745–752. doi:10.1115/1.3167719.

Reddy JN. 1987. A generalization of two-dimensional theories of laminated composite plates. Commun Appl Numer Meth. 3(3):173–180. doi:10.1002/cnm.1630030303.

Reddy JN. 2004. Mechanics of laminated composite plates and shells – theory and analysis, 2nd ed. Boca Raton, FL: CRC Press.

Ringsberg JW, Saglam H, Sarder MA, Ulfvarson A. 2012. Lightweight design of offshore platform marine structures – optimization of weight to strength utilization of corrugated shell plating. Ships Offshore Struct. 9(1):38–53. doi:10.1080/17445302.2012.712005.

Robbins DH, Reddy JN. 1991. Analysis of piezoelectrically actuated beams using a layer-wise displacement theory. Comput Struct. 41(2):265–279. DOI: 10.1016/0045-7949(91)90430-T

Romanoff J, Varsta P. 2007. Bending response of web-core sandwich plates. Compos Struct. 81:292–302. doi:10.1016/j.compstruct.2006.08.021.

Romanoff J, Karttunen A, Varsta P, Remes H, Goncalves BR. 2020. A review on non-classical continuum mechanics with applications in marine engineering. Mech Adv Mater Struct 27(13):1065–1075. doi:10.1080/15376494.2020.1717693.

Romanoff J, Remes H, Varsta P. 2013. Hull-superstructure interaction in optimised passanger ships. J. Ships Offshore Struct. 8:612–620. doi:10.1080/17445302.2012.675196.

Shi G, Gao D. 2019. Analysis of hull girder ultimate strength for cruise ship with multi-layer superstructures. Ships Offshore Struc. 14(7):698–708. doi:10.1080/17445302.2018.1552548.

Shi G, Gao D. 2021. Model experiment of large superstructures' influence on hull girder ultimate strength for cruise ships. Ocean Eng 222:108626. doi:10.1016/j.oceaneng.2021.108626.

Teguh P, Kõrgesaar M, Jelovica J, Tabri K, Naar H. 2021. Ultimate strength assessment of stiffened panel under uni-axial compression with non-linear equivalent single layer approach. Mar. Struct. 78:103004.

Toledano A, Murakami H. 1987. A high-order laminated plate theory with improved in-plane responses. Int. J. Solids and Struct. 23:111–131. doi:10.1016/0020-7683(87)90034-5.

Toming R, Kerge EH, Naar H, Tabri K, Romanoff J, Remes H. 2016. Hull and superstructure interaction using coupled beam method. Proceedings of PRADS2016, 4th-8th September, 2016, Copenhagen, Denmark, pp. 851-859.

Tsitsilonis K, Stefanidis F, Mavrelos C, Gad A, Timmerman M, Vassalos D, Kaklis P. 2018. Concept design considerations for the next generation of mega-ships. Marine Design XIII: Proceedings of the 13th International Marine Design Conference (IMDC 2018). 1:579–588.

Yang B, Pei Z, Wu W. 2022. Stress-distribution characteristics of cruise ship based on multiple-beam method. Ocean Eng 266(1):112646. doi:10.1016/j.oceaneng.2022.112646.

Zanic V, Andric J, Prebeg P. 2007. Decision support methodology for concept design of multi-deck ship structures. Proceedings of the 10th International Symposium of Practical Design of Ships and Other Floating Structures, Sep 30-Oct 5, Houston (TX). p. 468–476.

Zanic V, Andric J, Prebeg P. 2013. Design synthesis of complex ship structures. Ships Offshore Struct. 8:383–403. doi:10.1080/17445302.2013.783455.

Appendix 3

Publication III

Passenger ship global static response analysis implementing a modified higher-order shear element description

M.M. Imala, H. Naar & K. Tabri

Tallinn University of Technology, School of Engineering

ABSTRACT: This paper analyses the structural response of a passenger ships using a higher-order shear deformation (HSD) method. The methodology utilises third-order polynomial displacement fields to analyse stress distributions in complex ship structures, incorporating discontinuous multi-deck configuration and partial-length superstructures. The study applies the method to a conceptual cruise ship model, evaluating longitudinal and vertical shear stress distributions across different topological and geometrical transitions. Results demonstrate the method's effectiveness in capturing accurate stress distributions and peak stress values while maintaining computational efficiency comparable to traditional finite element methods.

1 INTRODUCTION

The structural analysis of modern passenger ships faces increasing complexity due to architectural innovations and growing vessel sizes. While 3D finite element analysis (FEA) remains the industry standard, linear coarse mesh models lack accuracy in stress-critical areas. In contrast, the computational demands and the level of design progression needed to make fine mesh applications impractical for conceptual design. Previous research has approached this challenge at two distinct levels. At the macro level, original beam theory applications by Crawford (1950) and Bleich (1953) and layer-wise methods like the Coupled Beam theory by Naar et al. (2004) and (2006) have been developed to analyse hull-superstructure interactions of complete ship sections. At the panel level, equivalent single-layer techniques have been created by Zanic et al. (2013), Romanoff & Varsta (2007), Avi et al. (2015), and Teguh et al. (2021) to represent complex stiffened structures as simplified orthotropic elements extending the work of Reddy (2004). These approaches, while efficient, often struggle to accurately capture discontinuous shear effects that are crucial in modern passenger ship structures with varying topology and material definitions.

Our approach bridges this gap by adapting the higher-order shear deformation theory developed by Reddy (1984) for composite laminates to ship structural analysis. The marine applications are introduced by Imala et al. (2022) and Imala et al. (2025) by utilising a third-order polynomial description for in-plane displacement. This theory provides a superior representation of vertical and horizontal distributions of shear stresses compared to first-order theories. We extend this formulation by incorporating vertical transversal element definitions, enabling a more accurate representation of structural interactions in passenger ships. The proposed methodology is validated using a 3D conceptual cruise ship model.

2 MODIFIED HIGHER-ORDER SHEAR DEFORMATION METHOD

The methodology used in this article closely follows the higher-order shear deformation method presented by Imala et al. (2025). Few modifications have been introduced to describe a multideck passenger ship more accurately, where the transversal bulkheads play a significant role in the ship's global stress response. Therefore, displacement field definitions have been added for vertical transverse elements and updated for vertical longitudinal elements in addition to updating the definition of shear deformation variable to reflect the addition of transverse vertical elements.

2.1 *Shear deformation variable definition*

The HSD theory utilises a homogeneous nodal degree of freedom mapping in the global Cartesian coordinate system, aligning the x-axis with the longitudinal direction, the y-axis with the transversal direction, and the z-axis with the vertical direction:

u, v, w – translations respectively in x, y, z axis directions, d – equilibrium force per unit length, jv/jx, jw/jx – deformations in the direction of the shared edge between the deck and longitudinal vertical elements.

The degree of freedom d is expressed as:

$$\delta = \delta_{el1} + \delta_{el2} + \delta_{el3} = \left(\frac{\partial u}{\partial z} + \frac{\partial w}{\partial x}\right)t\left(\frac{G}{G_0}\right) +$$

$$\left(\left(\frac{\partial u}{\partial y}\right)^* + \frac{\partial v}{\partial x}\right)t^*\left(\frac{G^*}{G_0}\right) + \left(\frac{\partial v}{\partial z} + \left(\frac{\partial w}{\partial y}\right)^{**}\right)t^{**}\left(\frac{G^{**}}{G_0}\right),$$

$$(1)$$

where degree of freedom value d comprises of neighbouring element specific d_{el1}, d_{el2}, d_{el3} values. Additionally, $(ju/jy)^*$, t^*, G^* are parameters of a neighbouring horizontal element, $(jw/jy)^{**}$, t^{**}, G^{**} are parameters of a neighbouring transversal vertical element, and G_0 is a reference shear modulus value to account for the change in material properties in adjacent elements. The reference shear modulus value is calculated as follows:

$$G_0 = \frac{\sum_{i=1}^{n} G_i}{n}, \tag{2}$$

where G_i denote the shear moduli used in the analysis.

Deformation parameters $(ju/jy)^*$ and $(jw/jy)^{**}$ are always considered in the direction of the positive axis.

Equation for describing the degree of freedom is explained in a local system presented in Figure 1 a), where *El1* and *El2* share an edge and force per length equilibrium is investigated at global coordinates coinciding with nodes $n_{1,2}$ and $n_{2,3}$.
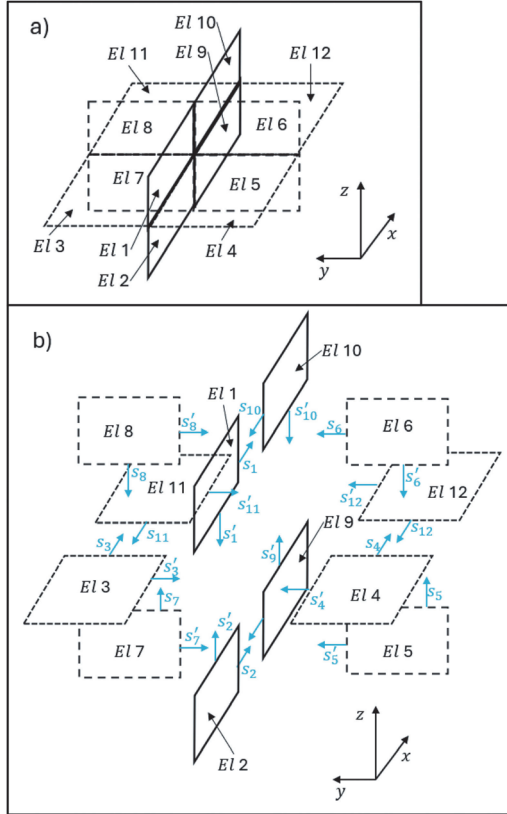

Figure 1. Example element intersection for a) non-exploded view b) for exploded view with edge normal directions.

Grouping method for neighbouring elements based on the polarity of the coincident edge normal has been defined to describe the equilibrium force per unit length degree of freedom d present in the definition of the vertical longitudinal elements.

In general form, the equilibrium equation between any coincident vertical longitudinal element node is described as:

$$\sum_{i=1}^{n} \delta_{el,i} S_i S_i^{'} = 0, \tag{3}$$

where s_i and $s_i^{'}$ show the direction of edge normal and obtain polarity values (1;-1) referring to the positive and negative direction related to the global coordinate system. Additionally, $\delta_{el,i}$ denotes the element specific force value.

An exploded view of the element group is shown in Figure 1 b), for which force equilibrium equation after inserting polarity values is described as:

$$\delta_{el2} - \delta_{el1} - \delta_{el3} + \delta_{el4} + \delta_{el5} - \delta_{el6} - \delta_{el7}$$
$$+\delta_{el8} - \delta_{el9} + \delta_{el10} + \delta_{el11} - \delta_{el12} = 0. \tag{4}$$

The equilibrium can be presented alternatively by separating the positively and negatively signed components as:

$$\delta_{el2} + \delta_{el4} + \delta_{el5} + \delta_{el8} + \delta_{el10} + \delta_{el11}$$
$$= \delta_{el1} + \delta_{el3} + \delta_{el6} + \delta_{el7} + \delta_{el9} + \delta_{el12}. \tag{5}$$

Eq. (5) can be further grouped by introducing matching components to the definition of the degree of freedom in Eq. (1):

$$\delta_{el2} + \delta_{el4} + \delta_{el5} = \delta_2, \tag{6}$$
$$\delta_{el8} + \delta_{el10} + \delta_{el11} = \delta_{10}, \tag{7}$$
$$\delta_{el1} + \delta_{el3} + \delta_{el6} = \delta_1, \tag{8}$$
$$\delta_{el7} + \delta_{el9} + \delta_{el12} = \delta_9, \tag{9}$$

where

$$\delta_1 = \delta_2 = \delta_9 = \delta_{10} = \delta. \tag{10}$$

In Equations (6) to (9) the elemental components with coincident edges are grouped with vertical longitudinal element component resulting in two necessary conditions when pairing elements for Eq. (1):

• Elements share an edge,
• Coincident edge normal directions simultaneously in positive or negative global coordinate system axis direction.

Eq. (1) is further expanded according to examples shown in a) and b). The former shows the contributing elements to describing $d_{2,3}$ as:

$$\delta_{2,3} = \delta_{el2,3} + \delta_{el4,3} + \delta_{el5,3}. \tag{11}$$

while the latter shows the contributing elements to describing $d_{1,2}$ as:

$$\delta_{1,2} = \delta_{el1,2} + \delta_{el3,2} + \delta_{el6,2}. \tag{12}$$

After replacing Eq. (6) and (8) to Eq. (1) and expanding to include nodal displacements, the shear deformation degree of freedom in nodes $n_{1,2}$ and $n_{2,3}$ is respectively described as:

$$\delta_{1,2} = \left(\left(\frac{\partial u}{\partial z} \right)_{1,2} + \left(\frac{\partial w}{\partial x} \right)_{1,2} \right) t_{el1} \left(\frac{G_{el1}}{G_0} \right)$$

$$+ \left(\frac{u_{3,3} - u_{3,2}}{h_{el3}} + \left(\frac{\partial v}{\partial x} \right)_{3,2} \right) t_{el3} \left(\frac{G_{el3}}{G_0} \right)$$

$$+ \left(\frac{v_{6,3} - v_{6,2}}{h_{el6}} + \frac{w_{6,2} - w_{6,1}}{l_{el6}} \right) t_{el6} \left(\frac{G_{el6}}{G_0} \right), \quad (13)$$

$$\delta_{2,3} = \left(\left(\frac{\partial u}{\partial z} \right)_{2,3} + \left(\frac{\partial w}{\partial x} \right)_{2,3} \right) t_{el2} \left(\frac{G_{el2}}{G_0} \right)$$

$$+ \left(\frac{u_{4,3} - u_{4,2}}{h_{el4}} + \left(\frac{\partial v}{\partial x} \right)_{4,3} \right) t_{el4} \left(\frac{G_{el4}}{G_0} \right)$$

$$+ \left(\frac{v_{5,3} - v_{5,2}}{h_{el5}} + \frac{w_{5,3} - w_{5,4}}{l_{el5}} \right) t_{el5} \left(\frac{G_{el5}}{G_0} \right). \quad (14)$$
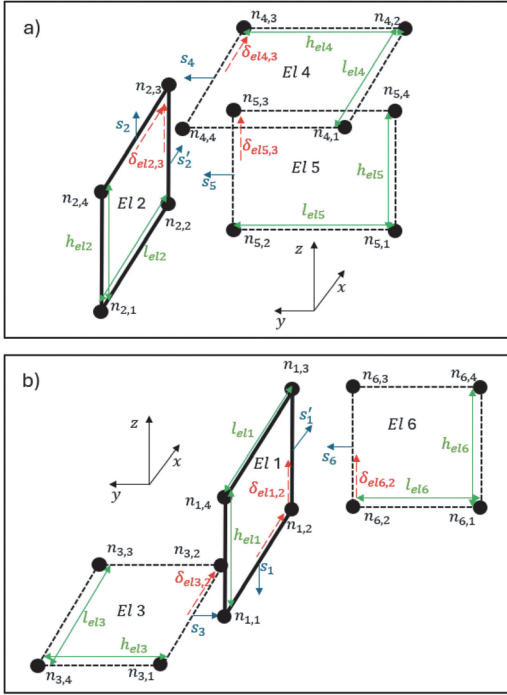

Figure 2. Contributing elements to a) d$_{2,3}$ and b) d$_{1,2}$.

Equations (13) and (14) can be alternatively presented after replacing shared nodal displacement and deformation values as:

$$\delta_{total1,2} = \left(\left(\frac{\partial u}{\partial z} \right)_{1,2} + \left(\frac{\partial w}{\partial x} \right)_{1,2} \right) t_{el1} \left(\frac{G_{el1}}{G_0} \right)$$

$$+ \left(\frac{u_{3,3} - u_{1,2}}{h_{el3}} + \left(\frac{\partial v}{\partial x} \right)_{1,2} \right) t_{el3} \left(\frac{G_{el3}}{G_0} \right)$$

$$+ \left(\frac{v_{1,3} - v_{1,2}}{h_{el1}} + \frac{w_{1,2} - w_{6,1}}{l_{el6}} \right) t_{el6} \left(\frac{G_{el6}}{G_0} \right), \quad (15)$$

$$\delta_{total2,3} = \left(\left(\frac{\partial u}{\partial z} \right)_{2,3} + \left(\frac{\partial w}{\partial x} \right)_{2,3} \right) t_{el2} \left(\frac{G_{el2}}{G_0} \right)$$

$$+ \left(\frac{u_{2,3} - u_{4,2}}{h_{el4}} + \left(\frac{\partial v}{\partial x} \right)_{2,3} \right) t_{el4} \left(\frac{G_{el4}}{G_0} \right)$$

$$+ \left(\frac{v_{2,3} - v_{2,2}}{h_{el2}} + \frac{w_{2,3} - w_{5,4}}{l_{el5}} \right) t_{el5} \left(\frac{G_{el5}}{G_0} \right) \quad (16)$$

2.2 Displacement field definitions for vertical elements

Vertical transversal element has been defined using a simple linear element description, where the non-zero nodal degrees of freedom are the planar displacements shown in Figure 3.
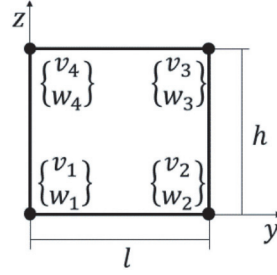

Figure 3. Degrees of freedom for vertical plating elements.

Displacement field definitions for in-plane displacements for such elements incorporate first-order polynomials introduced by Imala et al. (2025):

$$v(y,z) = \varepsilon_1(z)\phi_1(y)v_1 + \varepsilon_1(z)\phi_2(y)v_2 +$$
$$\varepsilon_2(z)\phi_1(y)v_4 + \varepsilon_2(z)\phi_2(y)v_3 \quad (17)$$

$$w(y,z) = \varepsilon_1(z)\phi_1(y)w_1 + \varepsilon_1(z)\phi_2(y)w_2 +$$
$$\varepsilon_2(z)\phi_1(y)w_4 + \varepsilon_2(z)\phi_2(y)w_3 \quad (18)$$

Finite element formulation for transversal vertical elements follows previously presented methodology by Imala et al. (2025).

Displacement field definitions for longitudinal vertical elements in Imala et al. (2025) are modified to include the updated definition for the shear deformation variable in Eq. (1):

$$u(x,z) = \psi_1(w)\phi_1(x)u_1 + \psi_2(w)\phi_1(x)\left(\frac{\partial u}{\partial z} \right)_1$$

$$+ \psi_1(z)\phi_2(x)u_2 + \psi_2(z)\phi_2(x)\left(\frac{\partial u}{\partial z} \right)_2$$

$$+ \psi_3(z)\phi_2(x)u_3 + \psi_4(z)\phi_2(x)\left(\frac{\partial u}{\partial z} \right)_3$$

$$+ \psi_3(z)\phi_1(x)u_4 + \psi_4(z)\phi_1(x)\left(\frac{\partial u}{\partial z} \right)_4, \quad (19)$$

$$w(x,z) = \xi_1(z)\omega_1(x)w_1 + \xi_2(z)\omega_1(x)w_4$$

$$+ \xi_1(z)\omega_2(x)\left(\frac{\partial w}{\partial x} \right)_1 + \xi_2(z)\omega_2(x)\left(\frac{\partial w}{\partial x} \right)_4$$

$$+ \xi_1(z)\omega_3(x)w_2 + \xi_2(z)\omega_3(x)w_3$$

$$+ \xi_1(z)\omega_4(x)\left(\frac{\partial w}{\partial x} \right)_2 + \xi_2(z)\omega_4(x)\left(\frac{\partial w}{\partial x} \right)_3, \quad (20)$$

where

$$\left(\frac{\partial u}{\partial z}\right)_1 = \left(\frac{\delta_1 G_0}{tG} - \left(\frac{\partial w}{\partial x}\right)_1 - \left(\frac{u_1^* - u_1}{h^*} + \left(\frac{\partial v}{\partial x}\right)_1\right)\right.$$
$$\left.\frac{t^* G^*}{tG} - \left(\frac{v_4 - v_1}{h} + \frac{w_1^{**} - w_1}{l^{**}}\right)\frac{t^{**} G^{**}}{tG}\right), \quad (21)$$

$$\left(\frac{\partial u}{\partial z}\right)_2 = \left(\frac{\delta_2 G_0}{tG} - \left(\frac{\partial w}{\partial x}\right)_2 - \left(\frac{u_2^* - u_2}{h^*} + \left(\frac{\partial v}{\partial x}\right)_2\right)\right.$$
$$\left.\frac{t^* G^*}{tG} - \left(\frac{v_3 - v_2}{h} + \frac{w_2 - w_2^{**}}{l^{**}}\right)\frac{t^{**} G^{**}}{tG}\right), \quad (22)$$

$$\left(\frac{\partial u}{\partial z}\right)_3 = \left(\frac{\delta_3 G_0}{tG} - \left(\frac{\partial w}{\partial x}\right)_3 - \left(\frac{u_3 - u_3^*}{h^*} + \left(\frac{\partial v}{\partial x}\right)_3\right)\right.$$
$$\left.\frac{t^* G^*}{tG} - \left(\frac{v_3 - v_2}{h} + \frac{w_3 - w_3^{**}}{l^{**}}\right)\frac{t^{**} G^{**}}{tG}\right), \quad (23)$$

$$\left(\frac{\partial u}{\partial z}\right)_4 = \left(\frac{\delta_4 G_0}{tG} - \left(\frac{\partial w}{\partial x}\right)_4 - \left(\frac{u_4 - u_4^*}{h^*} + \left(\frac{\partial v}{\partial x}\right)_4\right)\right.$$
$$\left.\frac{t^* G^*}{tG} - \left(\frac{v_4 - v_1}{h} + \frac{w_4^{**} - w_4}{l^{**}}\right)\frac{t^{**} G^{**}}{tG}\right). \quad (24)$$

Shape functions used in the displacement field definitions in Eq. (19) and (20) have been introduced in Imala et al. (2025).

2.3 *Finite element equations*

An orthotropic approach to describing material properties is used in the cruise ship concept design phase, where plate elements represent structures that span over multiple plate stiffening structures. Finite element formulations incorporate material properties in the form of [C]-matrix:

$$C_{11} = \frac{E_1}{(1 - \nu_{12}\nu_{21})}, \quad (25)$$

$$C_{22} = \frac{E_2}{(1 - \nu_{12}\nu_{21})}, \quad (26)$$

$$C_{12} = \nu_{12} C_{22}, \quad (27)$$

$$C_{66} = G_{12}, \quad (28)$$

where E_1 and E_2 represent the orthogonal Young's moduli, G_{12} is the in-plane shear modulus, and v_{21} and v_{12} are the orthogonal Poisson ratios.

Finite element equations are described for vertical longitudinal elements in Equations (29) to (31) and horizontal elements in Equations (32) to (34) and for vertical transversal elements in Equations (35) to (37).

$$\int_\Omega t[\mathrm{B}_1]^T [C][\mathrm{B}_1] dxdz \{\Delta_1\} - \int_\Omega t[\psi_1]^T \begin{Bmatrix} f_x \\ f_z \end{Bmatrix} dxdz = 0$$
$$(29)$$

$$\int_\Omega t[\mathrm{B}_1]^T [C][\mathrm{B}_1] dxdz \{\Delta_1\} = [K_1] \quad (30)$$

$$\int_\Omega t[\psi_1]^T \begin{Bmatrix} f_x \\ f_z \end{Bmatrix} dxdz = \{F_1\} \quad (31)$$

$$\int_\Omega t[\mathrm{B}_2]^T [C][\mathrm{B}_2] dxdy \{\Delta_2\} - \int_\Omega t[\psi_2]^T \begin{Bmatrix} f_x \\ f_y \end{Bmatrix} dxdy = 0 \quad (32)$$

$$\int_\Omega t[\mathrm{B}_2]^T [C][\mathrm{B}_2] dxdy \{\Delta_2\} = [K_2] \quad (33)$$

$$\int_\Omega t[\psi_2]^T \begin{Bmatrix} f_x \\ f_y \end{Bmatrix} dxdy = \{F_2\} \quad (34)$$

$$\int_\Omega t[\mathrm{B}_3]^T [C][\mathrm{B}_3] dydz \{\Delta_3\} - \int_\Omega t[\psi_3]^T \begin{Bmatrix} f_y \\ f_z \end{Bmatrix} dydz = 0 \quad (35)$$

$$\int_\Omega t[\mathrm{B}_3]^T [C][\mathrm{B}_3] dydz \{\Delta_3\} = [K_3] \quad (36)$$

$$\int_\Omega t[\psi_3]^T \begin{Bmatrix} f_y \\ f_z \end{Bmatrix} dydz = \{F_3\} \quad (37)$$

Shape function linear combinations in matrix form for in-plane displacements are described in matrixes $[Y_1]$, $[Y_2]$ and $[Y_3]$. In-plane derivations are included in matrices $[B_1]$, $[B_2]$ and $[B_3]$ where:

$$[C] = \begin{bmatrix} C_{11} & C_{12} & 0 \\ C_{12} & C_{22} & 0 \\ 0 & 0 & C_{66} \end{bmatrix}, \quad (38)$$

$$[B_1] = [D_1][\psi_1] = \begin{bmatrix} \frac{\partial}{\partial x} & 0 \\ 0 & \frac{\partial}{\partial z} \\ \frac{\partial}{\partial z} & \frac{\partial}{\partial x} \end{bmatrix} [\psi_1], \quad (39)$$

$$[B_2] = [D_2][\psi_2] = \begin{bmatrix} \frac{\partial}{\partial x} & 0 \\ 0 & \frac{\partial}{\partial y} \\ \frac{\partial}{\partial y} & \frac{\partial}{\partial x} \end{bmatrix} [\psi_2], \quad (40)$$

$$[B_3] = [D_3][\psi_3] = \begin{bmatrix} \frac{\partial}{\partial y} & 0 \\ 0 & \frac{\partial}{\partial z} \\ \frac{\partial}{\partial z} & \frac{\partial}{\partial y} \end{bmatrix} [\psi_3]. \quad (41)$$

3 CRUISE SHIP GEOMETRY AND FINITE ELEMENT MODEL

The analysis presented in this article has been conducted on a conceptual cruise ship model with global dimensions length $L_{tot} = 300$m, breadth $B_{tot} = 42$m, height $H_{tot} = 51$m, see Figure 4. The

model consists of 16 decks, including double bottom and cofferdam; deck spacing is uniformly defined as 3.4 m. Longitudinally, the cross-section has been divided with longitudinal bulkheads and pillars. Weakened structures such as the superstructure deck and pillars have been modelled with plate elements using lowered material stiffness properties for realistic global structural behaviour to simplify the modelling process in the conceptual design phase.
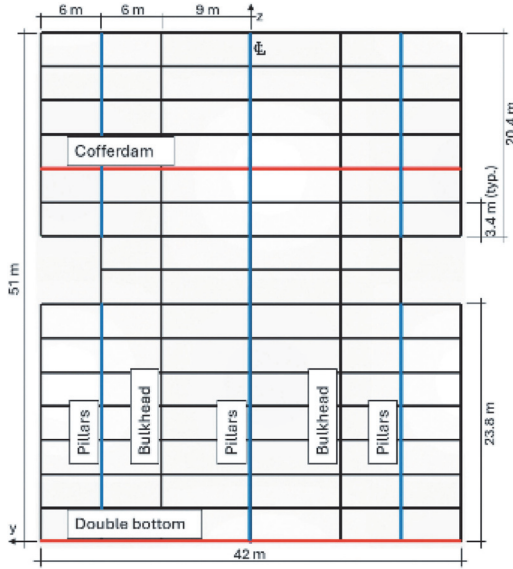

Figure 4. Conceptual cruise ship cross-section dimensions.

Transversal bulkheads have been placed with 40 m step in the aft and foreship. Two midship watertight section lengths have been set to 30 m, see Figure 5.
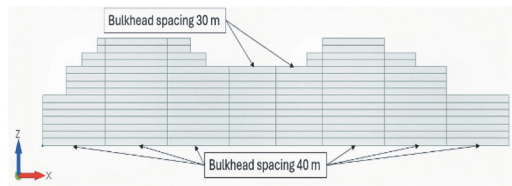

Figure 5. Transversal bulkhead spacing.

In concept design phase, stiffened panel sections that include plating stiffening elements have been represented as equivalent simple plate segments, where orthogonal material properties have been adjusted. Similar approach can be applied in areas with significant openings, such as deck and bulkhead openings as well as areas between pillars and superstructure outside shells, where most of the stiffness is provided by beam structures. This equivalent plating application for beam structures is suitable for global response contribution but is not capable of inter-elemental response analysis. Figure 6 shows example structures for deck, deck openings,

bulkheads and pillars that have been converted into equivalent plate regions.

Weakened material properties have been used in significant horizontal and vertical openings to represent stair openings and main corridor openings in longitudinal and horizontal bulkheads. Material properties and application cases are consolidated in Table 1. Structural breakdown with structure thicknesses and colour-separated material designations are shown in Figure 7.
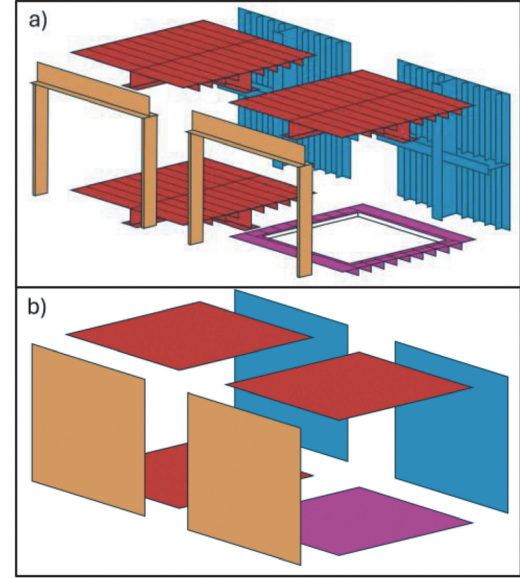

Figure 6. Structural segments for a) plating with stiffening structures, b) equivalent plating structures.

Table 1. Material property definitions and applications.

Name	Young's modulus, $E_1; E_2$ [GPa]	Poisson ratio, ν	Application
M1	210	0.3	Hull, bulkheads, decks,
M2	50	0.3	Superstructure shell, pillars, superstructure bulkhead openings
M3	100	0.3	Hull bulkhead openings
M4	10	0.3	Deck openings

Longitudinal vertical elements have been uniformly dimensioned as 3.4x5 m, where 3.4 m is the uniform vertical deck spacing. A uniform length of 5 m is defined for vertical and horizontal elements along the x-axis. Element dimensions in the transversal direction depend on the distance between adjacent longitudinal pillars and bulkhead structures. 5x9 m elements are used between the central pillar line and longitudinal bulkheads, while 5x6 m elements are used between the outer shell and the longitudinal bulkheads. Transversal bulkheads use, respectively, 3.4x9 m and 3.4x6 m elements. The coarse mesh model in total has 5716 nodes and 10228 elements; see Figure 8.
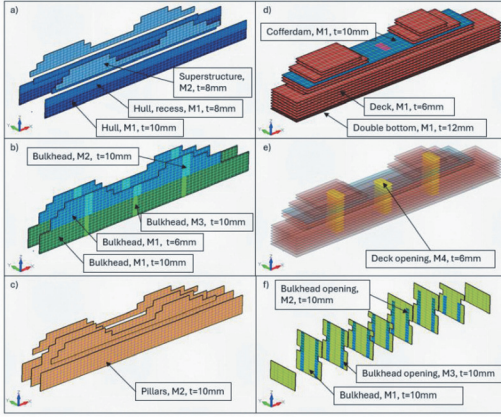
53

Figure 7. Structural breakdown of cruise ship conceptual model: a) outer shell, b) longitudinal bulkhead, c) pillars, d) deck plating, e) deck openings, f) transversal bulkheads.

In the finer mesh model, the element dimensions have been decreased to offer more data points for the analysis. Vertically, the deck spacing has been divided between 3 elements, longitudinally and transversally; the element dimensions have been divided such that the length along the x-axis and y-axis for all elements is 1 m. Thus, vertical longitudinal and transversal elements are dimensioned as 1x1.13 m, and horizontal elements are dimensioned as 1x1 m, see Figure 8.

Loading has been applied to outer shell structures, longitudinal bulkheads and pillars along the highlighted curves on the double bottom in Figure 9.
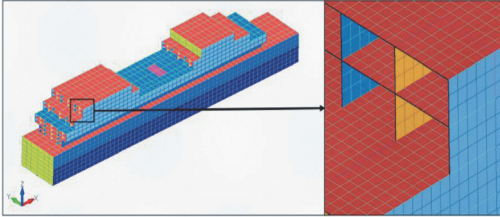

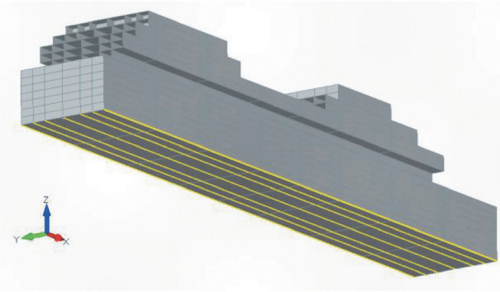Figure 8. Finite element 3D models for conceptual cruise ship.

Figure 9. Load carrying edges for vertical longitudinal structures.

Load per length unit has been defines as:

$$(x) = p_0 * \cos\left(\frac{2\pi x}{L}\right), \qquad (42)$$

where load amplitude p_0=200 N/mm and total length of L_{tot}=300 m.

Boundary conditions are applied on the model in the form of an elastic foundation, where a single row of elements is added to the outer shell and bulkhead bottom edges, see Figure 10. Free nodes for elastic foundation elements are fixed to the ground, and stiffness properties E_{el}=1 GPa and v_{el}=0.3 are used.

The HSD formulation has been implemented using Matlab 2023 software to create a global stiffness matrix utilising nodal point cloud and mesh properties data as input parameters. FEMAP 2021.2 software Direct Matrix Input G-set (DMIG) procedure has been used to import the generated global stiffness matrix. FEMAP 2021.2 software with Simcenter Nastran solver has been used to collect static response data for all finite element models.
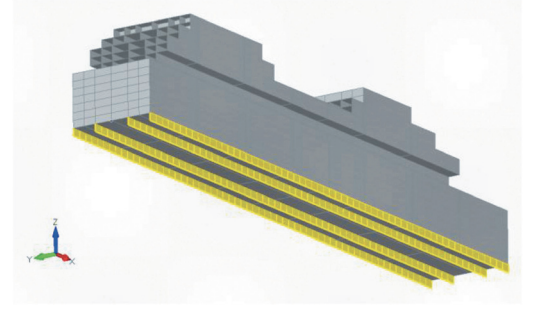

Figure 10. Elastic foundation elements.

4 RESULTS

The analysis presented in this article focuses on comparing shear stress distributions in various planes and cross-sections between the coarse, linear mesh model, fine linear mesh model and coarse HSD mesh model. Longitudinal distributions of stresses are presented in transitionary layers at the main deck at z=23.8 m, see Figure 11, Figure 12, in the transition between recess and first cabin deck at z=30.6 m, see Figure 13, and at the cofferdam transition at z=37.4 m, see Figure 14. Longitudinal stress distribution graphs include a low and a high approach to the transition layer, representing the direction of movement. This is achieved in fine mesh models due to the smaller distance to the layer from which the results are averaged to describe nodal values at the exact layer. For the HSD element mesh, this is achieved with the parametric description of the shear deformation variable, which allows a discontinuous expression of stresses at the transition. For coarse mesh models, this is not achieved as coarse, linear elements average nodal values over a large area, and thus, accuracy closer to the transition is lost.

Cross-sections for shear stress vertical distribution analysis are chosen at coordinate x=52.5 m to analyse stress response in an area where structural discontinuities are not prominent; see Figure 15. Cross-sections at x=172.5 m, see Figure 16, at x=182.5 m, see Figure 17, give an overview of the stress distributions in nearby cross-sections to structural discontinuities.

The longitudinal distributions of shear stresses demonstrate the necessity for a direction-specific parametric approach in describing shear stress values at topological transition layers. Figure 11 illustrates that the coarse mesh produces identical values for both approaches due to nodal stress averaging in the main deck and longitudinal bulkhead cross-section. These averaged values deviate from the fine mesh results by up to 40%, while the HSD mesh demonstrates a significantly higher correlation with the fine mesh results. Local stress fluctuations induced by topological variations in the bulkhead and deck openings are accurately captured by the HSD and fine linear mesh with comparable precision. In contrast, the coarse, linear mesh fails to resolve these subtle variations due to an insufficient degree of freedom coupling conditions, highlighting its limitations in capturing approach-specific stress phenomena.
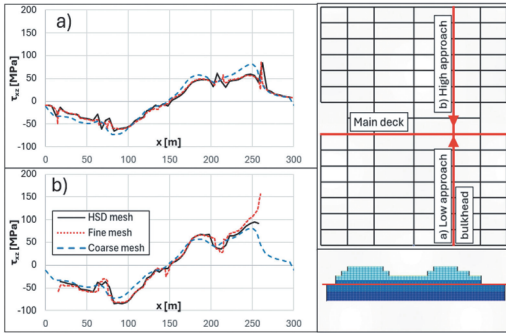

Figure 11. Longitudinal shear stress distribution in the bulkhead at main deck level.

Figure 12 illustrates the shear stress distributions in the outer shell at the main deck interface. All meshing variations exhibit highly consistent results at the low approach of the main deck intersection. This accuracy is attributed to the stress values evaluated in the topmost layer of the hull's outer shell, where nodal stress averaging is not required. In areas experiencing more intense stress fluctuations, the coarse mesh model demonstrates reduced accuracy in capturing peak stress values. In contrast, the HSD mesh maintains precision comparable to the fine mesh results. For the high approach, the coarse mesh shows significant limitations as stress values are averaged between the recess shell elements and adjacent pillar elements, resulting in deviations of approximately 40% from the fine mesh baseline.
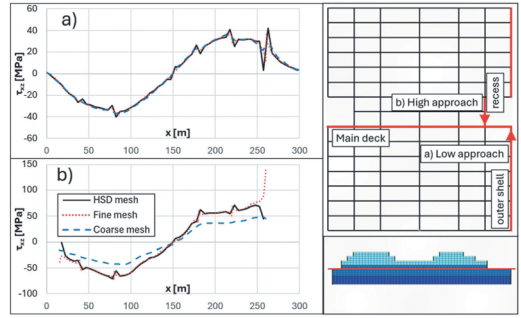

Figure 12. Longitudinal shear stress distribution in the hull outer shell and recess shell at main deck level.

Figure 13 presents stress distributions at the cabin deck and outer shell transitions. The phenomena observed parallel those at the main deck transitions. Here, the high approach, unaffected by nodal stress averaging, demonstrates excellent correlation across all mesh types, with minor discrepancies in local peak stress values for the coarse linear mesh. The HSD mesh captures local stress peaks with high accuracy. In contrast, the coarse, linear mesh fails to capture these peak values due to its inherent limitations in element size and lower-order interpolation methodology. The low approach shows up to 30% deviation in expressed stress values from the fine mesh results, while the HSD mesh maintains high precision.
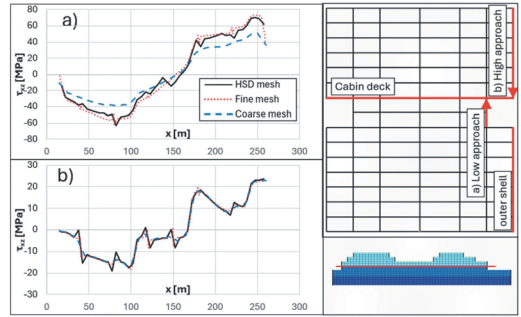

Figure 13. Longitudinal shear stress distribution in the superstructure outer shell and recess shell at cabin deck level.

Figure 14 illustrates the longitudinal shear stress distributions at the cofferdam and outer shell transitions. The coarse mesh model shows substantial inconsistencies in the low approach, particularly significant due to the high non-linearity of shear stresses in proximity to discontinuous structures. The HSD mesh model demonstrates a high capability of capturing these stress fluctuations with precision comparable to the fine linear mesh results. The high approach further fortifies the notion that the fine linear mesh and HSD mesh characterise discontinuous stress distributions with high correlation, while the coarse mesh underestimates peak stress values.
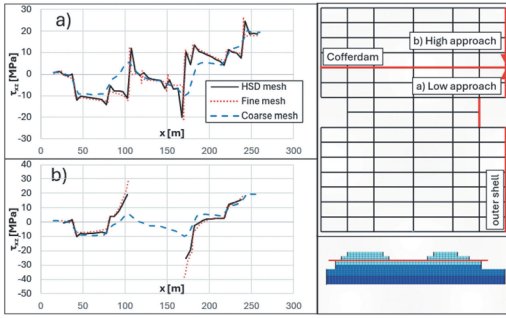
Figure 14. Longitudinal shear stress distribution in the outer shell and cofferdam level.

Analysis of the vertical shear stress distributions in critical cross-sections shows the necessity for inter-elemental stress characterisation. While nodal stress values from coarse mesh models may occasionally align with fine mesh distributions at nodal coordinates, peak stresses frequently occur within element boundaries. These internal stress concentrations require either higher-order approximation functions or mesh refinement for accurate description, highlighting the limitations of simple nodal interpolation methods.
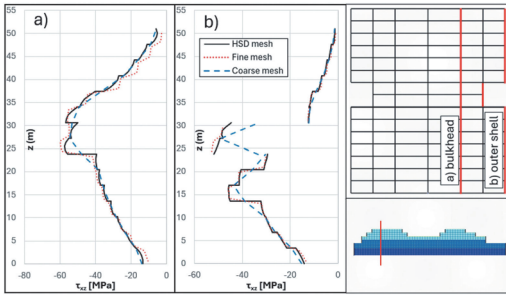

Figure 15. Vertical shear stress distribution at x=52.5 m.

Figure 15 illustrates a cross-section in a ship area, where structural discontinuities do not cause high shear stress fluctuations and thus serve as a baseline analysis. In topologically varying transitions, shear stress distributions go through a discontinuous description of shear stress. In Figure 15 a) this can be observed at z = 23.8 m, where longitudinal bulkhead thickness transitions from 10 mm to 6 mm. In surrounding elements, all meshing variations show good correlation; however, in the transition layer, coarse mesh analysis shows nodal averaging and thus, precision is lost. The HSD mesh and fine linear mesh maintain their correlation. Similar phenomena can be seen in Figure 15 b) where the outer shell thickness changes from 10 mm to 8 mm at z = 13.6 m. Coarse mesh values in the recess structures in Figure 15 b) show the effects of nodal averaging between recess outer shell elements and adjacent pillar elements, which result in significant deviations from the HSD mesh and acceptable linear mesh results.

Significant inter-elemental shear stress variation can be observed in Figure 16 and Figure 17. Proximity to structural discontinuity above the cofferdam deck at $z = 37.4$ m increases the stress variation to where coarse mesh produces results that severely underestimate the peak stress values above the cofferdam in Figure 16 a) and Figure 16 b). While other areas of the stress distribution graphs behave parallel to Figure 15, peak stress values for coarse mesh are underestimated in bulkhead structures by approximately 60%, while the overestimation of peak values by the HSD mesh stays between 6-13%.
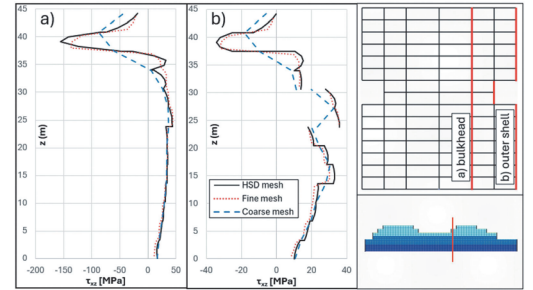

Figure 16. Vertical shear stress distribution at x=172.5 m.

In Figure 17 a) the residual effects of two discontinuous structure levels can be observed as the stress distribution shows double flat peaks above the cofferdam deck. The coarse mesh does not produce significant deviations from these peak values. However, an apparent lack of data density is experienced with coarse linear approximations, as the distribution does not capture local deviations.
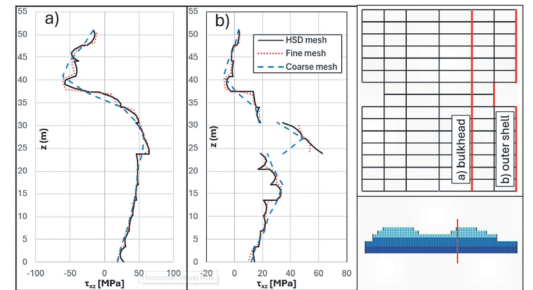
Figure 17. Vertical shear stress distribution at x=182.5 m.

5   CONCLUDING REMARKS

This article presents a modified higher-order shear deformation (HSD) method for global static response analysis of multideck hull girders. The analysis focuses on a marine industry case study using a conceptual cruise ship model, where plating and stiffening structures are simplified into equivalent plating structures with varying material and topological parameters. Complex structural discontinuities are incorporated as

56

partial-length superstructure, stepped cabin deck configuration and discontinuous top decks above the cofferdam, as these features significantly influence global stress distribution and overall design feasibility.

The modifications to the HSD method include transversal vertical elements, enhancing the shear deformation variable definition in longitudinal vertical elements. The updated displacement field definitions and the finite element formulation overview are presented. The method uses a formulation where the shear deformation variable is parametrically described to allow for direction-specific stress description in topological or geometrical transition layers, generating more realistic stress distributions than identically dimensioned coarse, linear mesh.

Analysis results show that the coarse HSD mesh consistently outperforms coarse, linear mesh, confirming the necessity of parametric formulation. Nodal stress averaging in linear mesh applications leads to significant stress distribution misrepresentation. The HSD mesh and fine linear mesh show a good correlation in all chosen planes. Cross-sectional shear stress distributions further confirm the limitations of nodal averaging in transition layers and emphasise the necessity of inter-elemental stress description. The HSD mesh successfully finds peak stress values within the element's boundaries, while fine linear mesh captures the peak stress values through increased nodal density. Although coarse linear mesh produces nodal stress results that often coincide with the finer linear mesh distributions, it does not detect critical peak stresses within element boundaries, particularly near structural discontinuities.

In practical applications, the HSD formulation accurately estimates the structural response of multi-deck ship structures in the conceptual design phase, outperforming commonly used and identically dimensioned linear mesh finite element models. The method presents a practical alternative to conventional 3D finite element methods in models where a complex stress behaviour is of interest in transitional structure layers, and accurate peak stress detection requires higher-order approximations. This method maintains computational efficiency comparable to traditional linear mesh while delivering superior accuracy in results.

REFERENCES

Avi E, Lillemäe I, Romanoff J, Niemelä A. 2015. Equivalent shell element for ship structural design. Ships Offshore Struct. 20(3):239–255.

Bleich, H.H. 1953. Nonlinear distribution of bending stresses due to distortion of the cross-section. J. Appl. Mech., 20(1): 95–104.

Crawford, L. 1950. Theory of long ships' superstructure. Trans SNAME, 58: 693–732.

Imala, M.M., Naar, H., Tabri, K., & Romanoff, J. 2022. Toward the application of the layer-wise displacement theory in passenger ships—a quasi-static response. Mechanics of Advanced Materials and Structures, 30 (22): 4698–4710.

Imala, M.M., Naar, H., Tabri, K. 2025. Higher-order shear deformation formulation for the structural response of a multideck ship. To be published in Ships Offshore Struct. Spring 2025.

Naar, H., Varsta, P., Kujala, P. 2004. A theory of coupled beams for strength assessment of passenger ships. Mar. Struct., 17: 590–611.

Naar, H. 2006. Ultimate strength of hull girder for passenger ships. Doctoral Dissertation, Helsinki University of Technology.

Reddy, J.N. 1984. A simple Higher-Order Theory for Laminated Composite Plates. J. Appl. Mech., 51(4): 745–752.

Reddy, J.N. 2004. Mechanics of laminated composite plates and shells – theory and analysis, 2nd ed. Boca Raton (FL): CRC Press.

Romanoff J., Varsta P. 2007. Bending response of web-core sandwich plates. Compos Struct. 81: 292–302.

Zanic V., Andric J., Prebeg P. 2013. Design synthesis of complex ship structures. Ships Offshore Struct. 8: 383–403.

Teguh, P., Kõrgesaar, M., Jelovica, J., Tabri, K., Naar, H. 2021. Ultimate strength assessment of stiffened panel under uni-axial compression with non-linear equivalent single layer approach. Mar. Struct., 78: 103004.

Curriculum vitae

Personal data

Name:	Mikk-Markus Imala
Date of birth:	22.04.1995
Place of birth:	Tallinn, Estonia
Citizenship:	Estonian

Contact data

E-mail:	mikk-markus.imala@taltech.ee

Education

2020–2025	Tallinn University of Technology, Engineering Sciences, PhD
2017–2020	Aalto University, Mechanical Engineering, MSC
2014–2017	Tallinn University of Technology, Mechanical Engineering, BSC

Language competence

Estonian	Native language
English	Fluent

Professional employment

2019–2020	Mechanical Engineer, MEC Insenerilahendused OÜ
2020–	Junior Researcher, Tallinn University of Technology
2022–2024	Mechanical Engineer, AuveTech OÜ
2024–2025	Mechanical Engineer, Alas-Kuul AS
2025–	Senior Multibody Dynamics Engineer, Milrem AS

Defended theses

- 2017, Double-hull breaching energy in oblique angle ship-tanker collisions, Mechanical Engineering BSc, supervisor Martin Heinvee, Department of Mechanical and Industrial Engineering, Tallinn University of Technology

- 2020, Higher-order coupled beam theory, Mechanical Engineering MSc, supervisor prof. Heikki, Remes, PhD Hendrik Naar, School of Engineering, Aalto University.

Field of research

- Finite element method
- Higher-order shear deformation theories
- Elastic response analysis
- Passenger ships structures

Scientific work

1. Imala, M. M., Naar, H., Tabri, K., & Romanoff, J. 2022. Toward the application of the layer-wise displacement theory in passenger ships—a quasi-static response. Mechanics of Advanced Materials and Structures, 30(22), 4698–4710. DOI: 10.1080/15376494.2022.2103859
2. Imala, M. M., Naar, H., & Tabri, K. 2025. Higher-order shear deformation formulation for the structural response of a multideck ship. Ships and Offshore Structures, 1–26. DOI: 10.1080/17445302.2025.2507714
3. Imala, M.M.; Naar, H.; Tabri, K. 2025. Passenger ship global static response analysis implementing a modified higher-order shear element description. Innovations in the Analysis and Design of Marine Structures. (49–57). CRC Press. DOI: 10.1201/9781003642411-6.

Elulookirjeldus

Isikuandmed

Nimi:	Mikk-Markus Imala
Sünniaeg:	22.04.1995
Sünnikoht:	Tallinn, Eesti
Kodakondsus:	Eesti

Kontaktandmed

E-post:	mikk-markus.imala@taltech.ee

Hariduskäik

2020–2025	Tallinna Tehnikaülikool, Tehnikateadused, PhD
2017–2020	Aalto Ülikool, Mehaanika Inseneeria, MSC
2014–2017	Tallinna Tehnikaülikool, Mehaanika Inseneeria, BSC

Keelteoskus

Eesti keel	Emakeel
Inglise keel	Kõrgtase

Teenistuskäik

2019–2020	Mehaanika insener, MEC Insenerilahendused OÜ
2020–	Nooremteadlane, Tallinna Tehnikaülikool
2022–2024	Mehaanika insener, AuveTech OÜ
2024–2025	Mehaanika insener, Alas-Kuul AS
2025–	Vanem mitme-keha dünaamika insener, Milrem AS

Kaitstud tööd

- 2017, Tankeri küljekonstruktsiooni purunemisenergia mittetäisnurksel kokkupõrkel laevaga, Mehaanika Inseneeria BSc, juhendaja Martin Heinvee, Mehaanika ja tööstustehnika instituut, Tallinna Tehnikaülikool

- 2020, Kõrgemat järku seotud talade meetod, Mehaanika Inseneeria MSc, juhendaja prof. Heikki, Remes, PhD Hendrik Naar, Inseneeria teaduskond, Aalto Ülikool.

Uurimisvaldkond

- Lõplike elementide meetod
- Kõrgeat järku nihke deformatsiooni teooriad
- Elastse vaste analüüs
- Reisilaevade konstruktsioonid

Teadustööd

1. Imala, M. M., Naar, H., Tabri, K., & Romanoff, J. 2022. Toward the application of the layer-wise displacement theory in passenger ships—a quasi-static response. Mechanics of Advanced Materials and Structures, 30(22), 4698–4710. DOI: 10.1080/15376494.2022.2103859
2. Imala, M. M., Naar, H., & Tabri, K. 2025. Higher-order shear deformation formulation for the structural response of a multideck ship. Ships and Offshore Structures, 1–26. DOI: 10.1080/17445302.2025.2507714
3. Imala, M.M.; Naar, H.; Tabri, K. 2025. Passenger ship global static response analysis implementing a modified higher-order shear element description. Innovations in the Analysis and Design of Marine Structures. (49–57). CRC Press. DOI: 10.1201/9781003642411-6.